Estimation of wind and solar resources in Mali

Badger, Jake; Kamissoko, Famakan; Olander Rasmussen, Mads; Larsen, Søren Ejling; Guidon, Nicolas; Hansen, Lars Boye; Dewilde, Luc; Nørgård, Per Bromand; Nygaard, Ivan

Publication date:
2012

Document Version
Publisher's PDF, also known as Version of record

Estimation of wind and solar resources in Mali

DANIDA contract 1711

Feasibility of renewable energy resources in Mali

December 2012

UNEP RISØ CENTRE
ENERGY, CLIMATE AND SUSTAINABLE DEVELOPMENT

Authors: Jake Badger, Famakan Kamissoko, Mads Olander Rasmussen, Søren Larsen, Nicolas Guidon, Lars Boye Hansen, Luc Dewilde, Maiga Issa Alhousseini, Per Nørgård, Ivan Nygaard

Title: Estimation of wind and solar resources in Mali

December 2012

ISBN 978-87-92706-55-3

Contract:

DANIDA contract 1711

Front Page:
Measurement mast

Photo: Famakan Kamissoko

UNEP Risø Centre
Department of Management Engineering
Technical University of Denmark
Risø Campus
Frederiksborgvej 399, P.O. Box 49
Building 142
4000 Roskilde,
Denmark
Direct + 45 46775115
Fax + 45 46321999
Skype: ivan.nygaard3

Contents

List of abbreviations

CNESOLER	Centre National de l'Energie Solaire et des Energies Renouvelables
DANIDA	Danish International Development Agency
DGG	Department of Geography and Geology
DNE	Direction Nationale de l'Energie
DSSF	Down-welling Surface Short-wave Radiation Flux
EDM	Electricité de Mali
ENI-ABT	Ècole Nationale d'Ingenieurs - Abderhamabe Baba Touré
GLCC	Global Land Cover Classification
GMT	Greenwich Mean Time
GRAS	Geographic Resource Analysis & Science A/
IFNS	Inverse Froude Number Squared
KAMM	Karlsruhe Atmospheric Mesoscale Model
LSA-SA	Land Surface Analysis – Satellite Applications Facility
MBC	Central Domain
MBN	Northern Domain
MBS	Southern Domain
MCP	Measure-Correlate-Predict method
MFC	Mali Folkecenter Nyetaa
MMEE	Ministère des Mines, de l'Energie et de l'Eau
MSG	Meterosat Second Generation
NASA	National (USA) Aeronautics and Space Administration
NCAR	National (USA) Center for Atmospheric Research
NCEP	National (USA) Center for Environmental Prediction
NGA	National (USA) Geospatial-Intelligence Agency
NRG systems	Sensor Brand
NWA	Numerical Wind Atlas
OWA	Observational Wind Atlas
SEVIRI	Spinning Enhanced Visible and Infrared Imager
SRTM	Shuttle Radar Topography Mission
SSE	Surface meteorology and Solar Energy
STRM	Shuttle Radar Topography Mission
URC	UNEP Risoe Centre
USGS	United States Geological Survey
UTM	Universal Transverse Mercator coordinate system
WAsP	Wind Atlas Analysis and Application Program

1 Preface

The supply of affordable, reliable and environmentally friendly energy services is an important precondition for the economic development of Malian society. Currently demand for electricity is increasing by about 10% per annum, and demand for fuel for transport is increasing at an even higher level (BAD 2010). This presents enormous challenges to the Malian government and to national operators in reducing imports of fossil fuels, as well as to the national electricity utility, EDM (Energie du Mali), and to private investors in providing sufficient electricity at reasonable prices.

A large part of electricity production comes from large-scale hydropower produced on the Senegal and Niger rivers, but small- and large-scale diesel generators are still providing about 20% of total production. While interconnectors are being planned and built to meet some of the demand with electricity produced from natural gas in Ghana and Ivory Coast, there are still good political and economic reasons to tap into abundant national renewable energy resources, such as hydro-energy, solar energy, wind energy, biomass residues from agriculture, and energy crops producing liquid biofuel.

Since the 1980s, in cooperation with various development partners, Mali has conducted a number of development projects and programmes focusing on the increased use of renewable energy sources, while the Ministry for Mines, Energy and Water has developed a strategy for the development of renewable energy in Mali, which was adopted by the Ministerial Council (Conseil des Ministres) on 26 December 2006 (MMEE 2007). This strategy combines the aims of reducing poverty, validating national energy resources and ensuring the long-term security and environmental sustainability of the energy supply. Given the rapid increase in prices for imported fuels such as diesel and gasoline, it is increasingly worthwhile to assess the potential for giving renewable energy resources a central role in the future energy system: environmentally friendly renewable energy resources are abundant in Mali and are becoming increasingly competitive.

For the purpose of planning future investment in the renewable energy sector, the Malian energy authorities, Energie du Mali, private operators and international cooperation partners have expressed their needs for a more precise assessment of the size and variety of renewable energy resources in Mali. The Danish International Development Agency (DANIDA) has therefore provided the finance to map renewable energy resources under the heading of the 'Feasibility of Renewable Energy Resources in Mali', or 'Faisabilité de Resources d'Energies Renouvelables au Mali'.

A first scoping phase of the project was conducted in 2007-2008. The project report, submitted in 2008 and entitled 'Provisional mapping of Renewable Energy Resources in Mali, or 'Carte provisoire de ressources renouvelables du Mali', was based entirely on satellite data and meteorological models.

The present project has taken the first study further by including ground measurements of wind and solar resources, and by including extensive field studies to assess the potential for using biomass waste for energy and to assess the socio-economic impacts of growing cassava for biofuel production. Not all renewable energy resources have been mapped, however. The most important exception is the stock of energy resources contained in Mali's woody vegetation, which is not easily assessed from satellite data but is being assessed by other on-going projects.

The present project is covered in five main reports:

1) Analyses of the potential for sustainable, cassava-based bio-ethanol production in Mali
2) Agricultural residues for energy production in Mali
3) Pre-feasibility study for an electric power plant based on rice straw

4) Estimates of wind and solar resources in Mali
5) Screening of feasible applications of wind and solar energy in Mali, using the wind and solar maps for Mali

The project is being carried out by a group of university departments, research institutions and consultants led by the UNEP Risø Centre (URC) at the Technical University of Denmark (DTU) and conducted in cooperation with Direction Nationale de l'Energie (DNE) and Centre National de l'Energie Solaire et des Energies Renouvelables (CNESOLER) in Mali. The subcontracted institutions comprise Geographic Resource Analysis & Science A/S (GRAS), Department of Geography and Geology (DGG), University of Copenhagen, Ea Energy Analyses, 3E, Ecole Nationale d'Ingénieurs Abderhamabe Baba Touré (ENI-ABT) and Mali Folkecenter Nyetaa.

2 Wind resources – Observational wind atlas

2.1 Introduction

As part of the project 10 NRG Systems ® masts have been positioned at 14 sites in Mali to carry out high quality measurements. In this section an analysis of the measured wind data will be described. The analysis is performed in order to calculate generalized wind climate statistics for from the observed winds. This analysis is of value for assessment of wind resource in the vicinity of the measurement site, and is of value of the validation of the numerical wind atlas study, to be described in Section 3.

The measurement data was quality controlled and processed by the company 3E in Belgium. Then, to use the data for such an evaluation activity, it is necessary to evaluate local features, influencing especially the wind measurement, around the measurement stations, roughness, terrain, and obstacles, and to perform a local WAsP analysis (see section 2.4) to clean and homogenize the data for strictly local features.

The measurement masts were all placed and operated by CNESOLER. Ten sites were chosen by CNESOLER to provide windmeasurements for potential sites for windturbines, and the last four sites were chosen by the project in order to ensure a geographical spread for the calibration of the wind atlas. The sites have been reported in Kamissoko 2008, 2009a, 2009b, 2010.

Appendix B gives further details of the characteristics of the measured wind speed and direction distributions, and variations by month of year and variations by hour of day. In addition Appendix C gives information about the NRG Systems ® sensor serial numbers.

2.2 Summary of measurement sites

Table 2.1: Table giving the details about the sites' code and position.

Site name	Code	Longitude	Latitude	UTM zone	Easting	Northing
Bandiagara	BAN	-3.6026	14.3635	29	1082705	1594749
Gao	GAO	-0.0064	16.2524	30	820010	1799192
Gossi	GOS	-1.2836	15.8237	30	683820	1750185
Goundam	GOU	-3.6521	16.4040	30	430372	1813740
Hombori	HOM	-1.7113	15.2922	30	638368	1691052
Kadiolo	KAD	-5.7568	10.5660	29	854984	1169835
Kangaba	KAN	-8.4254	11.9457	29	562561	1320610
Kayes	KAY	-11.4084	14.4795	29	240394	1602123
Koro	KOR	-3.0939	14.0901	29	1138564	1565719
Mopti/Sévaré	MOP	-4.0843	14.5127	29	1030222	1610136
Niafunké	NIA	-3.9947	15.9350	30	393538	1761995
Nioro	NIO	-9.5774	15.2371	29	437993	1684633
San	SAN	-4.8932	13.2954	29	945155	1473479
Tombouctou	TOM	-2.9979	16.7300	30	500219	1849684

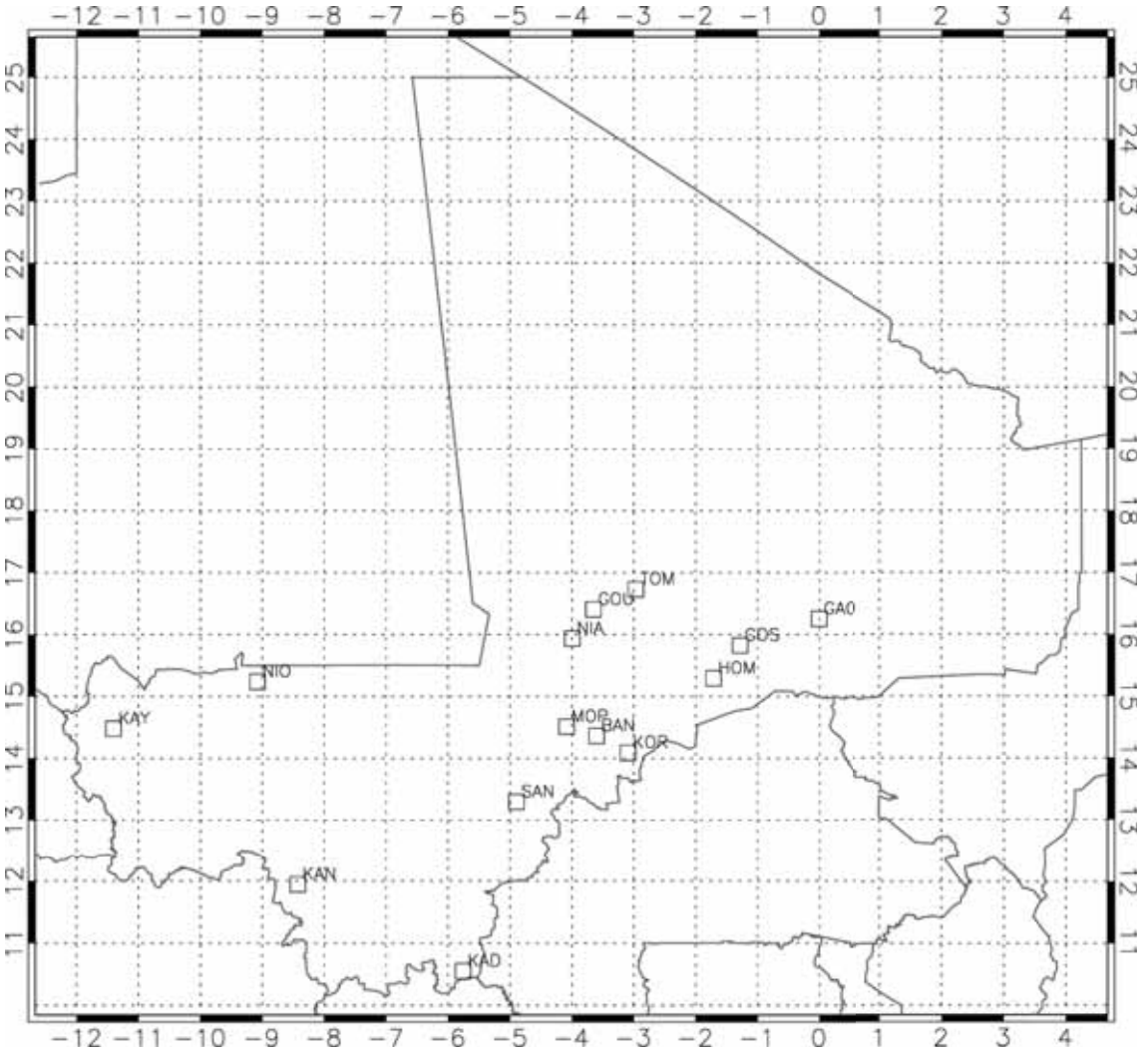

Figure 2.1: Map showing the location of the 14 wind and solar measurement sites. Axes are given in degrees longitude and latitude respectively. Lines indicated international borders around Mali.

Positional details of the measurement masts are given in Table 2.1: Table giving the details about the sites' code and position. A map of Mali and the location of the measurement mast is given in Figure 2.1 The masts are labelled using the 3 letter code given in Table 2.1.

2.3 Summary of data processing

The main concern for the type of anemometers installed (NRG #40) is the so-called "Dry Friction Whip phenomenon" (slowdown effect) that affected the NRG #40 due to problems in their manufacturing process. The slowdown effect affects serial numbers ranging from 26130 to 92049, thus the only measurements that are not affected are those from the 7 last sites (Bandiagara, San, Koro, Kadiolo, Kangaba, Kayes and Nioro). See Appendix C for information about the sensor serial numbers.

The slowdown effect occurs when an anemometer enters a vibratory mode, which occurs especially in the range 4-10 m/s when the wind speed is decreasing. The magnitude of the slowdown is therefore closely

related to the wind regime on a particular site. Also, it affects the top measurements more than the bottom measurements. However, there is no way to accurately assess when an anemometer enters or leaves the vibratory mode, unless a non-defect anemometer is installed at the same level. The magnitude of the slowdown is 0.3 to 0.6m/s, and increases with time.

NRG provided available papers by consultants who partnered with them to carry out comparisons of defect against non-defect sensors. First of all, according to one of these papers, 87 out of 99 anemometers with serial numbers ranging from 26130 to 92049 proved to be affected by the slowdown effect. So it is likely that almost all of the anemometers on 7 out of the 14 sites are affected. A method was provided to assess if measurements are affected or not, and which anemometer of a pair is the most affected. Using this method shows that all anemometers are more or less affected, but some probably not so much.

Although some authors have suggested corrections, here there is a reluctance to apply corrections, because first of all they were assessed based on a very limited number of measurements, and at locations that do not necessarily represent the wind conditions in Mali. In the end, it was decided that it was more appropriate to just dismiss the measurements that look the most affected by the slowdown.

The final recommendation was to exclude measurements from the top measurement level for the sites Gossi and Hombori, where only data at 22 m should be used. For the rest of the sites where anemometers were affected by slowdown, the measurements of the least affected anemometer of the pair were used.
For the last 7 sites were the anemometers were not affected by slowdown, the mast shading effect was cleaned from the measurements of the pair of anemometers at each height.

In addition the following observations are stated:

- One of the top anemometers at Gossi was damaged during a high wind event in August 2009, but this anemometer was not considered anyway, because it was the most affected by slowdown at the top level of this mast.
- A few periods should be removed from the measurements in Tombouctou in October 2009.
- A few periods were missing at Koro (1 incomplete day) and Sevare (4 incomplete or missing days).
- A few hours of data were missing from the measurements in Kadiolo, Kangaba, Kayes and Nioro around mid-May 2011.
- Vanes offset were negligible at all sites but Tombouctou, where an offset of 70° was applied.
- The datalogger in Tombouctou was configured in GMT-1 instead of GMT0.

Initially, the small periods of missing data were filled through a MCP method (measure-correlate-predicted) using data from the measurements giving the best agreement. However, for the WAsP analysis that follows the MCP values were rejected, as in any case the data recovery is very good; see Table 2.2 for a summary of data recovery for each site.

Table 2.2: Table summarizing the measurement masts data recovery and anemometer heights.

Site name	Mast code	Total data lines	Measured data lines	Fitted data lines	% measured	Anemometer heights [m]
Bandiagara	BAN	52560	52560	0	100.00	50, 30
Gao	GAO	52560	52560	0	100.00	40, 22
Gossi	GOS	52560	52560	0	100.00	22
Goundam	GOU	52560	52560	0	100.00	50, 30
Hombori	HOM	52560	52560	0	100.00	22
Kadiolo	KAD	52560	52488	72	99.86	40, 22
Kangaba	KAN	52560	52512	48	99.91	40, 22
Kayes	KAY	52560	52500	60	99.89	40, 22
Koro	KOR	52560	52518	42	99.92	50, 30
Mopti/Sévaré	MOP	52560	52560	0	100.00	40, 22
Niafunké	NIA	52560	52560	0	100.00	50, 30
Nioro	NIO	52560	52500	60	99.89	40, 22
San	SAN	52560	52560	0	100.00	50, 30
Tombouctou	TOM	52560	52424	136	99.74	40, 22

Finally, the measurement periods for the data used in the analysis of the 14 mast sites, it should be noted, are not concurrent. The measurement periods of the mast sites are given in Table 2.3.

Table 2.3: Table giving the 1-year period start and end dates used for the measurement sites.

Site name	Mast code	Measurement period	Start (incl)	End (incl)	Length
Gao	GAO	p1	Nov-08	Oct-09	1-year
Gossi	GOS	p1	Nov-08	Oct-09	1-year
Hombori	HAM	p1	Nov-08	Oct-09	1-year
Mopti/Sévaré	MOP	p1	Nov-08	Oct-09	1-year
Goundam	GOU	p2	Mar-09	Feb-10	1-year
Niafunké	NIA	p2	Mar-09	Feb-10	1-year
Tombouctou	TOM	p2	Mar-09	Feb-10	1-year
Bandiagara	BAN	p3	Jun-09	May-10	1-year
Koro	KOR	p3	Jun-09	May-10	1-year
San	SAN	p3	Jun-09	May-10	1-year
Kadiolo	KAD	p4	Sep-10	Aug-11	1-year
Kangaba	KAN	p4	Sep-10	Aug-11	1-year
Kayes	KAY	p4	Sep-10	Aug-11	1-year
Nioro	NIO	p4	Sep-10	Aug-11	1-year

2.4 Analysis using WAsP

WAsP is the industry standard tool for wind resource assessment and it contains a suite of microscale models for prediction of wind resources over the area surrounding a meteorological station, taking effects of local roughness changes and elevation changes into account. The WAsP flow model is a linear model with a polar grid. It is based on analysis of flow over hills described in Jackson and Hunt (1976). The roughness change model within WAsP accounts for inhomogeneity of surface roughness length surrounding an observation site, out to around 10 km. Inhomogeneous roughness leads to development of internal boundary layers and the effect of these on the wind profile is modeled in a sectorwise manner according to relationships found in Sempreviva et al (1989) and Rao et al (1974). An obstacle model is also contained in WAsP but this is not used as there are no obstacles impacting the sites. The local effects at the measurement site are removed and a generalized wind climate is calculated.

The generalized wind climate can then be used to calculate the wind climate at a nearby site through consideration of the new site's specific local elevation changes and roughness changes, through the models contained in WAsP. WAsP can also be used to predict the wind resource at different heights at the measurement site itself, by accounting for the effects of internal boundary layers due to nearby roughness changes, such that the profile departs from a logarithmic profile, and orographic speed-up effects, which are a function of height above ground. Site specific corrections for boundary layer stability are not performed as the default WAsP settings are used. A detailed description of the models within WAsP is given in Chapter 8 of Troen and Petersen (1989).

WAsP requires a description of the surface topograph (orography – changes in surface elevation – and surface roughness length). Evaluation of local roughness length conditions around each measurement station have been performed partly from aloft, using Google Earth, and partly from site visits. All of the sites have been visited on several occasions by the CNSOLER staff. Selected sites have been visited by staff from DTU Wind Energy, Denmark, in cooperation with CNSOLER. The selected sites and the dates visited are indicated below:

Tombouctou: 2008.05.02.
Nioro: 2011.05.15
Kayes: 2011.05.20
Kangaba: 2011.05.18.
Kadiolo: 2011.05.19.

The first of the stations is placed in the Northern Sahel region, the next two in the Western part, and the two last in the South of Mali. The first three stations all reflected fairly smooth Sahel terrain, and was placed in connection with local airports, while the two last stations were situated at "climate station" compounds, and were placed in more complex terrain, surrounded with more habitation and denser vegetated areas.

The orography was determined using the SRTM dataset, which is a near global dataset at approximately 90 m resolution. For each measurement site a 50 x 50 km orography map was created using the 10 m contour interval. Roughness change lines were inserted into the map by digitizing dominant feature using satellite imagery, i.e. boundaries between rivers, lakes, towns, and forested areas. The roughness length was determined from photographs around the sites and from satellite imagery. Roughness length values were refined by seeking best agreement for generalized wind climates derived from anemometers mounted at different heights on the same mast, where possible.

For WAsP analysis for verification was performed for all sites except Hombori and Bandiagara where only the lower anemometer data was available. The analysis of data from the upper anemometers was

prioritized, but subsequent of analysis of Hombori and Bandiagara is certainly considered worthwhile. In Figure 2.2 one can see the WAsP software being used to analysis measurement data for Nioro.

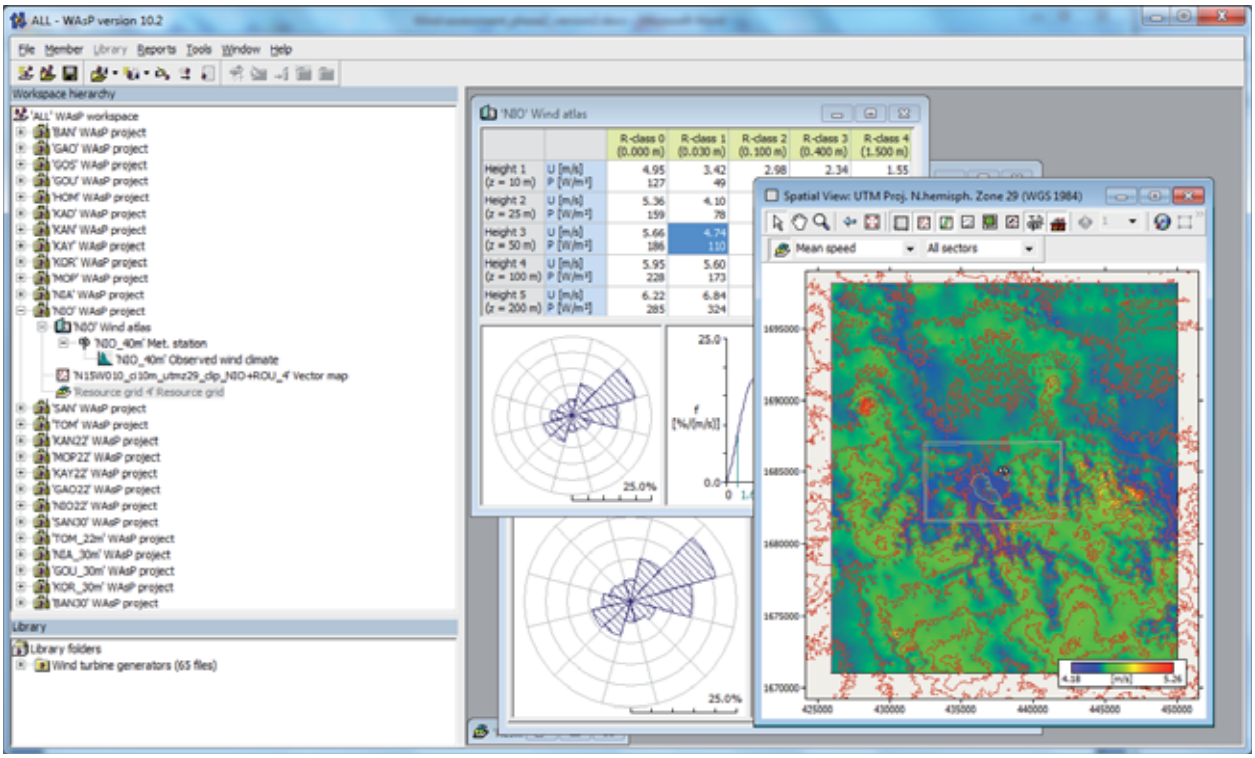

Figure 2.2: Screen shot of WAsP software during the analysis of measurement data, in this case from Nioro.The map window indicates the modelled variation of the annual mean 40 m wind speed due to orography and roughness length change features in the landscape.

2.5 Generalized wind climates

In Figure 2.3 the graphical representation of the generalized wind climates for the analysed sites are shown. The generalized wind climates contain information about the sectorwise wind speed frequency distribution and the wind direction frequency distribution. The generalization pertains to wind conditions for flat terrain and homogeneous surface roughness. In the case of the plotted climates the winds are given for 50 m above 3 cm roughness.

(a) Bandiagara (BAN)

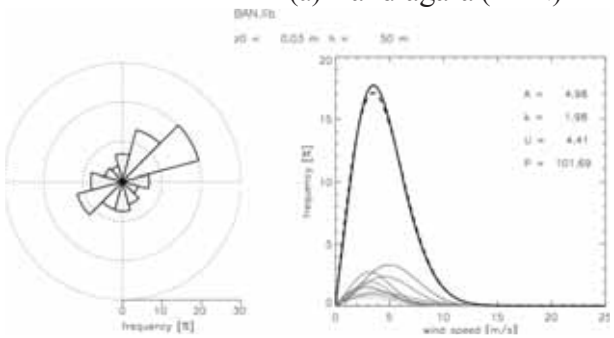

(b) Gao (GAO)

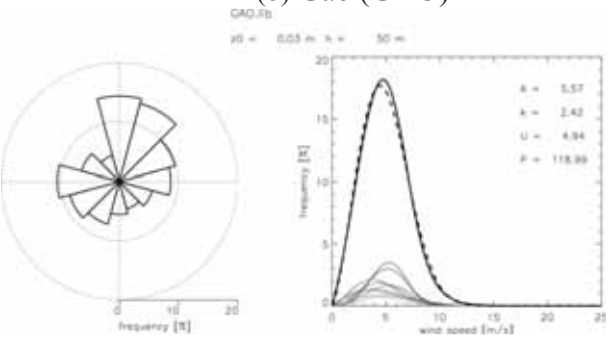

(c) Goundam (GOU)

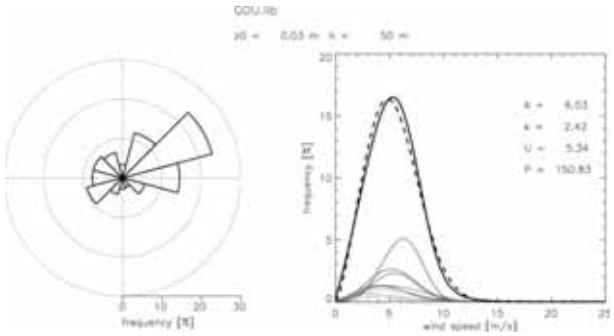

(d) Kadiolo (KAD)

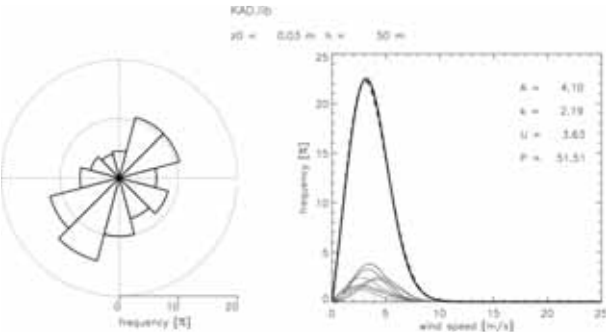

(e) Kangaba (KAN)

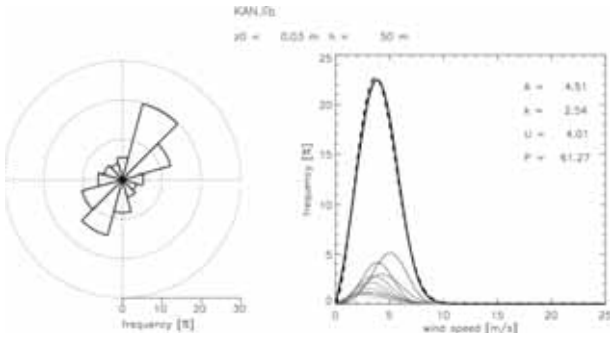

(f) Kayes (KAY)

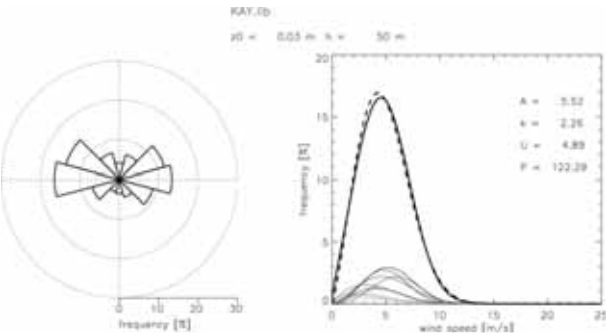

(g) Koro (KOR)

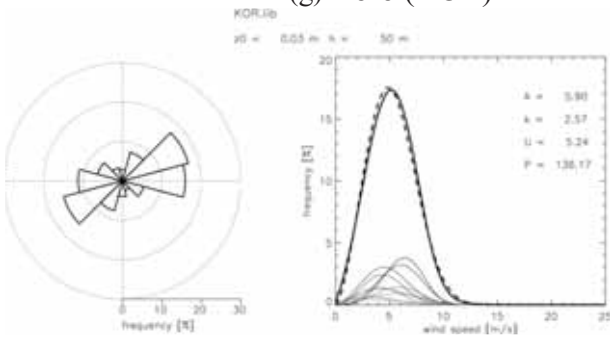

(h) Mopti/Sévaré (MOP)

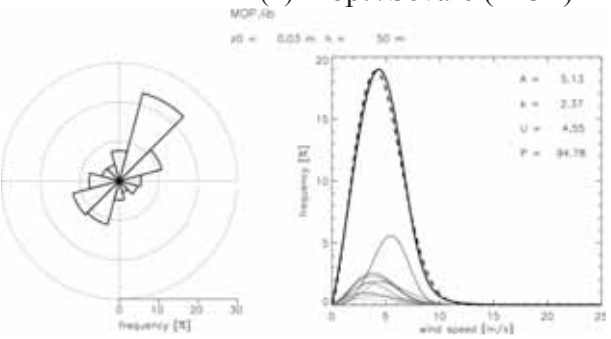

(i) Niafunké (NIA)

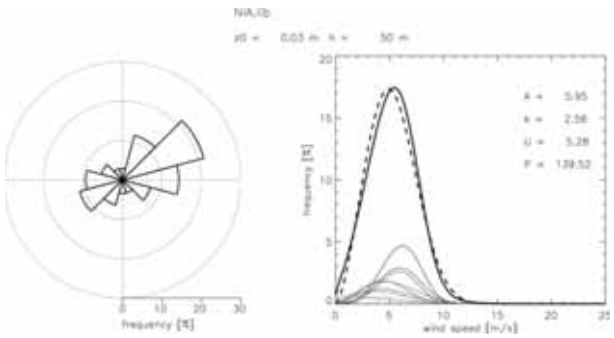

(j) Nioro (NIO)

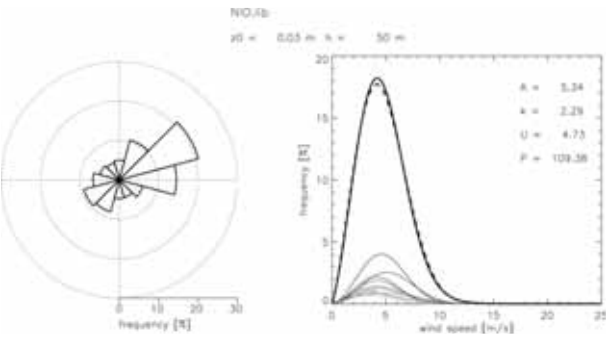

(k) San (SAN)

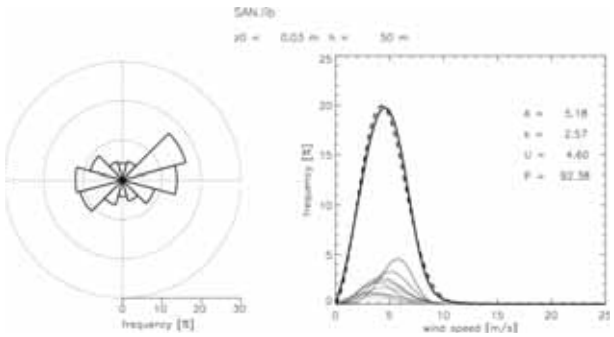

(l) Tombouctou (TOM)

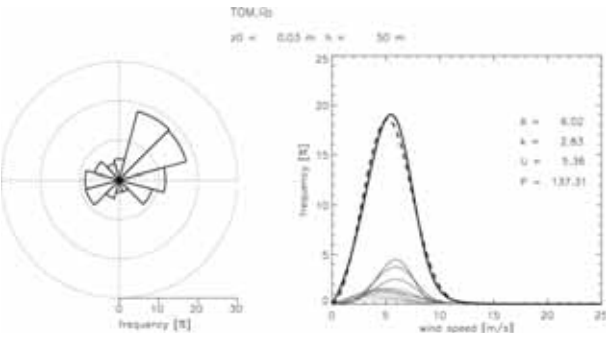

Figure 2.3: Graphs showing the generalized wind climate at the measurement sites at 50 m for standard conditions, flat terrain of homogeneous 3 cm roughness length. The wind rose plots give the direction frequency distribution and the line graphs indicate the wind speed distributions. The faint lines indicate the wind speed distributions for separate directions sectors. The bold solid line indicates the emergent wind speed distribution, i.e. sum of sectorwise distributions. The bold dashed line indicates the Weibull distributions of the total wind speed distributions. The printed values give the total wind speed distribution Weibull scale parameter (A), shape parameter (k), mean annual wind speed (u) in m/s and the power density (P) in W/m^2.

3 Wind resources – Numerical wind atlas

3.1 Introduction

The conventional method used to produce estimates of wind resource over large areas or regions, such as on a national scale, is to analyze wind measurements made at a number of sites around the region, as in for example the European Wind Atlas (Troen and Petersen, 1989). In order for this method to work well there needs to be a sufficient quantity of high quality data, covering the country. This criterion is sometimes difficult to satisfy and therefore other methods are required – methods that will not meet bankable accuracy in resource estimates, but on the other hand will typically give good indications of the geographical distribution of the wind resource, and as such will be very useful for decision making and planning of feasibility studies.

Numerical wind atlas methodologies have been devised to solve the issue of insufficient wind measurements. One such methodology is the KAMM/WAsP method developed at Risø National Laboratory (Frank and Landberg, 1997).

The real added value element of the KAMM/WAsP numerical wind atlas methodology is the ability to apply the derived generalized wind atlas data at the microscale using the WAsP software. This allows the WAsP user to make pre-feasibility calculations for any location covered by the numerical wind atlas, and to make estimates for annual energy production given specific turbine type and characteristics.

In the KAMM/WAsP methodology an approach called **statistical-dynamical downscaling** is used (Frey-Buness et al, 1995). The basis for the method is that there is a robust relationship between meteorological situations at the large-scale and meteorological situations at the small-scale.

Information about the large-scale meteorological situation is freely available from the NCEP/NCAR reanalysis data-set, (Kalnay et al, 1996). This data-set has been created by assimilating measurement data from around the globe in a consistent fashion from 1948 to the present day. The primary purpose for the generation of this data-set is to provide a reference for the state of the atmosphere and to identify any features of climate change. Another application of the data-set is as a long-term record of large-scale wind conditions. The NCEP/NCAR data is used to create around 100 different large-scale wind situations, called wind classes that represent the large-scale wind climate.

In order to make these wind classes meaningful at a smaller scale a mesoscale model is used to find out how the large-scale wind forcing is modified by regional scale topography. Therefore for each wind class a mesoscale model simulation is performed using the KAMM (Karlsruhe Atmospheric Mesoscale Model) (Adrian and Fiedler, 1991).

Post-processing of the results from all the simulations yields a wind resource map at the resolution of the model simulations. Further analysis of the results from the simulations with consideration to the topography as described in the mesoscale model, yields wind atlas maps for generalized surface conditions. Files containing detailed information about the wind speed and direction distributions that are directly compatible with the WAsP software (Mortensen et al, 2007), the wind industry standard for site resource assessment calculations, can also be generated.

There are two parts to a numerical wind atlas study: (i) The numerical modelling work itself and (ii) the verification study to determine the validity and likely uncertainty of the results reached by the numerical wind atlas.

This section starts by describing the numerical modelling and then draws on the results of the analysis of the recent wind measurements made during this project.

3.2 Model Description

The Karlsruhe Atmospheric Mesoscale Model (KAMM) is a 3D, non-hydrostatic, and incompressible mesoscale model. It is described in Adrian and Fiedler (1991), and Adrian (1994). Spatial derivatives are calculated in the model by central differences on a terrain following grid. The turbulent fluxes are modelled using a mixing-length model with stability dependent turbulent diffusion coefficients in stably stratified flow, and a non-local closure for the convective mixed layer. Lateral boundary conditions assume zero gradients normal to the inflow sides. On outflow boundaries, the horizontal equations of motion are replaced by a simple wave equation allowing signals to propagate out of the domain without reflection. Gravity waves can penetrate the upper boundary outward using the boundary condition of Klemp and Durran (1983).

KAMM is able to run as a "stand-alone" model, i.e. the model can be run by using only the large-scale forcing in the form of a single vertical profile of geostrophic wind and virtual potential temperature. Hence, it is not necessary to nest the mesoscale model within a larger model that must supply the boundary conditions. At regional scales the mesoscale model is used to model atmospheric flows in domains of 100-1000 km x 100-1000 km in size with a typical horizontal resolution of 2.5 to 10 km.

In the vertical the model extends from sea level to 5500 m above sea level, using 25 model levels employing a terrain following coordinate system. The interval between vertical levels is not uniform. This allows for more closely spaced vertical model levels near to terrain. The first 5 model levels are at 0 m, 20.3 m, 58.7 m, 115.3 m and 190.0 m above the surface. The separation between these levels is smaller in elevated terrain.

Figure 3.1 shows terrain elevation for the modelling domains used for this numerical wind atlas study. The surface elevation data is derived from NASA's Shuttle Radar Topography Mission (STRM30) dataset version 2. The dataset can be accessed via the USA's National Aeronautics and Space Administration (NASA) webpage (Internet Link [1]). This data uses a longitude-latitude projection at 30 arc second resolution. This elevation data is manipulated first to change it to a UTM coordinate system and then to change the coordinate system and resolution appropriately for the mesoscale simulations.

The aerodynamic surface roughness length data is derived from the United States Geological Survey (USGS) Global Land Cover Classification, also known as GLCC. The data can be accessed via a USGS webpage (Internet Link [2]). By means of a look-up table, the land-use types were converted to aerodynamic surface roughness lengths. This roughness data is manipulated first to change it to a UTM coordinate system and then to change the coordinate system and resolution appropriately for the mesoscale simulations. The map of the surface roughness for the mesoscale modelling domains is shown in Figure 3.2.

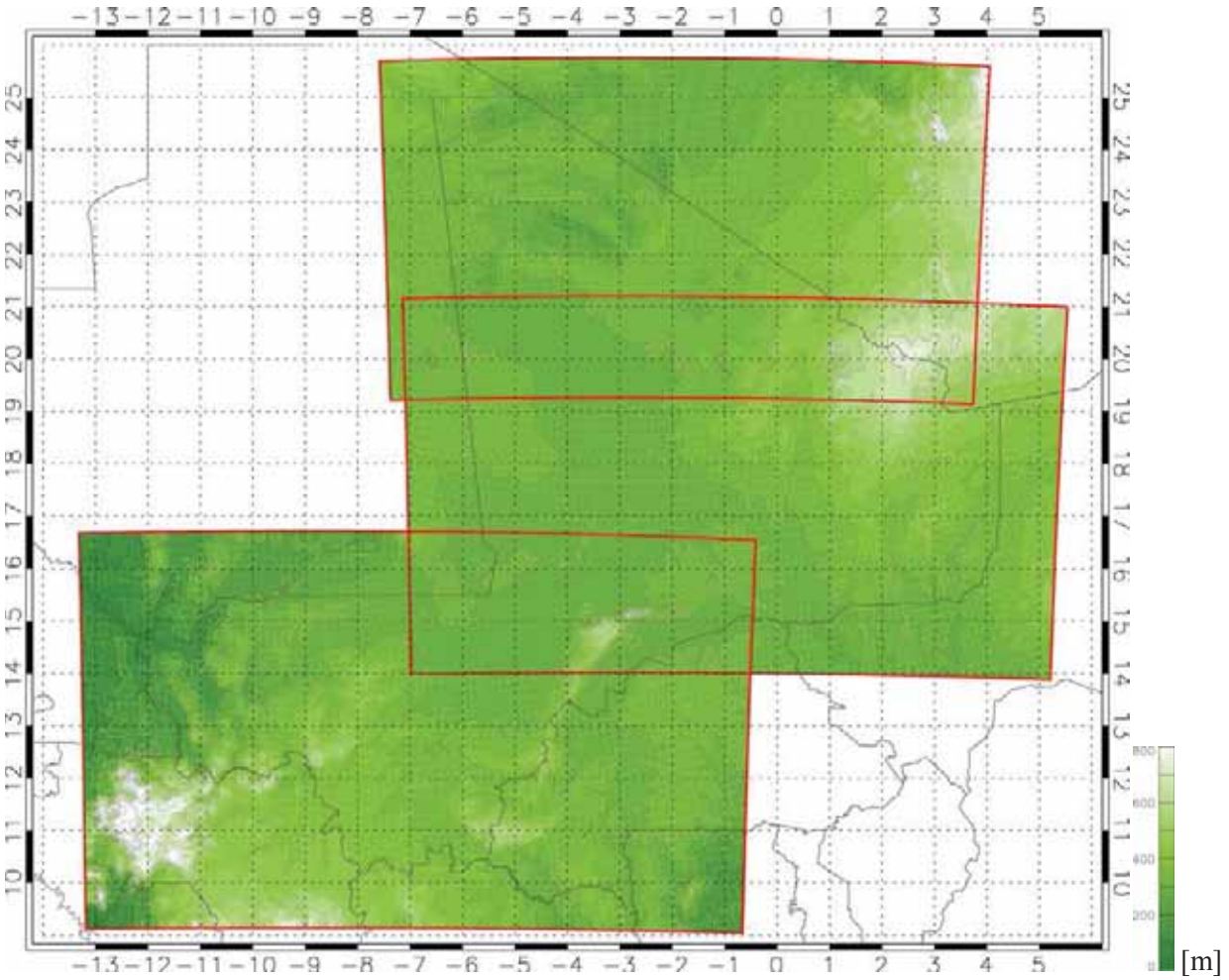

Figure 3.1: The surface elevation over the three computational domains used for the KAMM mesoscale modelling at 7.5 km resolution for Northern Mali, Central Mali, and Southern Mali domains, marked by the red domain boundary lines. The contour interval is 100 m. The x and y axis are in longitude and latitude. The data is derived from NASA's Shuttle Radar Topography Mission (STRM) dataset version 2.

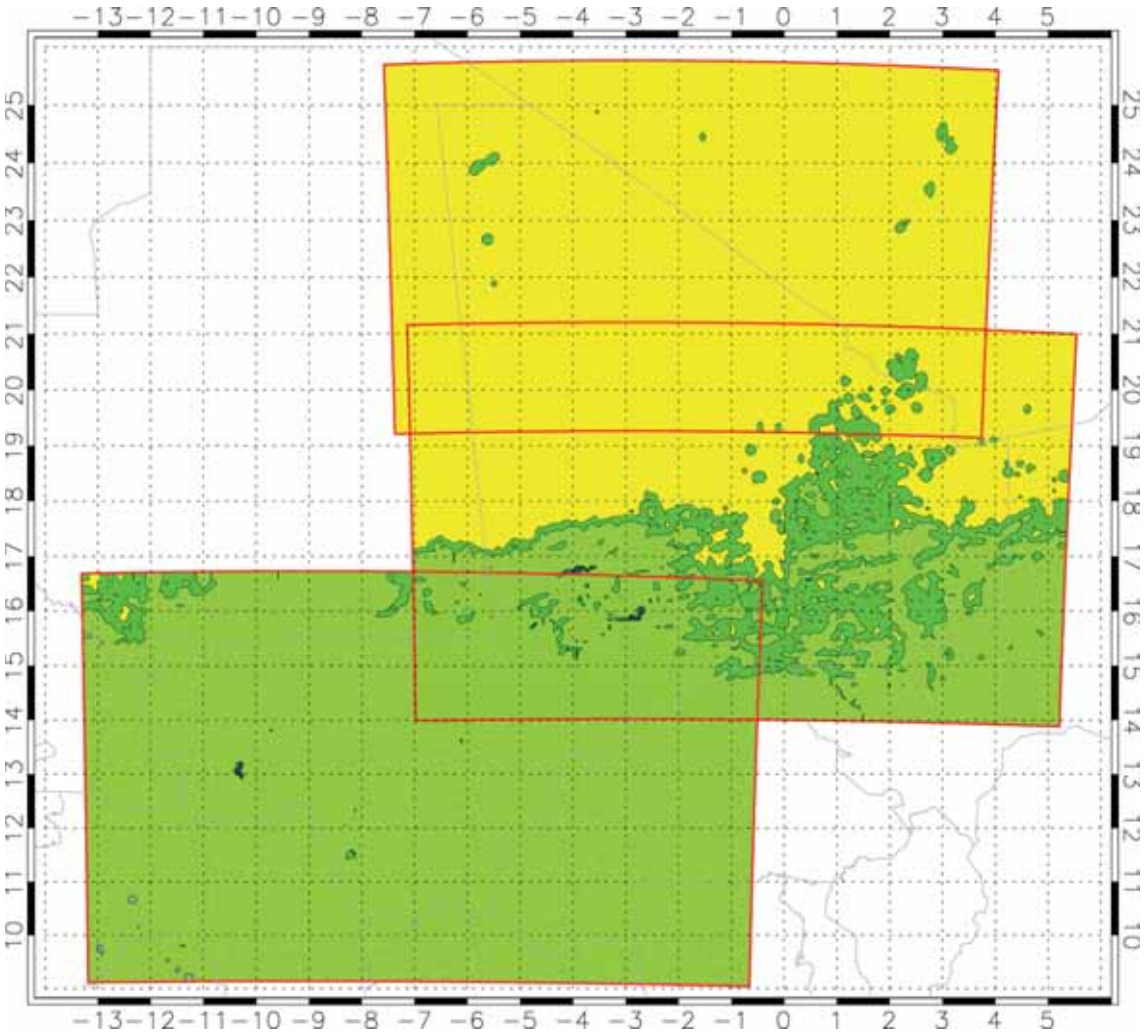

Figure 3.2: The surface aerodynamic roughness length for the three modelling domains at a resolution of 7.5 km. , The domains' boundaries are marked by the red lines. The x and y axes use longitude and latitude as in figure 1.1. Colour key: Blue z_0 = 0.0002 m, yellow 0.0002 < z_0 < 0.002 m, bright green 0.002 < z_0 < 0.020 m, green 0.020 < z_0 < 0.2 m, grey 0.2 < z_0 < 0.60 m.. The roughness data is derived from the United States Geological Survey (USGS) Global Land Cover Classification.

3.3 Initial Meteorological Data

Atmospheric data for the modelling initialization is obtained from the NCEP/NCAR reanalysis data-set on a longitude-latitude grid with a resolution of 2.5 x 2.5 degrees (Kalnay et al, 1996). The data can be down loaded from the internet (Internet Link [3]).

Geopotential height, temperature, humidity data from the 1000 hPa, 850 hPa, 700 hPa, and 500 hPa isobaric surfaces are used. This data is converted into geostrophic wind and virtual potential temperature

values for 0 m, 1500 m, 3000 m and 5500 m heights above sea level. The data is compiled into 30-year time series, covering 1977 to 2006, for use in the wind class generation programs.

3.4 Classification system

The time-series data of wind and temperature profiles derived from NCEP/NCAR reanalysis data is used to determine three sets of wind classes. One set for each of the modelling domains.

These wind class sets form representative sets of wind conditions for the region of interest. The wind classes represent different wind speeds, wind directions, and atmospheric stabilities.

For each wind class a wind class profile is defined. The wind class profiles describe how the geostrophic wind speed, wind direction, temperature and specific humidity vary with height, from 0 m to the top of the model at 5500 m for each wind class. The wind class profiles can be defined using all the data in the period 1977-2006 to give annual wind class profiles.

The Froude number is used to assess the likely impact of an obstacle, such as a hill, on wind flow. The Froude Number is $U / (h * N)$, where U is the velocity scale, h is the height scale of obstacle, N^2 is the Brunt-Väisälä frequency, where $N^2 = (g/\theta_0)(d\theta/dz)$, with $(d\theta/dz)$ being the vertical gradient of potential temperature.

For cases where the Froude number is below one, the flow tends to flow around obstacles. For cases where the Froude number is above one, the flow tends to flow over obstacles. More stable conditions tend to lead to lower Froude number flow behaviour, in which channelling between or around obstacles is more prevalent, as well as lee effects to be more persistent.

The inverse Froude number squared is used in the wind class classification system to differentiate meteorological situations that have similar wind speed and direction but different thermal stratification. The height scale used is 1500 m, the height difference between the first and second level in the wind class profile.

The three wind class sets used for this numerical wind atlas study are shown in Figure 3.3. The figures indicates the wind classes' wind speeds, directions, inverse Froude numbers squared, and frequencies of occurrence. It can be seen in Figure 3.3 that many of the wind classes come in pairs, i.e. for similar wind speed and wind direction, two wind classes are present with different Froude number. The different Froude number reflects the wind classes' different vertical temperature profiles.

(a)

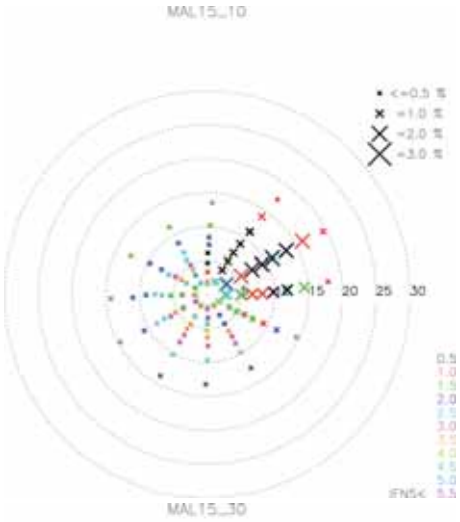

(b)

(c)

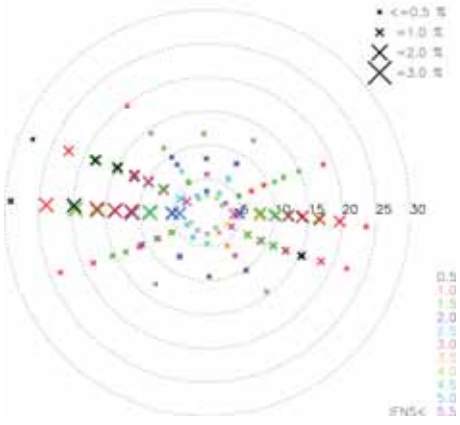

Figure 3.3: The three sets of geostrophic wind classes for (a) Northern Mali, (b) Central Mali, (c) Southern Mali based on data for the period 1977-2006. Each cross represents a forcing wind speed (distance from the centre of the diagram) and direction. The speed scale is in m/s. The size of each cross represents the probability of the wind class. The frequency scale is given in the upper right hand corner. The colour scale indicating the inverse Froude number squared (IFNS) is given in the lower right hand corner.

3.5 Post-processing

After the mesoscale simulations are complete, the results are compiled in the post-processing stage of the methodology. First, a weighted mean of the wind speeds at each mesoscale model grid point is calculated. The weightings for each wind class simulation are based on the frequencies of occurrence. This averaging operation yields a simulated resource map. Second, for each wind class simulation, the effects of elevation and roughness variation are removed with modules similar to those in the WAsP software. Then the weighted mean of the adjusted result from the wind simulations is made. This yields a wind atlas map, or generalized wind map for flat surface condition of a specified roughness.

Figure 3.4 shows a schematic diagram of the wind class simulations and the post-processing steps.

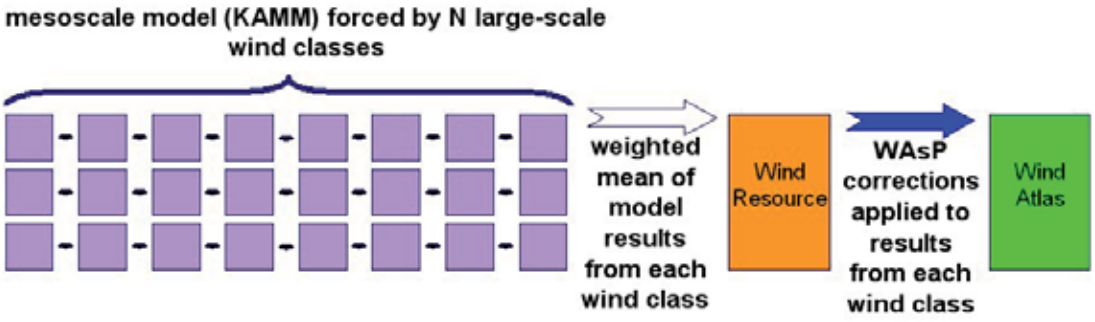

Figure 3.4: A schematic diagram showing the KAMM/WAsP numerical wind atlas methodology. In this numerical wind atlas study, N, the number of wind classes is 136, 116, and 113, for the different calculation domains.

3.6 Results

The results from the numerical wind atlas study using the KAMM/WAsP methodology can be output and utilized in two rather different ways. One way is to present the results in the form of resource maps, created in the method described above. These maps provide a good means to summarize the large amount of data generated in the study. Another way to output the results is in the form of WAsP generalized wind climate files, known as *.lib-files*, because the convention is to use the extension '.lib' in their filename.

The WAsP generalized wind climate files can be generated by the KAMM/WAsP methodology. This means that comprehensive information concerning the wind speed and direction distribution for various heights above ground level and for various surface roughness lengths can be obtained for any location within the region of interest.

WAsP generalized wind climate files have been generated on a grid with 7.5 km spacing for the region of interest. All the *.lib-files* are provided and a small program is also included to assist in the selection of the appropriate *.lib-file* by prompting for the longitude and latitude of the site of interest. This is described further in Section 3.9.

Figure 3.5 and Figure 3.6 show the annual mean simulated wind speed and power density respectively for the region of interest at 50 m above surface level. These maps give an overview impression of the spatial variation of wind resources.

However for any location on the map one would not expect necessarily to have measured the same mean wind speed indicated by the map. This is because the map has been created using a surface description at 7.5 km resolution. In reality the surface will be full of details in surface elevation and surface roughness. For example, small hills and forests, pertaining to elevation and surface roughness details respectively, will not be resolved.

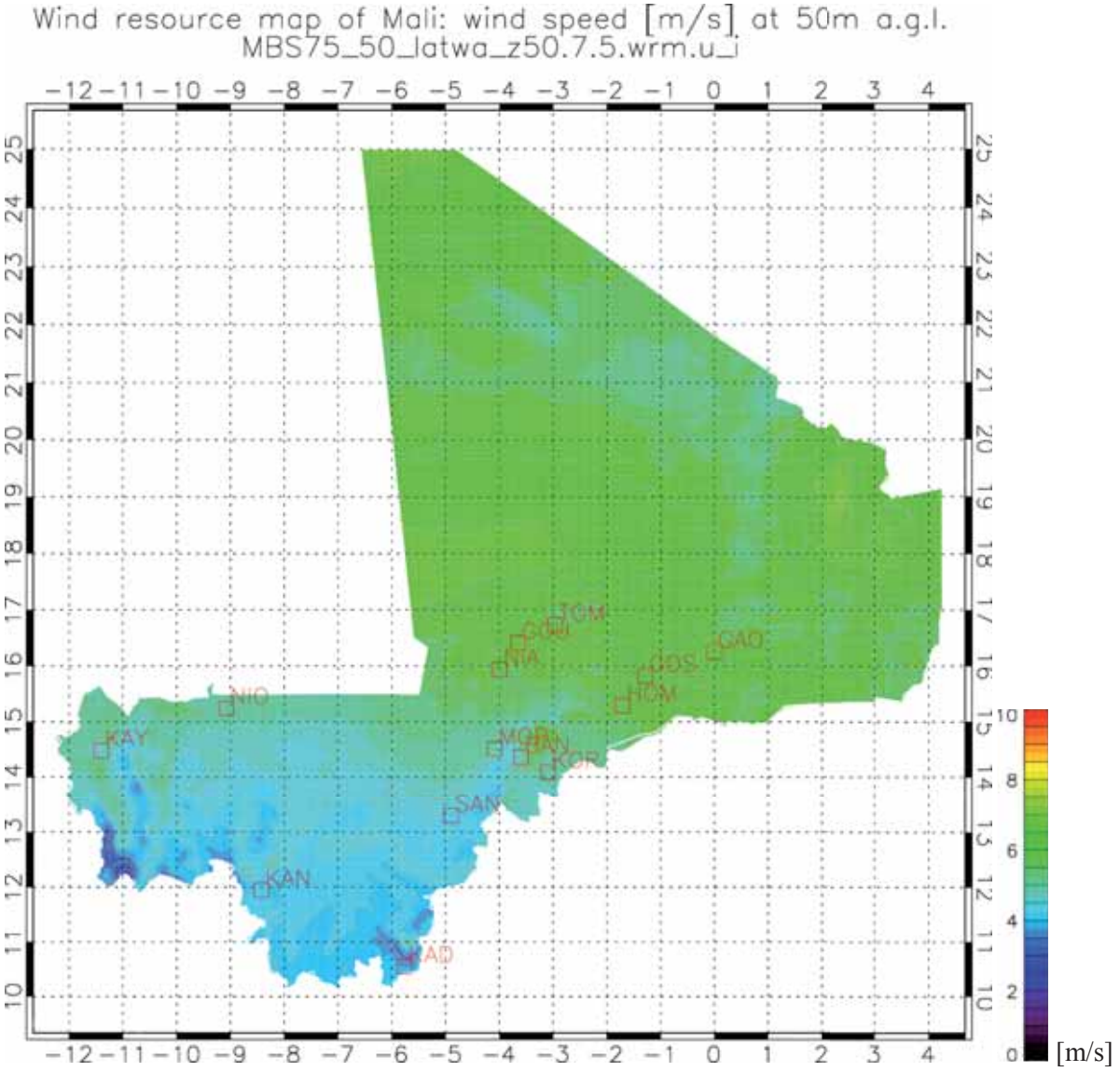

Figure 3.5: Annual mean simulated wind speed at 50 m a.g.l. The contour interval is 0.5 m/s and colour scale is in m/s. Axes are given in longitude and latitude coordinates.

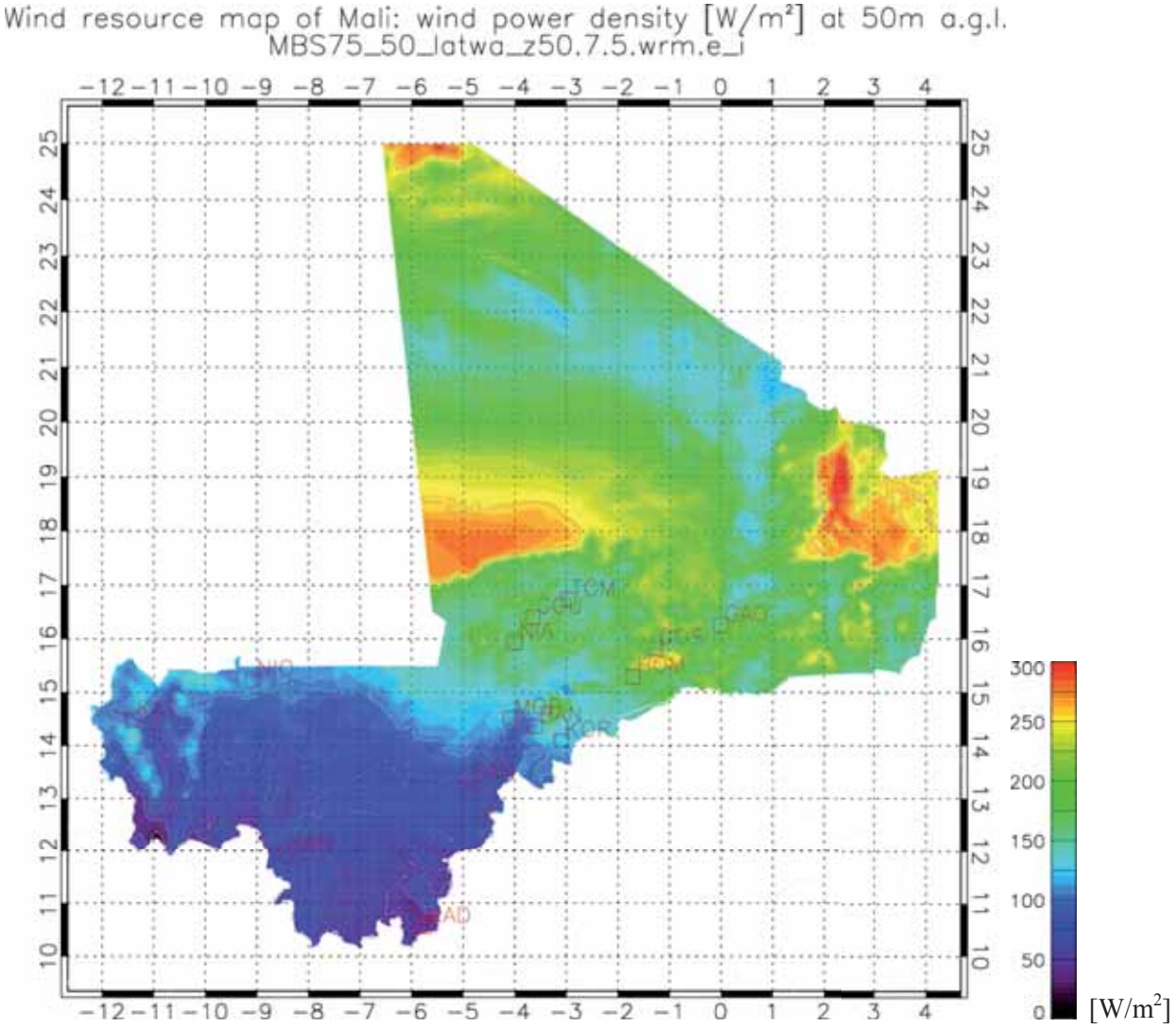

Figure 3.6: Annual mean simulated wind power density at 50 m a.g.l. The contour interval is 25 W/m^2 and colour scale is in W/m^2. Axes are given in longitude and latitude coordinates.

Figure 3.7 and Figure 3.8 show the annual mean generalized wind speed and power density respectively. These maps show the resource when the effects of resolved surface elevation and roughness change are removed. They show what the annual mean wind speed and the power density would be at 50 m above surface level for flat terrain with a uniform roughness of 0.03 m. These maps are useful because they show the mesoscale influence on wind resource, i.e. variation of resource due to phenomena other than local orographic speed-up and roughness change.

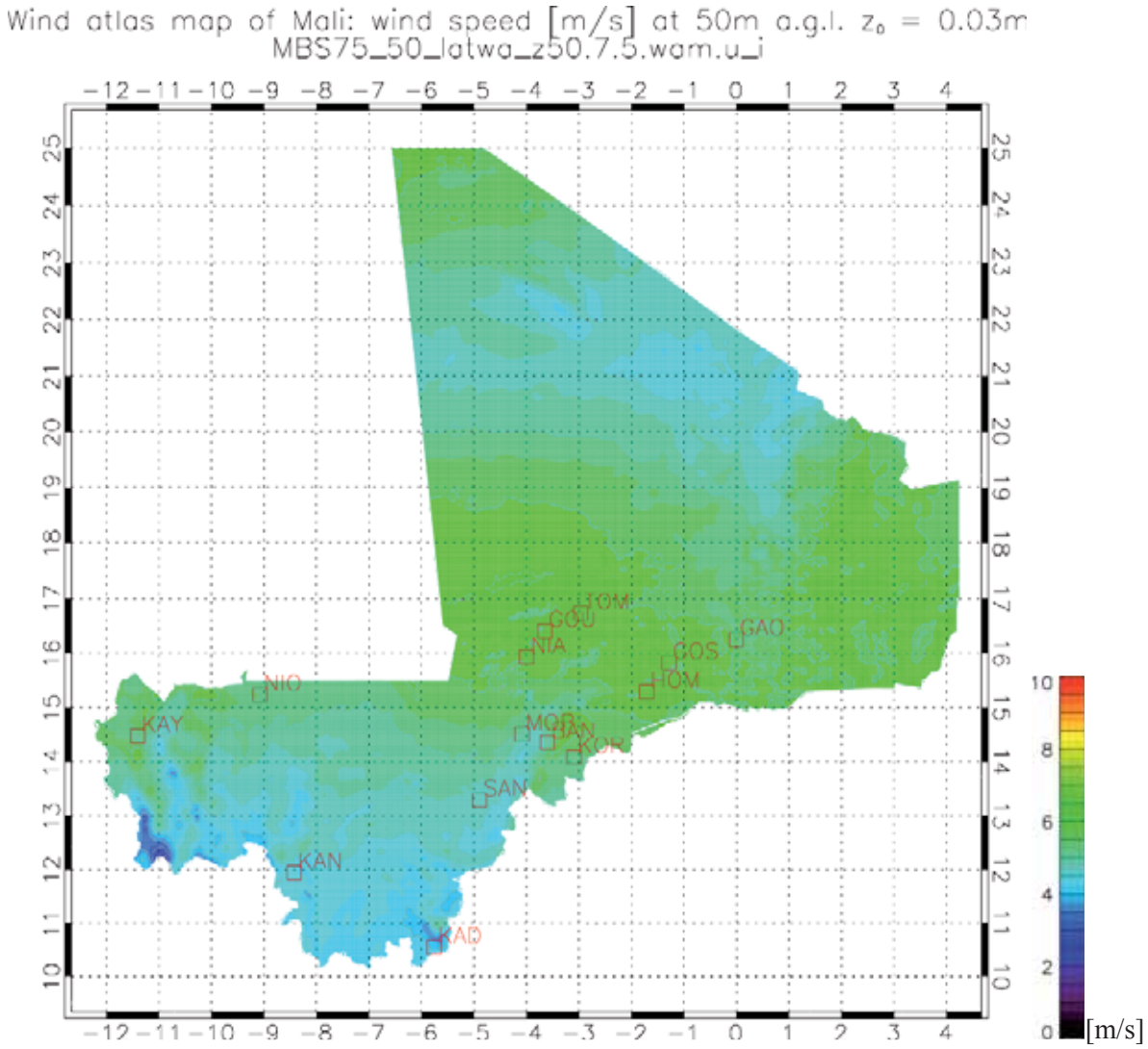

Figure 3.7: Annual mean <u>generalized</u> wind speed at 50 m a.g.l. for a flat homogeneous surface with roughness length 0.03 m. The contour interval is 0.5 m/s and colour scale is in m/s. Grey contours indicating the surface elevation, country borders and coastline. Axes are given in longitude and latitude coordinates.

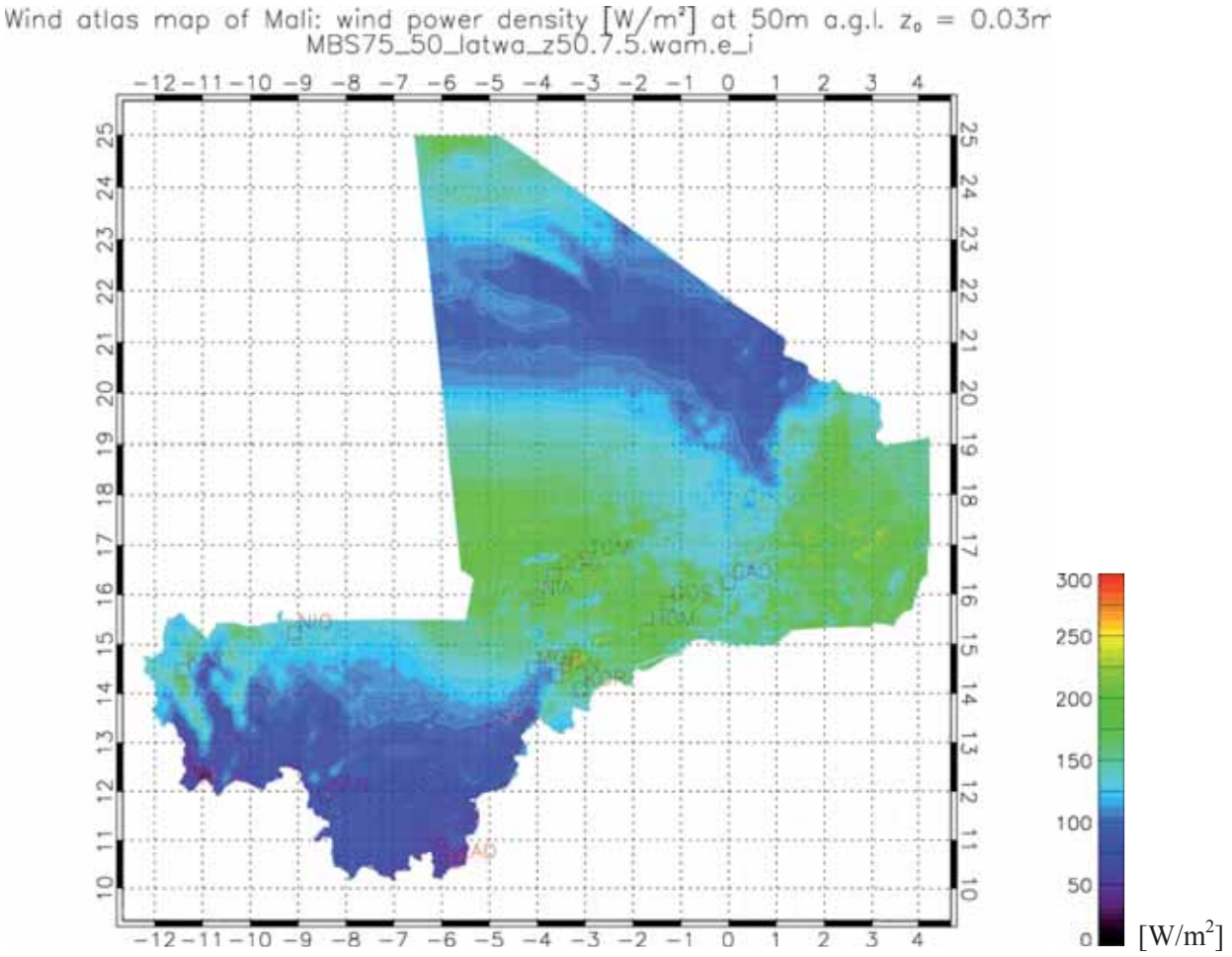

Figure 3.8: Annual mean generalized wind speed at 50 m a.g.l. for a flat homogeneous surface with roughness length 0.03 m. The contour interval is 25 W/m^2 and colour scale is in W/m^2. Grey contours indicating the surface elevation, country borders and coastline. Axes are given in longitude and latitude coordinates.

Depending on local conditions, e.g. access conditions and options for replacing diesel-based electricity, wind speeds of 5 m /s are generally considered to be the lower limit for economic feasible exploitation of wind resources. The results in Figure 3.5, show as expected a relative low (< 5 m/sec) wind resource potential in Mali, especially in the south and most populated part of the country, although exposed sites on favourably oriented ridges will give stronger mean winds. Wind speeds > 5 m/sec are prevailing in the northern part of the country, (latitude above 16 degree) including towns such as Timbuktu and Gao. Mean wind speeds of above 5 m/s are also found as far south as the Dogon plateau. Favourably exposed sites in these areas could be promising, if combined with practical utilizations possibilities.

3.7 Error and uncertainty

In this section the causes of error and uncertainty in the methodology are discussed. The uncertainty or error on the final results of the numerical wind atlas methodology should be considered as part of the study. Each step in the methodology involves approximations and uncertainties, therefore the estimation

of the final uncertainty must consider how each step may contribute to the uncertainty and characterize the impact of the error.

Contributors to the errors may include:

- Description of the large scale meteorological conditions from the NCEP/NCAR reanalysis.
    - The global NCEP/NCAR reanalysis uses a rather coarse resolution and its accuracy is better in regions of high density observations. In regions of scarcer measurement the accuracy is degraded.
    - Errors in the wind velocities may lead directly to errors in wind resource
    - Errors in temperature profiles will lead to errors in stability and Froude number, and may give rise to spurious flow behaviour in complex terrain.

- Determination of the wind class and their associated vertical profiles of geostrophic wind and temperature.
    - Breaking down a large amount of atmospheric data into approximately 120 different wind classes is a way to reduce the amount of computer resource necessary to perform the mesoscale simulations. In doing so it is possible to add new errors in the process. However great care has been taken to develop the method in which the wind classes are determined to minimize this error.
    - Certain choices for the properties of the wind classes must be made. For example, at what height should the geostrophic wind be used to define the wind classes. Careful and appropriate selection of such properties minimizes error from this step.

- Description of the surface elevation
    - The surface elevation errors may come about due to insufficient spatial resolution. One of the most serious consequences of an error in the orography is the under-representation of high terrain. For example the heights of peaks are reduced when a lower resolution is used. This may lead to incorrect interaction of flow with terrain.
    -
- Description of the surface roughness
    - The surface roughness errors may come about due to insufficient spatial resolution, and also through incorrect estimation of roughness length.

- Mesoscale modelling
    - Thermally driven winds, such as sea breezes, are known to be difficult to reproduce in the mesoscale model. Since the temperatures for land and sea surfaces are held fixed in time for each wind class it is expected that evolution of such wind phenomena are not very well reproduced.
    - The KAMM modelling assumes a uniform and steady atmospheric forcing, thus any wind features due to transient and spatially varying forcings are not accounted for well.

- Microscale modelling
    - By accounting for the local mesoscale orographic speed-up and roughness change it is possible to transform the simulation wind characteristics to generalized wind characteristics (WAsP *.lib-files*). This process may introduce some uncertainties to the generalized wind statistics.

3.8 Verification

The previous section discussed the causes of error or uncertainty. In this section the error or uncertainty is evaluated. As with most modelled data generally it is of value to verify results with measurements so as to make an assessment of the error or uncertainty of the model results. The standard procedure to do this for KAMM/WAsP results is to compare generalized wind climate statistics obtained from KAMM/WAsP and from WAsP analysis of measurement data at specific measurement locations. The verification process is actually an iterative process, in which the model system set-up is changed until the optimum model system configuration is obtained by minimizing the difference between model derived output and measurements.

Section 2 described the process of making the generalized wind climates based on measurements. There is one issue to resolve first, which is that the measurement periods were only one year in length. This does not represent a climatological period, nor the period upon which the numerical wind atlas results are based. To resolve this issue the numerical wind atlas results are recalculated by determining the wind classes weightings for the actual measurement periods used.

Figure 3.9 shows the variation of the large-scale forcing winds for the 3 mesoscale modelling domains. It can be seen that the mean large-scale forcing winds in the climatological period are slightly higher than the large-scale forcing winds in the measurement periods. Thus we would expect a slight underestimate of a climatological wind climate if it was based on the measurement period alone. However the difference in climatological and measurement period is accounted for, So we do not expect a bias caused by this effect in the final result. Table 3.1 shows the distribution of the measurement stations within the different modelling domains.

Table 3.1: Table indicating the location of the measurement masts within the mesoscale modelling domains used for the numerical wind atlas. It can be seen that no stations lie inside the northern domain (MBN). Also it can be seen that some stations lie in the overlap region of the central and southern domains (MBC and MBS). In these cases the "Y1" indicates the domain giving the best numerical wind atlas results, and the "Y2" indicated poorer results. The poorer results are due to the measurement mast location being closer to the domain edge. For GOS and HOM, where no verification has been carried out, it is expected that the MBC domain will give the better result.

		Mesoscale modelling domain(s)		
Site	Mast Code	MBN	MBC	MBS
Tombouctou	TOM	-	Y	-
Niafunké	NIA	-	Y1	Y2
Goundam	GOU	-	Y1	Y2
Gossi	GOS	-	Y1	Y2
Mopti/Sévaré	MOP	-	Y	Y
Hombori	HOM	-	Y1	Y2
Bandiagara	BAN	-	Y2	Y1
Koro	KOR	-	-	Y
Gao	GAO	-	Y	
San	SAN	-	-	Y
Nioro	NIO	-	-	Y
Kayes	KAY	-	-	Y
Kangaba	KAN	-	-	Y
Kadiolo	KAD	-	-	Y

In order to account for the difference in climatological and measurement period, and to make a proper comparison of the generalized wind climate for the sites, the wind classes weightings are recalculated for the measurement period, and new post-processing performed. The result is the generalized wind climates shown on the left-hand side of Figure 3.10 and Figure 3.11. These can be compared to the observation derived generalized wind climates show in the right-hand side of Figure 3.10 and Figure 3.11.

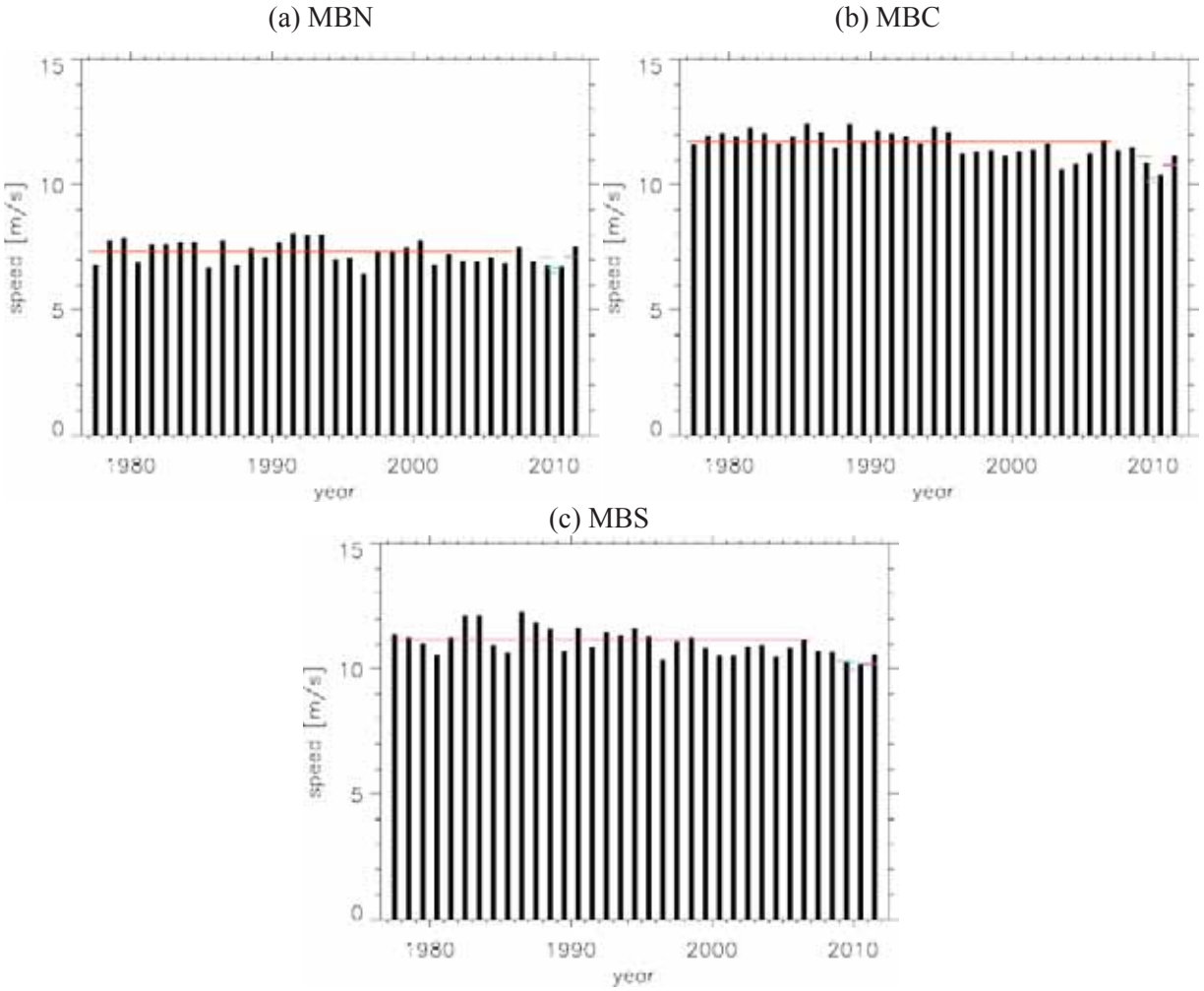

Figure 3.9: Graphs showing the annual mean geostrophic wind speed pertaining to the 3 mesoscale modelling domains(a) the northern domain, MBN, (b) the central domain, MBC, and (c) the southern domain, MBS, for the years 1977-2011. The red line indicates the mean for the period 1977-2006, which is the period the wind atlas climatology is calculated for. The other short coloured lines indicate the mean for four1-year measurement periods used and listed in Table 2.3.

(a) Gao (GAO)

NWA

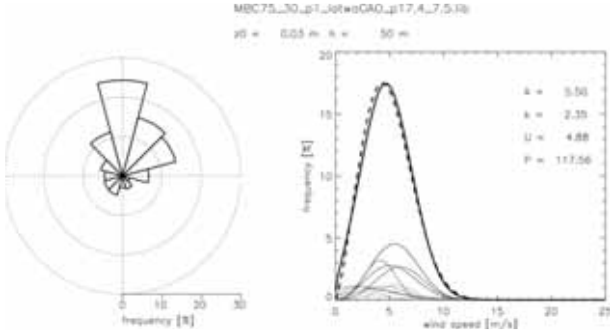

OWA

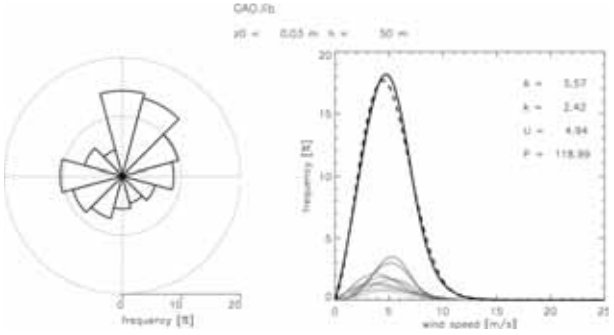

(b) Goundam (GOU)

NWA

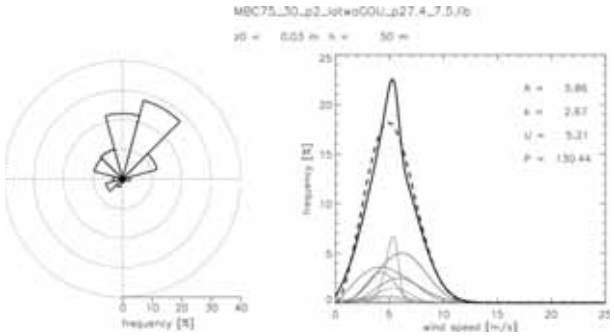

OWA

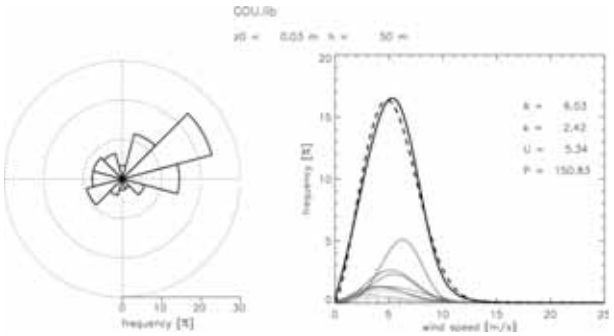

(c) Niafunké (NIA)

NWA

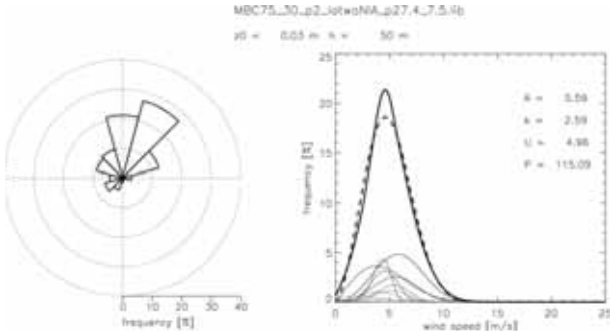

OWA

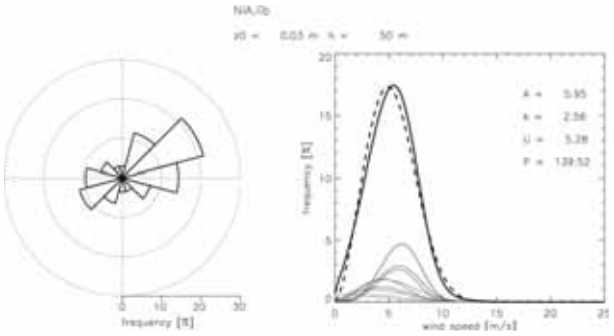

(d) Tombouctou (TOM)

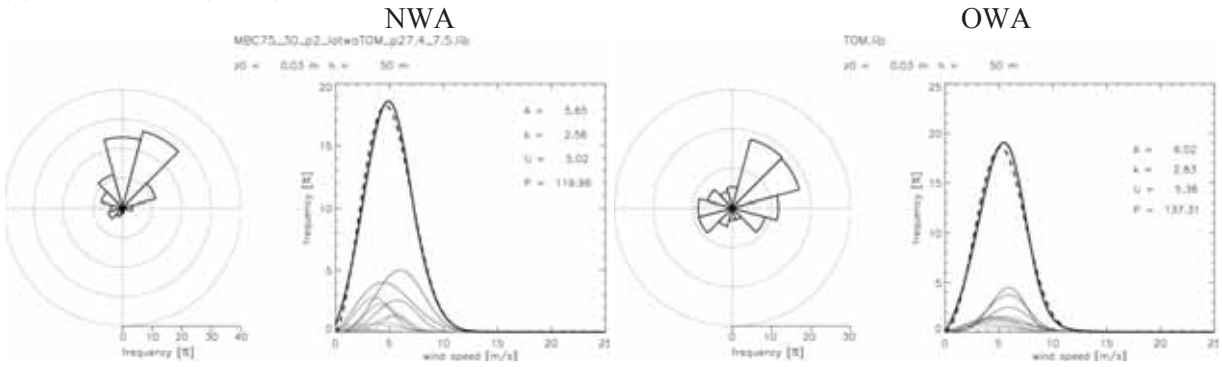

Figure 3.10: Comparison of numerical wind atlas (NWA) (left) and observation wind atlas (OWA) (right) generalized wind climate calculates for the measurement sites at 50 m in the central domain (MBC) for standard conditions, flat terrain of homogeneous 3 cm roughness length. The wind rose plots give the direction frequency distribution and the line graphs indicate the wind speed distributions. The faint lines indicate the wind speed distributions for separate directions sectors. The bold solid line indicates the emergent wind speed distribution, i.e. sum of sectorwise distributions. The bold dashed line indicates the Weibull distributions of the total wind speed distributions. The printed values give the total wind speed distribution Weibull scale parameter (A), shape parameter (k), mean annual wind speed (u) in m/s and the power density (P) in W/m^2.

(a) Mopti/Sévaré (MOP)

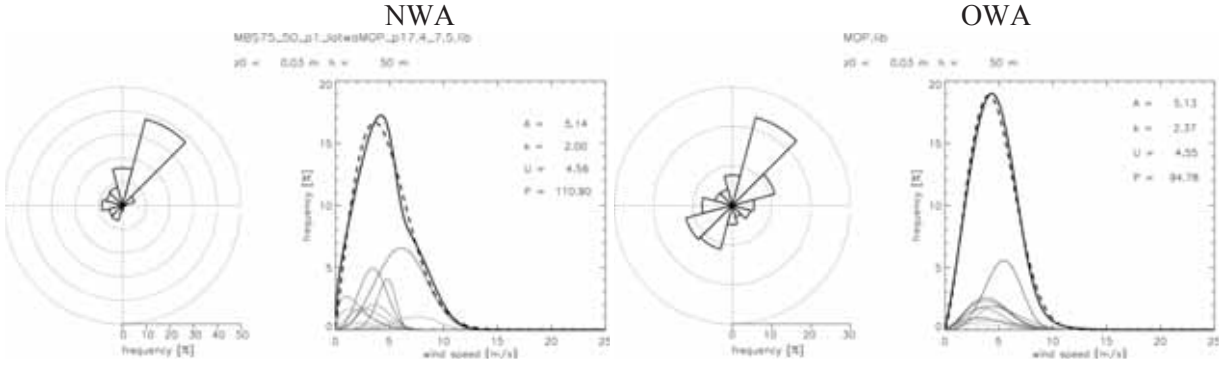

(b) Bandiagara (BAN)

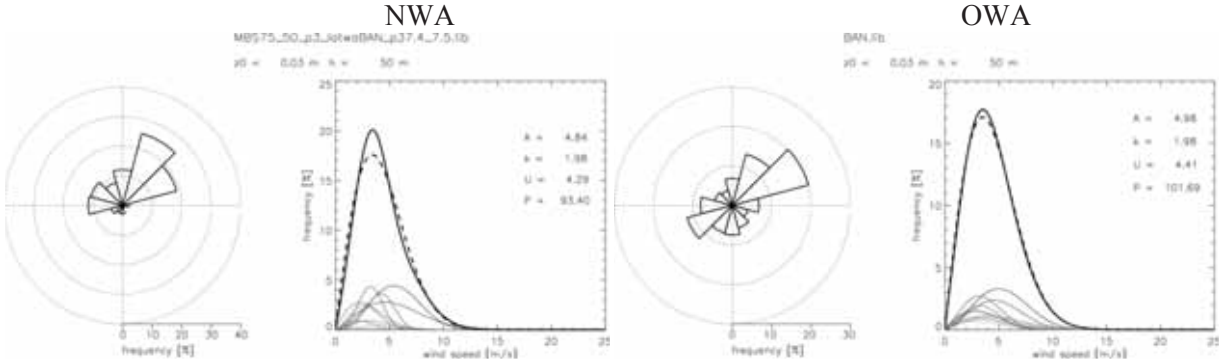

(c) Koro (KOR)

NWA

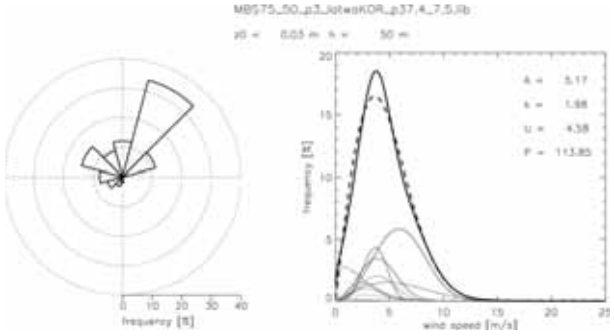

OWA

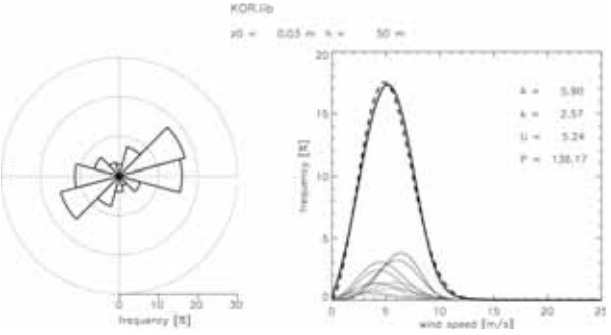

(d) San (SAN)

NWA

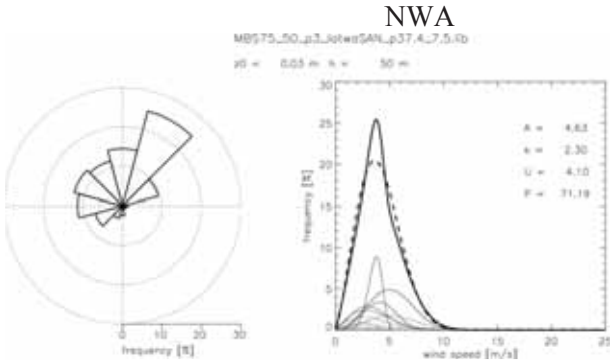

OWA

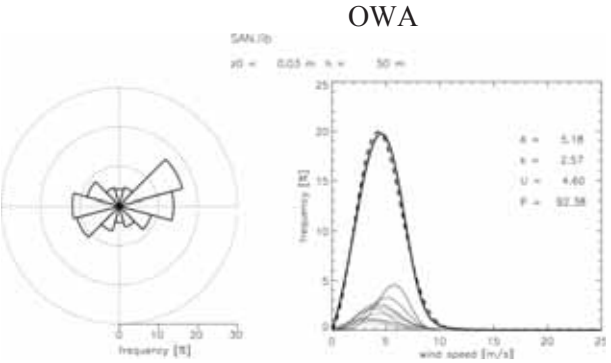

(e) Kadiolo (KAD)

NWA

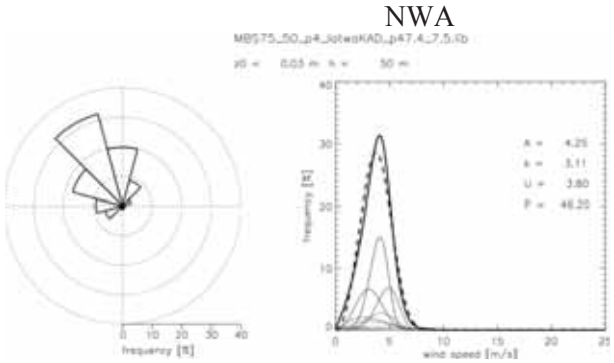

OWA

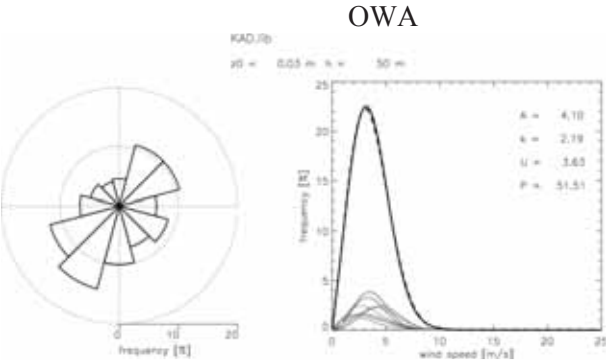

(f) Kangaba (KAN)

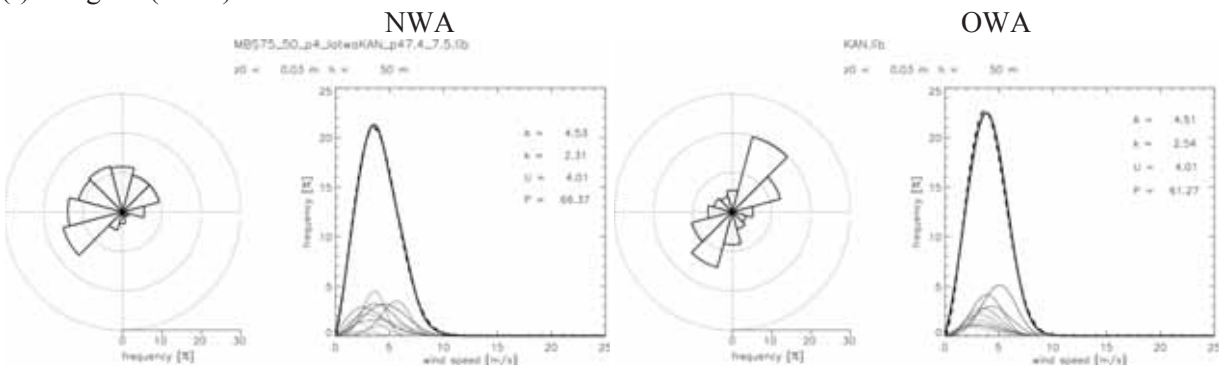

(g) Kayes (KAY)

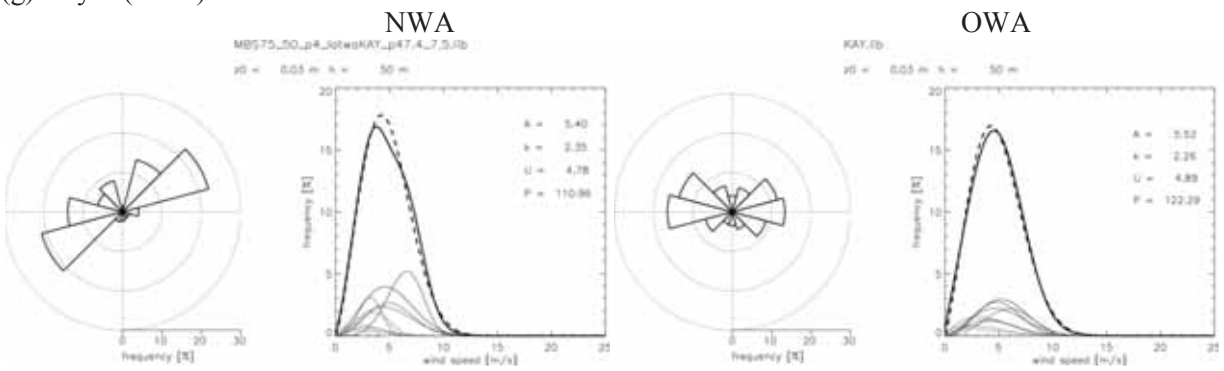

(h) Nioro (NIO)

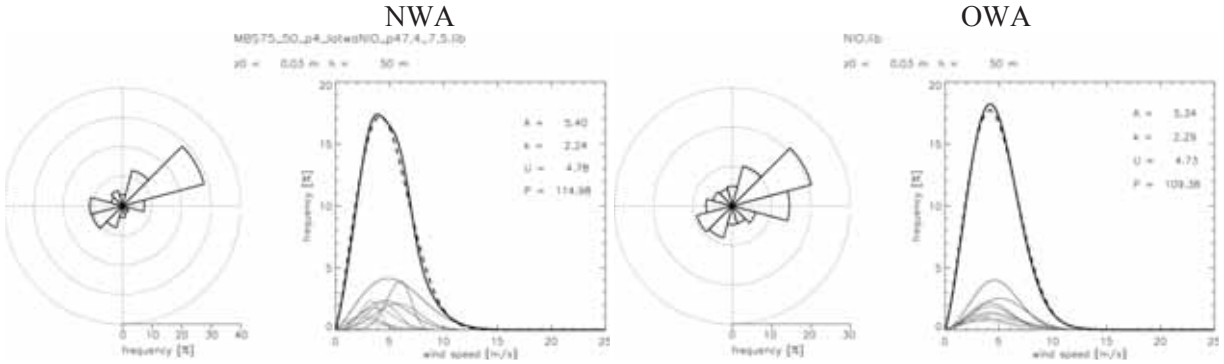

Figure 3.11: Comparison of numerical wind atlas (NWA) (left) and observation wind atlas (OWA) (right) generalized wind climate calculates for the measurement sites at 50 m in the southern domain (MBS) for standard conditions, flat terrain of homogeneous 3 cm roughness length. The wind rose plots give the direction frequency distribution and the line graphs indicate the wind speed distributions. The faint lines indicate the wind speed distributions for separate directions sectors. The bold solid line indicates the emergent wind speed distribution, i.e. sum of sectorwise distributions. The bold dashed line indicates the Weibull distributions of the total wind speed distributions. The printed values give the total wind speed distribution Weibull scale parameter (A), shape parameter (k), mean annual wind speed (u) in m/s and the power density (P) in W/m^2.

In general the qualitative agreement of the wind direction distributions (wind roses) between the numerical wind atlas and observational wind atlas is good. The poorest direction distribution agreement is for Kadiolo. Here the mean wind speed is rather low, and it is very often difficult to model the winds direction in these cases. Typical results from KAMM/WAsP give wind direction distributions that are more concentrated than the measurement derived direction distributions (as in the case of Mopti/Sévaré, MOP), and the dominant direction may be displaced by one direction sector (30 degrees) (as in the case of Goundam, GOU, and Kayes, KAY, amongst others).

A more quantitative assessment of the numerical wind atlas is offered by comparing the mean wind speed of the generalized climates for the measurement sites based on the numerical wind atlas and the observational wind atlas. The summary of this comparison is given in Table 3.2. The mean relative difference or error is -3.3 % (a slight negative bias, or underestimate) and the mean absolute error is 4.3%. This is very much in accordance with typical values reached for verification studies in other projects. Previous numerical wind atlas studies using the KAMM/WAsP method and employing verification have demonstrated uncertainty of wind speeds at 50 m above ground level of between approximately 5% and 15% (Badger et al, 2011, Mortensen et al, 2005 and Frank et al, 2001). The lower uncertainty pertaining to relatively simple terrain and the higher value pertaining to complex terrain, i.e. mountainous areas and sites. Table 3.3 gives the verification statistics, as in Table 3.2, but using the lower anemometer instead. The overall error characteristics are similar to the upper anemometer. The measurement sites Koro and San exhibit the largest errors.

Table 3.2: Verification table comparing the generalized wind climate mean wind at 50 m at the listed measurement sites derived from observational wind atlas (OWA), based on the upper anemometers (40 m or 50 m) and from the numerical wind atlas (NWA) for standard condition, flat terrain of homogenous 3 cm roughness.

Location	Mast code	OWA [m/s]	NWA [m/s]	Difference [m/s]	Relative difference %	Absolute difference %	Configuration
Bandiagara	BAN	4.42	4.29	-0.13	-2.94	2.94	MBS
Gao	GAO	4.94	4.88	-0.06	-1.21	1.21	MBC
Goundam	GOU	5.34	5.21	-0.13	-2.43	2.43	MBC
Kadiolo	KAD	3.63	3.79	0.16	4.41	4.41	MBS
Kangaba	KAN	4.00	4.01	0.01	0.25	0.25	MBS
Kayes	KAY	4.89	4.78	-0.11	-2.25	2.25	MBS
Koro	KOR	5.24	4.59	-0.65	-12.40	12.40	MBS
Mopti/Sevaré	MOP	4.55	4.56	0.01	0.22	0.22	MBS
Niafunké	NIA	5.28	4.96	-0.32	-6.06	6.06	MBC
Nioro	NIO	4.73	4.78	0.05	1.06	1.06	MBS
San	SAN	4.60	4.10	-0.50	-10.87	10.87	MBS
Tombouctou	TOM	5.36	4.96	-0.40	-7.46	7.46	MBC
				Mean	**-3.31**	**4.30**	

Table 3.3: Verification table comparing the generalized wind climate mean wind at 50 m at the listed measurement sites derived from observational wind atlas (OWA), based on the lower anemometers (22 m or 30 m) and from the numerical wind atlas (NWA) for standard condition, flat terrain of homogenous 3 cm roughness.

Location	Mast code	OWA [m/s]	NWA [m/s]	Difference [m/s]	Relative difference %	Absolute difference %	Configuration
Bandiagara	BAN	4.43	4.29	-0.14	-3.16	3.16	MBS
Gao	GAO	4.87	4.88	0.01	0.21	0.21	MBC
Goundam	GOU	5.25	5.21	-0.04	-0.76	0.76	MBC
Kangaba	KAN	3.70	4.01	0.31	8.38	8.38	MBS
Kayes	KAY	4.94	4.78	-0.16	-3.24	3.24	MBS
Koro	KOR	4.98	4.59	-0.39	-7.83	7.83	MBS
Mopti/Sevaré	MOP	4.42	4.56	0.14	3.17	3.17	MBS
Niafunké	NIA	4.96	4.96	0.00	0.00	0.00	MBC
Nioro	NIO	4.56	4.78	0.22	4.82	4.82	MBS
San	SAN	4.31	4.10	-0.21	-4.87	4.87	MBS
Tombouctou	TOM	4.71	4.96	0.25	5.31	5.31	MBC
				Mean	**0.18**	**3.80**	

3.9 Application of data using WAsP

The real added value element of the KAMM/WAsP numerical wind atlas methodology is the ability to apply the derived generalized wind atlas data at the microscale using the WAsP software. This allows the WAsP user to make pre-feasibility calculations for any location covered by the numerical wind atlas, and to make estimates for annual energy production given specific turbine type and characteristics. This sections gives a demonstration of this applications.

First the user must assess the correct generalized wind climate data for a given location. This data is contained in a so-called lib-file. Mali is covered by a grid of libfiles with a 7.5 km spacing, making up 10s of thousands of lib-files.

There are two methods to access the generalized wind climate data for Mali.

Method 1

For offline access, to assist the user a simple program is provided for download from the project website (www.frsemali.org). By running this program the user is prompted for the location of interest's longitude and latitude, and the program copies the relevant lib-file containing the generalized wind climate data into convenient folder. A screenshot of this application is shown in Figure 3.12. The project website also includes a guide to using the offline lib selection tool.

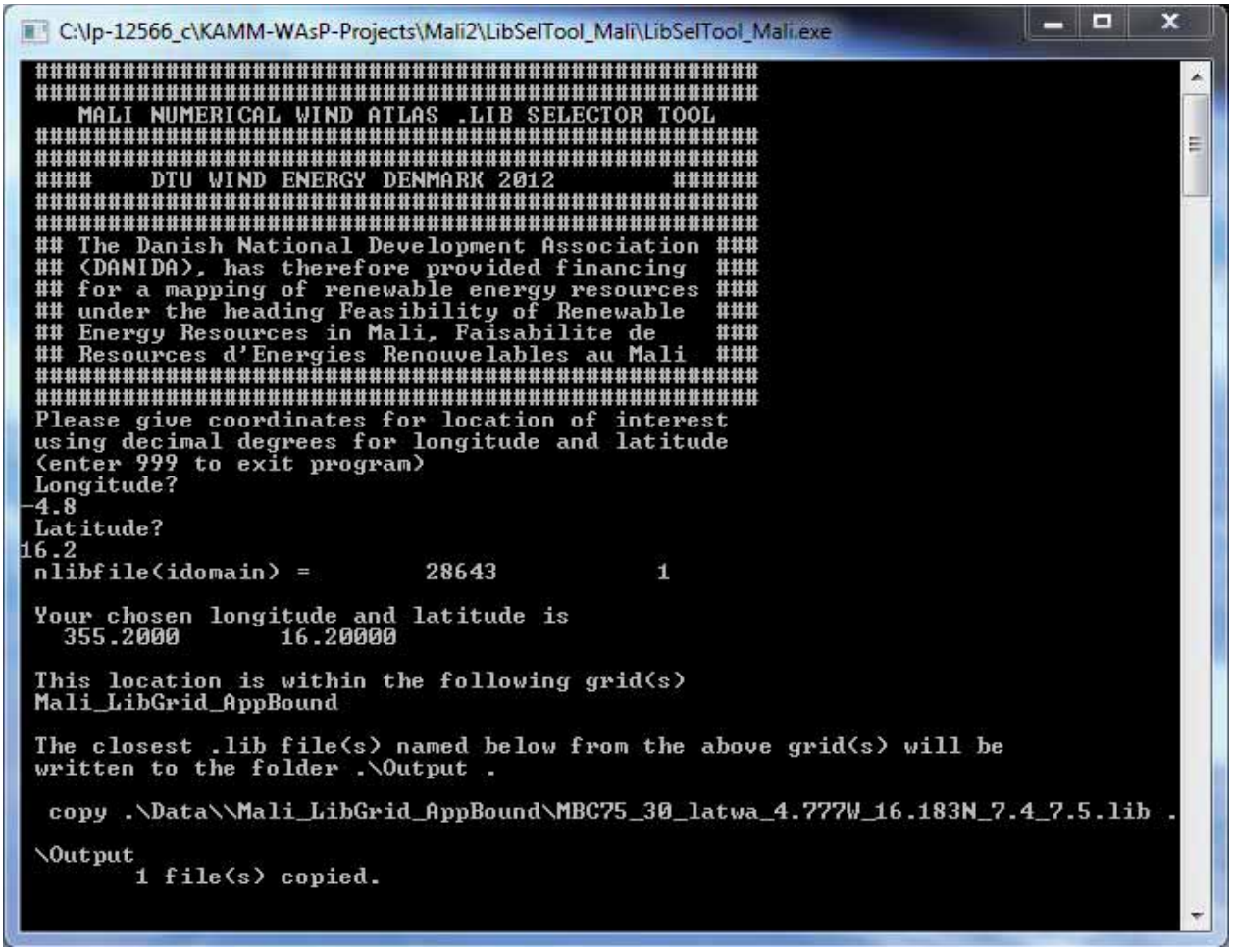

Figure 3.12: Screen shot of the lib-file selection tool.

Method 2

For online access, an alternative lib-file selector is available. It is called Tadpole and uses a Google Earth plug-in to allow the user to navigate, select a location of interest and download the generalized wind climate data. A link to the Tadpole server will be given on the project website (www.frsemali.org). A screen shot of Tadpole is given in Figure 3.13. The project website also includes a guide to using Tadpole.

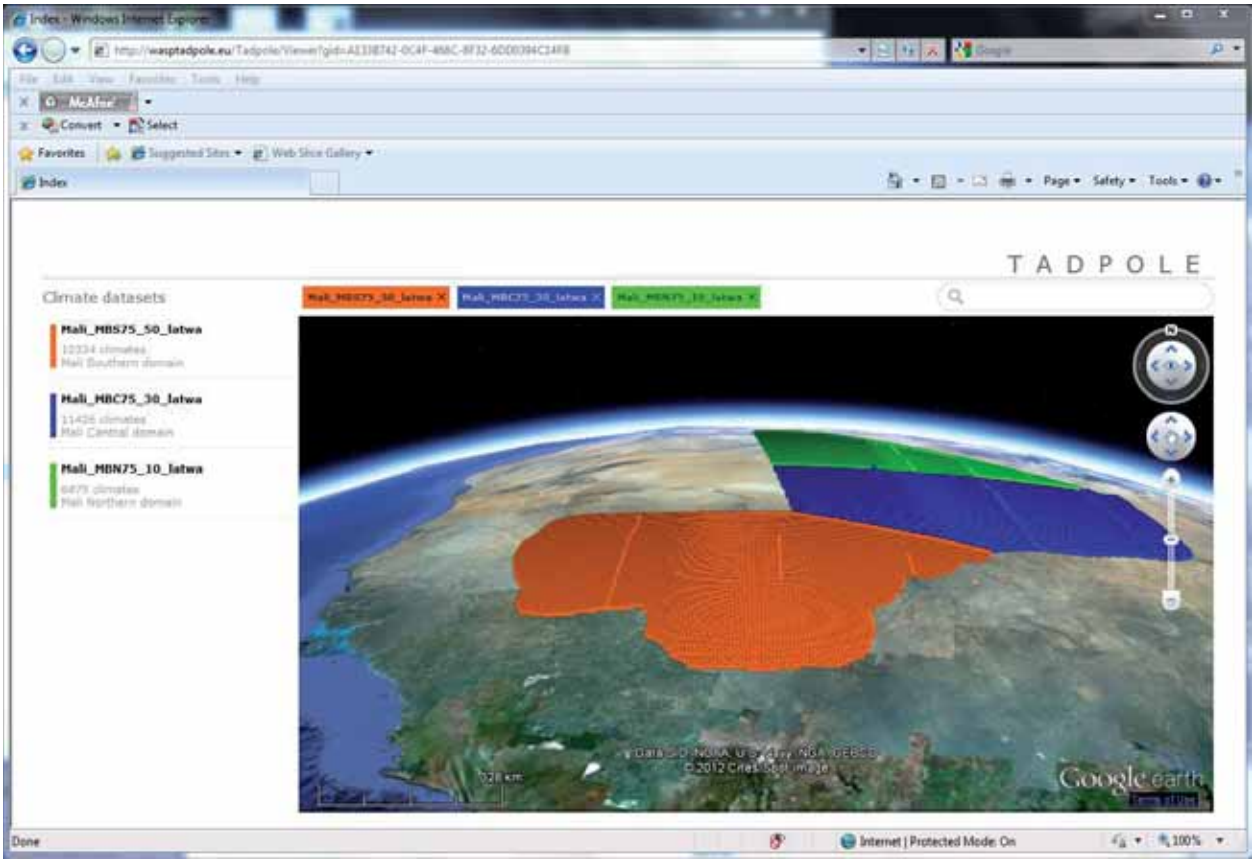

Figure 3.13: Screen shot of the lib-file selection tool Tadpole over Mali. Orange, blue and green dots indicated lib-file locations. The user can navigate, zoom, and search the map, and by clicking on a dot allows the user to download the lib-file so that it can be applied in WAsP.

WAsP

Once downloaded, the lib-file can be used in the WAsP software to carry out microscale modelling. Figure 3.14 shows a screen shot of the WAsP results displayed in Google Earth. This display functionality is part of WAsP. The application shown has been used to calculate the variation in the annual energy production over terrain south of Kayes. The software is very powerful as a tool to locate potential sites for wind turbines away from the measurement locations, and estimate the annual energy production of particular wind turbines by combining the information about directional wind speed distribution with the wind turbine power curve.

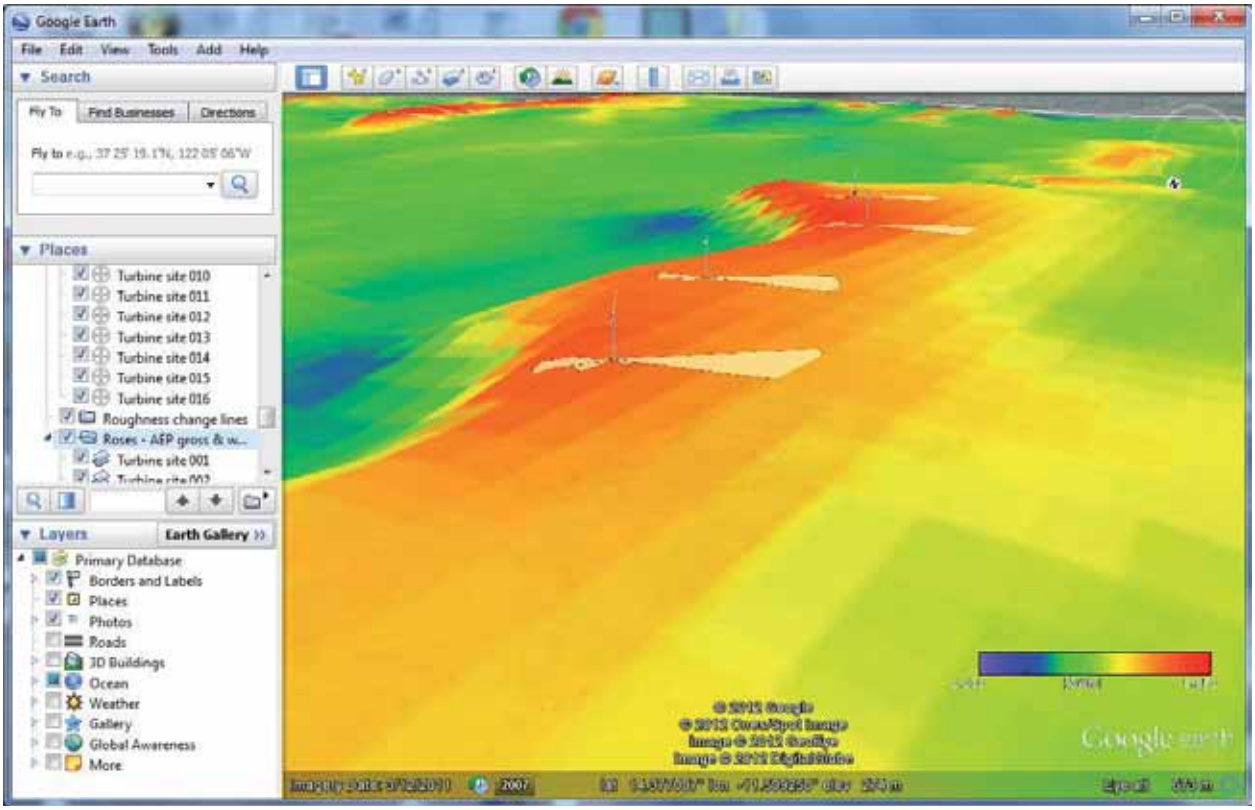

Figure 3.14: Screen shot showing the WAsP software being used to calculate annual mean wind speed at 70 m a.g.l for a 4.5 km by 4.5 km area at 100 m resolution. The area includes the measurement station (near western edge) and a hypothetical wind turbine site (north-eastern corner). A predicted wind climate can be calculated for any location, and a estimate of the annual energy production of a wind turbine can be obtained using WAsP. The input data is generalized wind climate data from the KAMM/WAsP numerical wind atlas calculation. This calculation is an example only. Surface roughness used is 0.02 m everywhere. A site survey is needed to add more topographical detail to calculation map.

3.10 Summary

The wind resource has been estimated for all of Mali at 7.5 km resolution using the KAMM/WAsP numerical wind atlas methodology. Three domains were used to cover entire country and three sets of wind classes used to capture change in large scale forcing over country. The final output includes generalized climate statistics for any location in Mali, giving wind direction and wind speed distribution. The modelled generalized climate statistics can be used directly in the WAsP software. The WAsP software then allows the inclusion of high resolution topographical information. WAsP can then used as a tool for verification studies of the KAMM/WAsP data, and for feasibility studies by calculating wind turbine annual power production estimates for any location.

The numerical wind atlas was verified against 12 measurement sites where 1-year of data had been collected. Allowance for the short measurement period within the methodology provides a means to compare the numerical derived atlas with the measurements. A mean absolute error of 4.3 % was

determined. This level of uncertainty is within the expected uncertainty for the KAMM/WAsP methodology, as experienced in other projects in other parts of the world.

The preliminary results show a wind resource, which is relatively low, but which under certain conditions may be economically feasible, i.e. at favourably exposed sites, giving enhanced winds, and where practical utilization is possible, given consideration to grid connection or replacement or augmentation of diesel-based electricity systems.

3.11 Acknowledgments

NCEP/NCAR reanalysis data are provided by the National (USA) Center for Environmental Prediction (NCEP) and the National (USA) Center for Atmospheric Research (NCAR). SRTM data is provided by the National (USA) Geospatial-Intelligence Agency (NGA) and the National (USA) Aeronautics and Space Administration (NASA). The roughness data is derived from the United States Geological Survey (USGS) Global Land Cover Classification. KAMM is used with kind permission from Karlsruhe University, Germany.

4 Solar resources

4.1 Methodology

This section will provide a brief overview of the methodology applied in this study to derive monthly and yearly maps of the solar energy resource for Mali. Further details on the method and the applied data can be found in the paragraphs below.

This study relies on satellite based estimates of the available solar energy at the surface by using the "Down-welling Surface Short-wave Radiation Flux" (DSSF) product produced by the "*Land Surface Analysis – Satellite Applications Facility*" (LSA-SAF) (Internet link [1]) based on data from the geostationary Meteosat Second Generation (MSG) satellites (Schmetz el al. 2002). This product delivers an estimate of the (semi-)instantaneous shortwave flux every 30 minutes based on data from bands 1, 2 and 3 from the SEVIRI sensor onboard MSG which covers the visible and near-infrared part of the electromagnetic spectrum. These 30-minutes values are then summed to create a daily estimate of the total daily solar radiation, assuming that the instantaneous estimates are representative of the 30 minute period they cover. The daily maps are then composited to create monthly and yearly maps. In this report we work with a three year study period ranging from July 2008 to June 2011.

In order to ensure that the resulting solar maps match the local conditions in Mali, we have chosen to calibrate the satellite based estimates to the available in situ data from the area. This is done by analysing the match between in situ measurement and satellite estimates on a daily basis and subsequently calibrating the satellite data to match the absolute levels of the in situ data. The discrepancies between the in situ data and the satellite estimates are thought to be caused mainly by the atmospheric conditions locally affecting the satellite based estimates using an algorithm that is developed for use for the entire earth disk as seen by MSG. Furthermore, the match between the two datasets will also be affected by errors in the in situ data (caused by instruments noise and inaccuracies) and errors in the satellite estimate coming from various sources.

4.2 Data

The LSA-SAF DSSF product

The present study relies as mentioned on the LSA-SAF DSSF product. The product is derived from data from the SEVIRI sensor onboard the geostationary Meteosat Second Generation satellite operated by Eumetsat. Although originally designed for meteorological purposes, it has proven useful for a number of land applications due to the number of spectral channels and their position in the visible, near-infrared and thermal infrared parts of the electromagnetic spectrum. For the application for solar energy resource mapping channels 1, 2 and 3 are positioned within the spectral region where the most solar energy is emitted. These channels are centred on 0.6µm, 0.8µm and 1.6µm while the DSSF product estimates the flux in the 0.3µm to 4.0µm region. The product exploits the high temporal resolution of the SEVIRI sensor which provides data every 15 minutes, to give an estimate of the short-wave flux (every 30 minutes). This allows the method to map changes in cloud cover with a high temporal frequency over the day, which is essential as cloud cover is the most important factor determining the amount of solar energy available at the surface. The algorithm applied in the product generation is therefore also very dependent on the cloud cover information, which is also derived from the SEVIRI spectral channels (but which also include data from the mid-infrared and thermal-infrared channels). The base parameterization of the down-welling surface shortwave radiation flux ($F^{\downarrow}$) within the algorithm is the following equation:

$$F^{\downarrow} = F_0 \, v(t) \, \cos\theta_s \, T$$

Where F_0 is the solar constant (adjusted for the spectral region of the product), θ_s is the (cosine to the) solar zenith angle, *v(t)* is a factor accounting for the varying sun-earth distance depending on the day of year and *T* is the effective transmittance of the atmosphere or cloud-atmosphere system. How T is parameterized in the algorithm depend on whether a given pixel is flagged as being clouded or not. The clear sky method requires input data on the atmospheric water vapour and ozone content, the visibility as well as the dominant aerosol type. In the clouded cases, the down-welling solar flux at the surface is inversely correlated with the cloud-top reflectance in SEVIRI channels 1-3 and is estimated using an angular reflectance model and a parameterization of the cloud transmittance.

The validation report of the LSA-SAF product shows a tendency for overestimating the down-welling flux for clear sky conditions, especially at the African validation sites (all in West-Africa). This corresponds to the findings of this study as presented below.

In situ measurements of solar radiation in Mali

CNESOLER provided in situ measurements from 10 field sites in Mali, 8 of which contained measurements of incoming solar radiation (see Figure 4.1). One of these stations, Gossi, was found to be affected by an instrument problem in January 2009 and was therefore excluded from the analysis. The rest of the stations provide data for different parts of the study period, with the latest data available being from October 18th 2011. The stations provide measurements at a 10-minute interval throughout the day but neither stations cover the entire period. For the use in this study, 5 stations where selected for the calibration of our method, while 2 stations (Bandiagara and Gao) were retained for validation purposes. Which stations to use for calibration were decided randomly. For all sites, the instrument used was specified as being a Licor Pyranometer. In situ measurements using pyranometers are usually of good quality, although the lack of cleaning and sensor drift might affect accuracy over time.

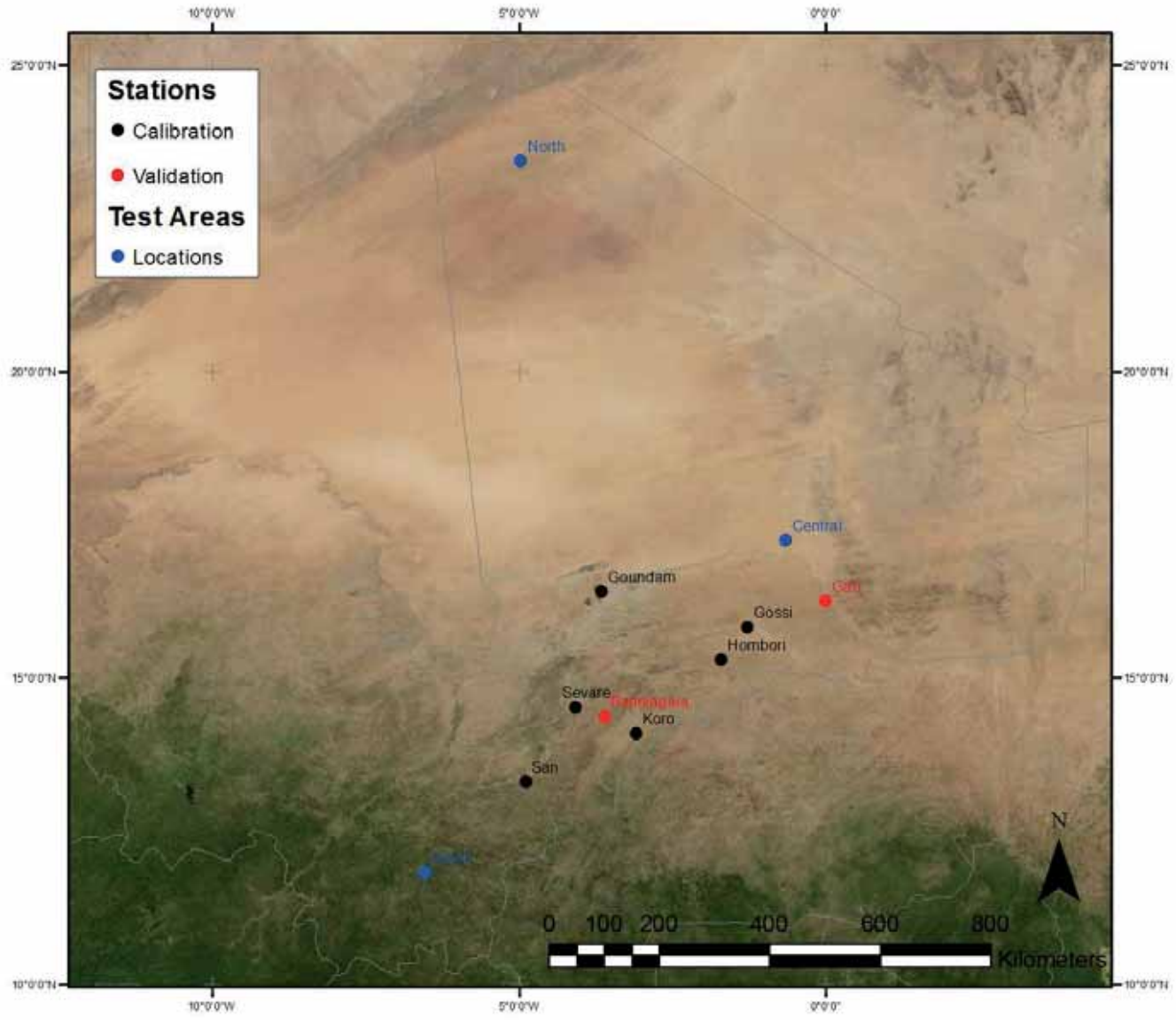

Figure 4.1: Locations of the 8 field stations for which in situ measurement of incoming shortwave radiation were available. Also shown in blue is the areas used to represent the northern, central and southern cases in the validation section.

Gap-filling

The time series of 30-minute LSA SAF DSSF contains a number of data gaps, which have to be accounted for when producing daily and monthly sums. Gap-filling was in this case done in a number of steps to ensure overall data consistency. We only treated the 30-minute products between 05:00 and 19:00 UTC as slots outside this period do not contribute to the daily sums for Mali.

1) Single slot gaps in the 30 minute data were filled by linear interpolation. This will only introduce very little uncertainty in the daily sums, unless the missing gap is located right at solar noon.
2) Daily sums were calculated for all days with a complete data record (a total of 29 30-min slots).

3) For days with missing data, the daily sum was linearly interpolated using data from two days before and two days after (with equal weights assigned to the four days) where possible.
4) For days where the method in step 3 was not possible (due to data from the four adjacent days not being available), a manual decision was made on a day-by-day basis to either gap fill the missing 30-min slots within the day, or to use three or four of the closest daily-sums to interpolate the daily value.

The total time series from 2008-07-01 to 2011-06-30 totals to 1095 days, giving a potential number of 30-minute slots of 31755. Out of these 30742 (96.8%) was available from LSA-SAF and 99 of the missing files where filled by step 1. Step 2 produced 976 daily images (89%) while steps 3 and 4 combined accounted for 119 days.

4.3 Calibration

Firstly, the agreement between the daily images produced from the LSA-SAF product and the in situ measurements at the five selected locations was analysed. This was done by investigating time-series plots of the two data series (for each site) as well as scatter plots. Note that data was only included from either source if all data was available for a given day. This means that days that required gap-filling as described above, were not included in the comparisons and subsequent calibration.
Figure 4.2 shows an example of the agreement between the in situ measurements and the remote sensing based estimates for the Sevare site. The agreement is good with and r^2-value of 0.89, small offset and a gain close to 1. Overall, the gains are all between 0.95 and 1.07 and the r^2-values are in the range between 0.75 and 0.89 (when excluding the obviously erroneous data – e.g. data from the second half of the time series at the Gossi-site). When analysing a time series plot of the two data series (see Figure 4.3 top), it is apparent that there are seasonal trends in the agreement between the two types of measurements. It is obvious that the LSA-SAF estimates are generally higher than the in situ measurements and that the difference between the two is larger during summer than winter. The pattern shown in Figure 4.3 (top) is similar to the pattern found at the other sites, with the exception that the LSA-SAF values are in some cases lower that the in situ measurements during winter while they are still higher during summer. These results leads to the conclusion that although the overall agreement is good despite a slight tendency for LSA-SAF to overestimate the down-welling shortwave flux, seasonal variations in the agreement are present that require a time-dependent approach for calibration.

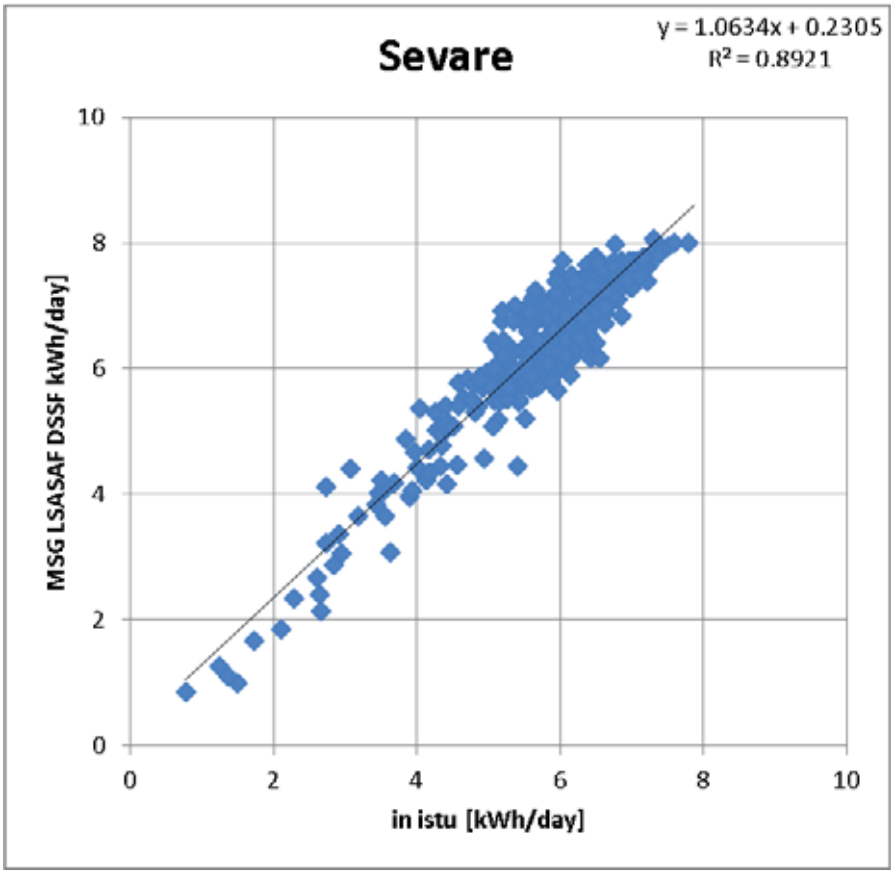

Figure 4.2: Scatterplot showing the agreement between the in situ measurements and the LSA-SAF product for the Sevare site. The green line is the 1:1 line.

A calibration-scheme was designed that account for the time-dependence of the agreement between the in situ and remote sensing estimates. All data from the five field sites were grouped by month and then compared to the remote sensing data. Regression analyses were then carried out between the two data series using standard linear least-squares regression with in situ being the independent variable and the remote sensing estimates being the dependent variable. Note that we are, by using standard least-squares regression minimize the residuals on the dependent variable, effectively assuming that the in situ data are perfect and that errors are mainly affecting the remote sensing estimates. This assumption is justified in this case by the fact that the regressions for the five analyzed stations are very similar and because of the generally very high accuracy of in situ measurements of incoming shortwave radiation.
The monthly regressions were then used to adjust the remote sensing estimates to better match the level of the in situ measurements over the year. An example of the result of the calibration can be seen in Figure 4.3, bottom. This calibration of the data will not necessarily improve the fit of the individual days, but will correct the level of the values over the entire time series. When considering data for the five stations included in the calibration for complete days only, the root-mean-square-error is reduced from 0.74 kWh/m^2/day to 0.39 kWh/m^2/day while the mean absolute error is reduced from 0.59 kWh/m^2/day to 0.30 kWh/m^2/day.

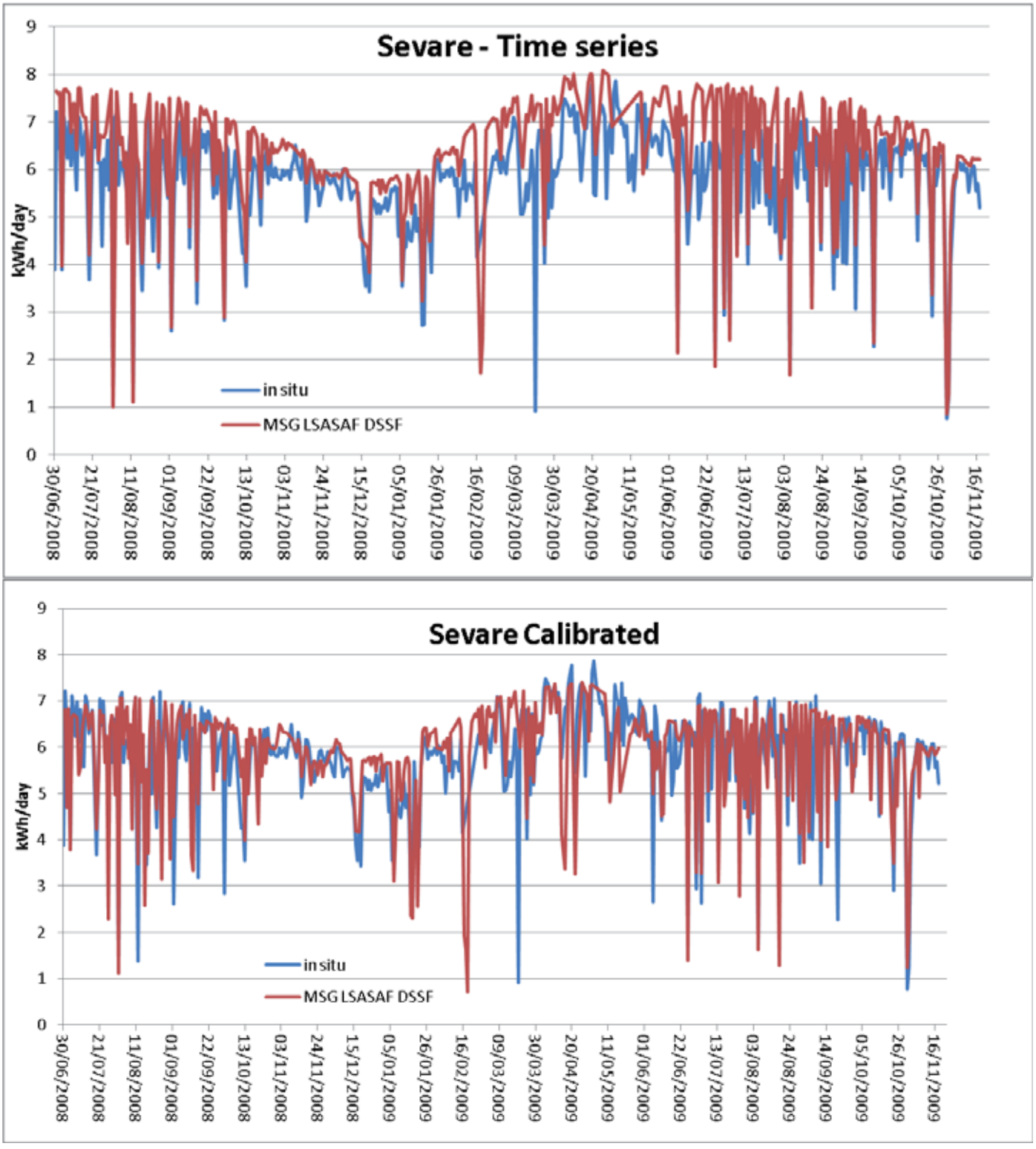

Figure 4.3: Top: Time series of the in situ and LSA data for the Sevare site. Note the seasonal differences in the agreement between the two data series. Bottom: Same time series, but with the calibrated version of the LSA-SAF data based on the monthly regressions.

4.4 Validation

Validation of the calibration described above was done using in situ data from two stations, Gao and Bandiagara, not included in the calibration. For both stations, the changes in the regression are minimal (compared to the comparisons with the raw LSA-SAF values, but with slight increases in the r^2-values from 0.80 (for both stations) to 0.83 and 0.86 respectively (see Figure 4.4). Please note that these results only include days were both in situ and a complete LSA-SAF time series were available, and thus exclude days that were gap-filled afterwards. As shown for the calibration case of Sevare above, the level of the measurements fit the LSA-SAF values better after the calibration than before due to the monthly-calibration scheme (not shown).

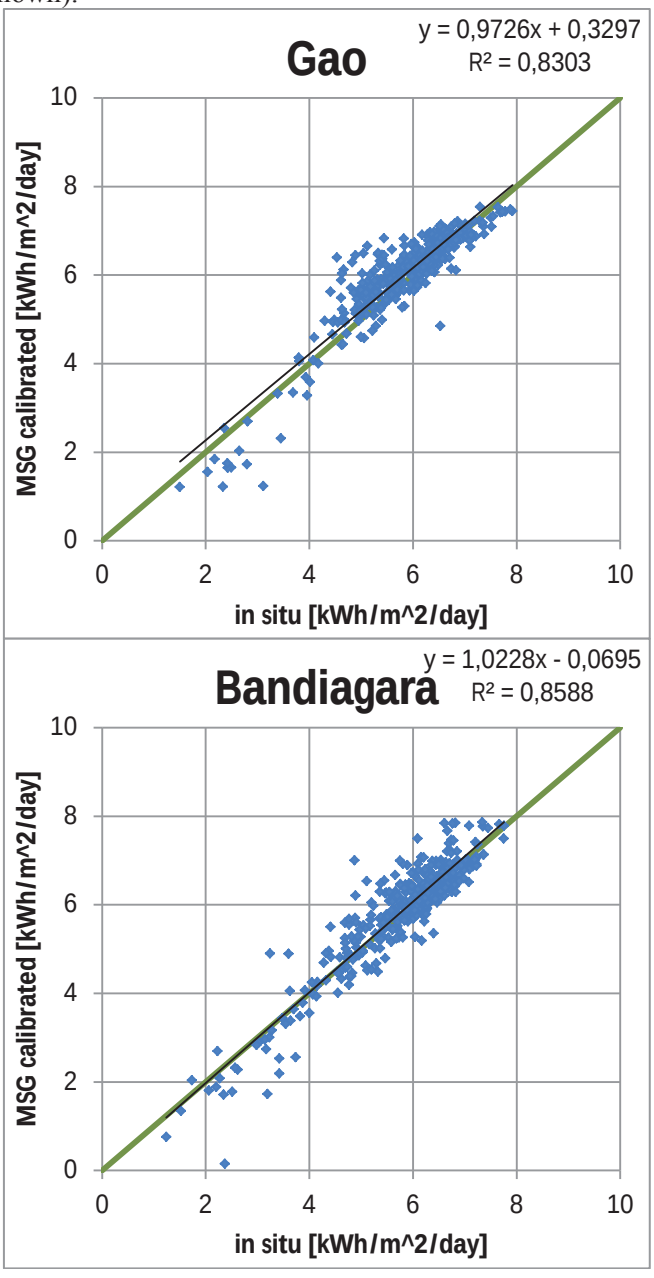

Figure 4.4: Scatterplots for the two validation sites. The green lines are the 1:1 lines and the black lines are the regression lines. Data are only included for days with complete coverage for both in situ and remote sensing data.

4.5 Solar resources

The spatial distribution of solar resources in Mali is shown in Figure 4.5 and in Figure 4.6. The figure shows the mean solar radiation for the years 2008 to 2011. Similar maps for each of the three years are included in appendix D. Note that some land cover related features are apparent in composites that cover long series. This is due to the fact that surface albedo is used in the calculations, which introduces a slight sensitivity to this parameter. When making composites covering long time periods, these small differences will accumulate and become visible in the solar maps. This is exemplified by looking at the monthly composites (in appendix D), where certain land surface features is still visible, they are much less pronounced than in the yearly or three-yearly composites.

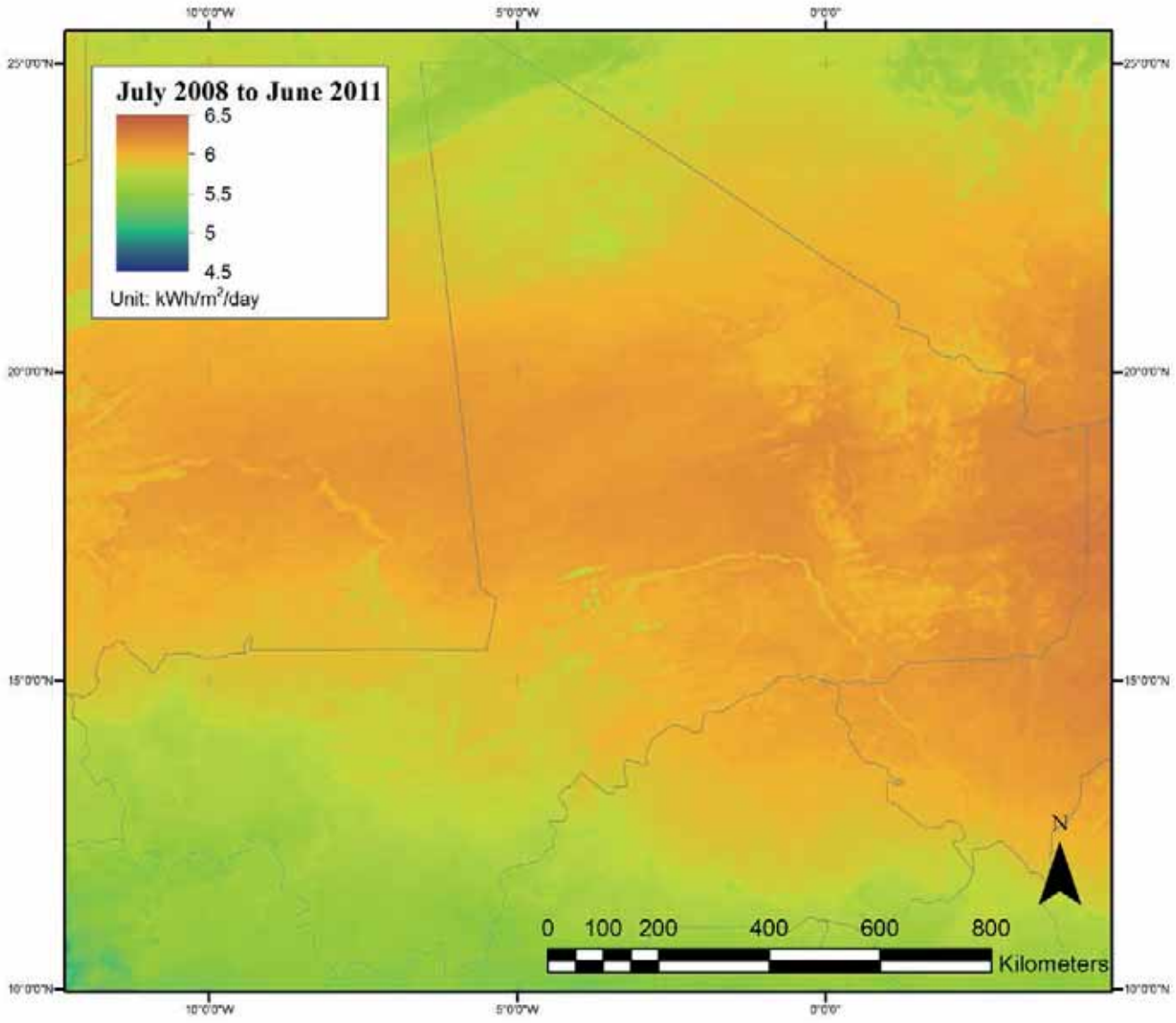

Figure 4.5: Average daily solar radiation for the period between July 2008 and June 2011. Similar maps for the three years are included in appendix D.

Figure 4.6 shows the information from Figure 4.5 in a 1 degree resolution (110*110) km. The three years average solar radiation is indicated in kWh/m2/day. Monthly and yearly maps of accumulated solar radiation are included in appendix D for the 36 months covered

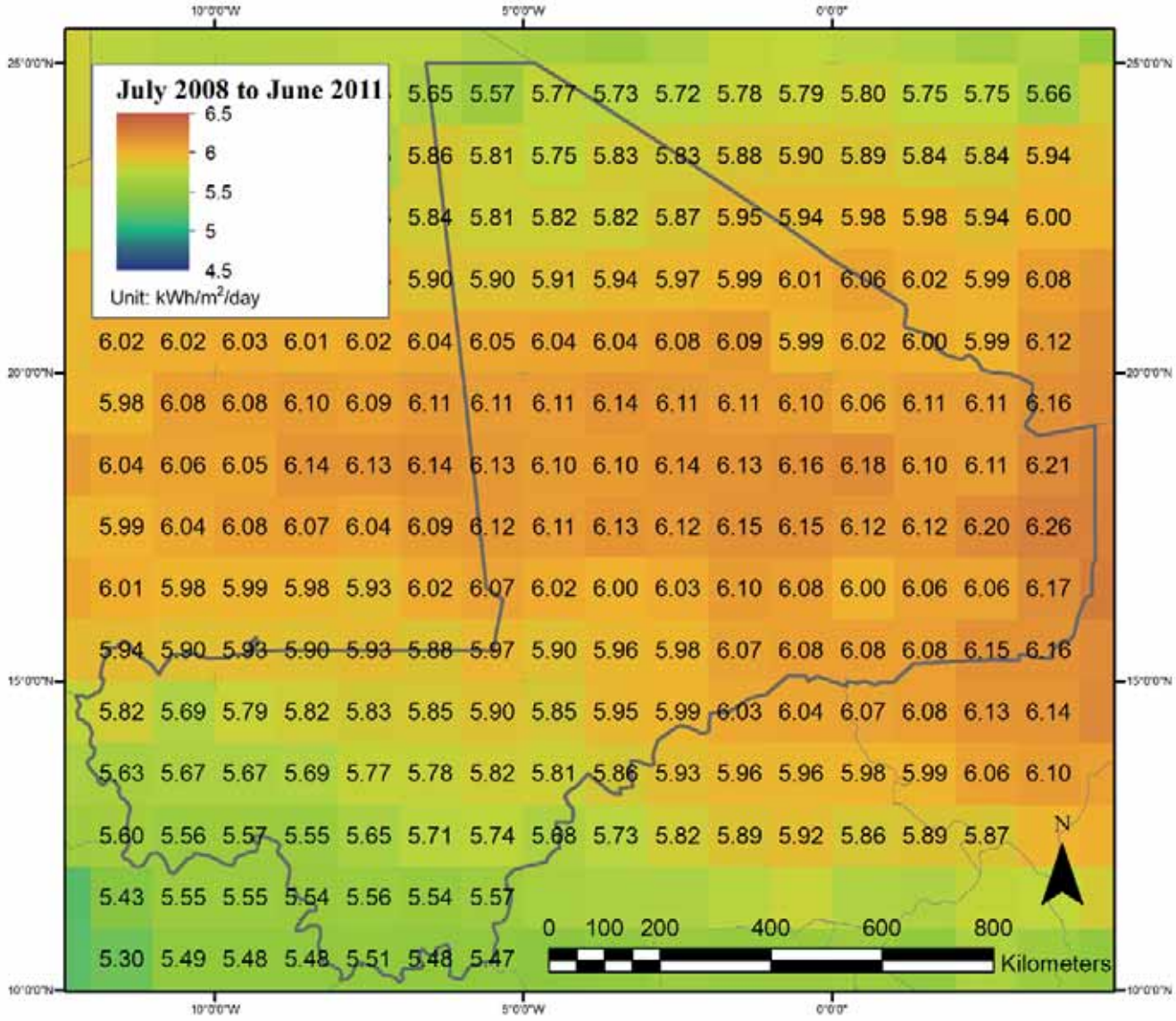

Figure 4.6: Average daily solar radiation for the period between July 2008 and June 2011. Similar maps for the three years are included in appendix D.

The figures above show that there are substantial variation north-south in Mali, due to the seasonal differences in cloud cover and position of the sun. We extracted the time-series of daily radiation estimates for three sites representing the northern, central and southern part of the country (see Figure 4.1 for locations). The northern location is located almost on the Tropic of Cancer where the sun is at zenith at the summer solstice, and we would therefore expect the largest amplitude in the solar radiation time-series for this position as it experiences the largest variation in solar zenith angle. In addition to the differences in sun-earth geometry for the three locations, the cloud cover and atmospheric aerosol content

also induce large temporal variation in solar radiation. The monsoon season starts in May-July in the south, slowly progressing northwards. The differences in cloud cover and timing of the cloud cover (together with the temporal changes in solar position) also causes the time-series for the three points to be out of phase. The southern area sees the largest values of solar radiation in April where the sun is almost at zenith and before the monsoon sets in. For the central and northern areas, the peak appears later in May or July.

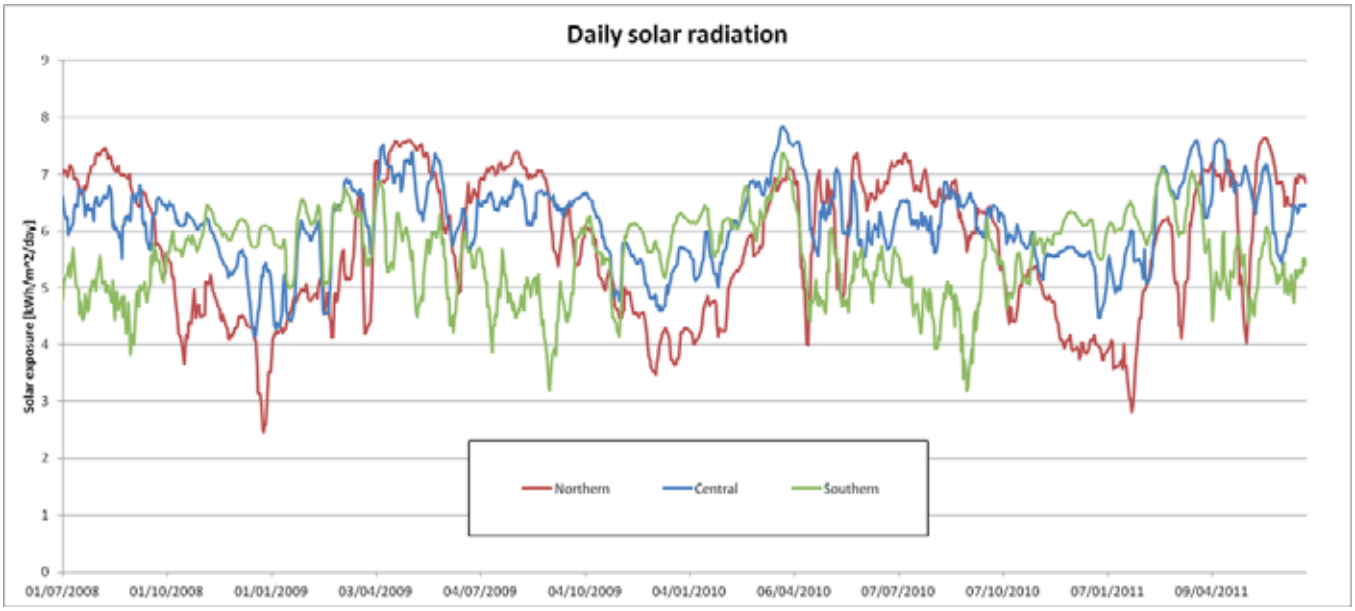

Figure 4.7: Time series of the three areas shown in Figure 4.1 as representing the north-south differences in solar radiation in Mali. Note that the time series have been smoothed with by showing a 9-day moving average.

It is also clear from Figure 4.7, that there is substantial inter-annual variation, due to the differences in the weather and cloudiness from year to year. In Figures 4.8-4.10 the yearly variation in the solar radiation is shown for the three sites, as well as the average (by month) for the three year study period analyzed here. For comparison, we have also included data from the NASA POWER/SSE database (internet link [2]) which shows the monthly average values for the period between 1983 and 2005. Generally, the match between the MSG DSSF estimates and the NASA-estimates are good, although MSG DSSF shows smaller values during spring and summer for the "central"-location.

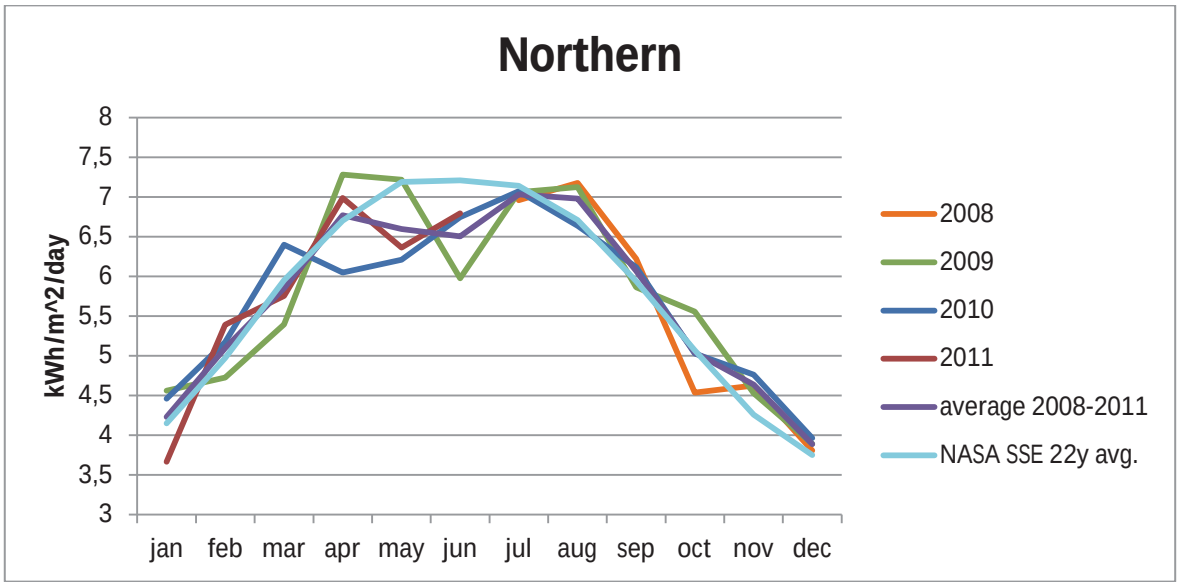

Figure 4.8: Comparison between the 3 years of data from the MSG DSSF product, and the historic NASA SSE (1983-2005) data series for the "North" location (see Figure. 4.1 for location).

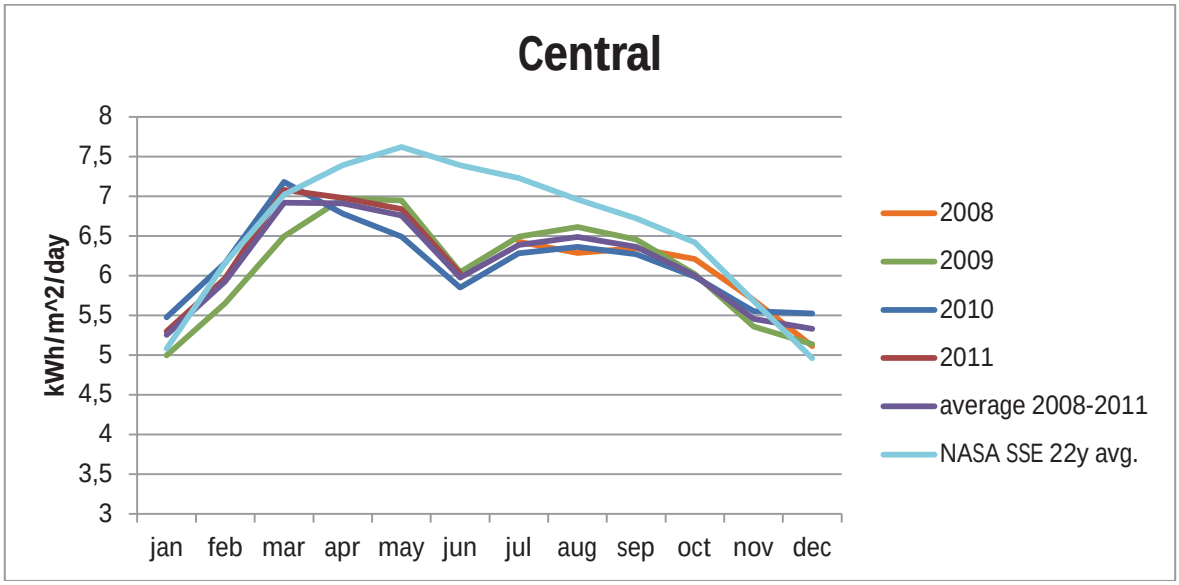

Figure 4.9: Comparison between the 3 years of data from the MSG DSSF product, and the historic NASA SSE (1983-2005) data series for the "Central" location (see Figure 4.1 for location).

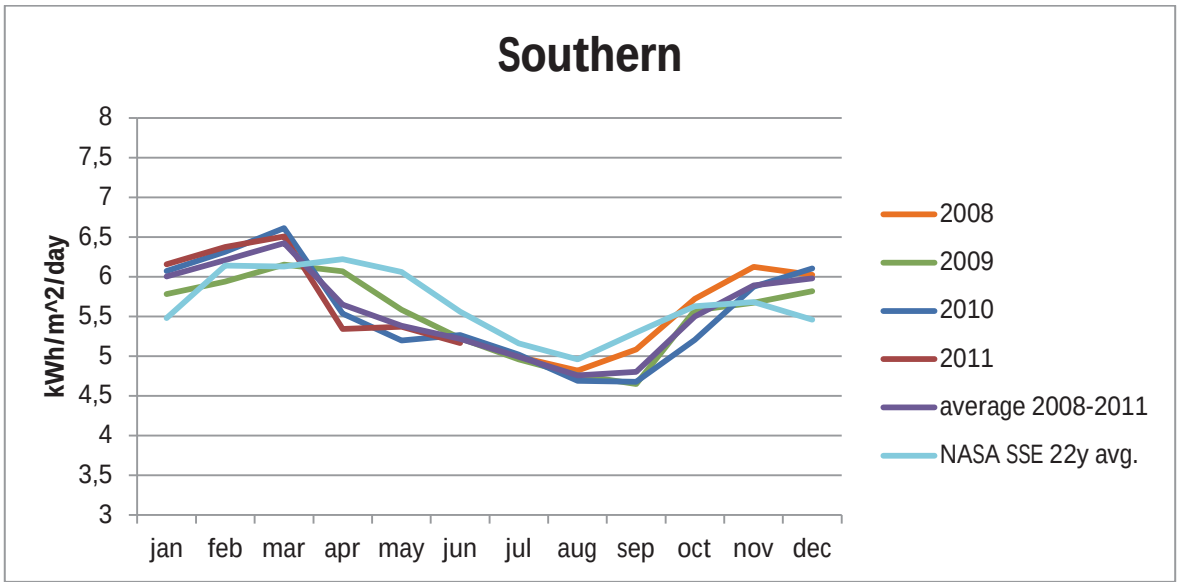

Figure 4.10: Comparison between the 3 years of data from the MSG DSSF product, and the historic NASA SSE (1983-2005) data series for the "South" location (see Figure 4.1 for location).

The average diurnal cycle of solar radiation on a monthly basis is shown in Figure 4.11 for the three sites. Note that the time is given in UTC and the small horizontal shifts in the curves is at least partly caused by the seasonal changes in the timing of local solar noon, while the difference in timing of the maximum values between the three sites can also be related to their absolute positions.

Table 4.1: Comparison between the average of 3 years of data from the MSG DSSF product, and the historic NASA SSE (1983-2005) data series for the three locations (see Figure 4.1 for location)

	Jan	Feb	Mar	Apr	May	Jun	Jul	Aug	Sep	Oct	Nov	Dec
Northern												
Average 2008-11	4.23	5.10	5.85	6.77	6.60	6.50	7.03	6.98	6.07	5.04	4.64	3.89
Nasa SSE	5.08	6.16	7.02	7.39	7.62	7.39	7.23	6.96	6.72	6.42	5.68	4.96
Central												
Average 2008-11	5.25	6.16	7.02	7.39	7.62	7.39	7.23	6.96	6.72	6.42	5.68	4.96
Nasa SSE	4.15	4.97	5.95	6.70	7.19	7.21	7.14	6.71	5.94	5.07	4.26	3.75
Southern												
Average 2008-11	6.00	6.21	6.42	5.65	5.38	5.22	4.99	4.76	4.80	5.50	5.89	5.98
Nasa SSE	5.48	6.14	6.13	6.22	6.06	5.56	5.16	4.96	5.30	5.63	5.68	5.46

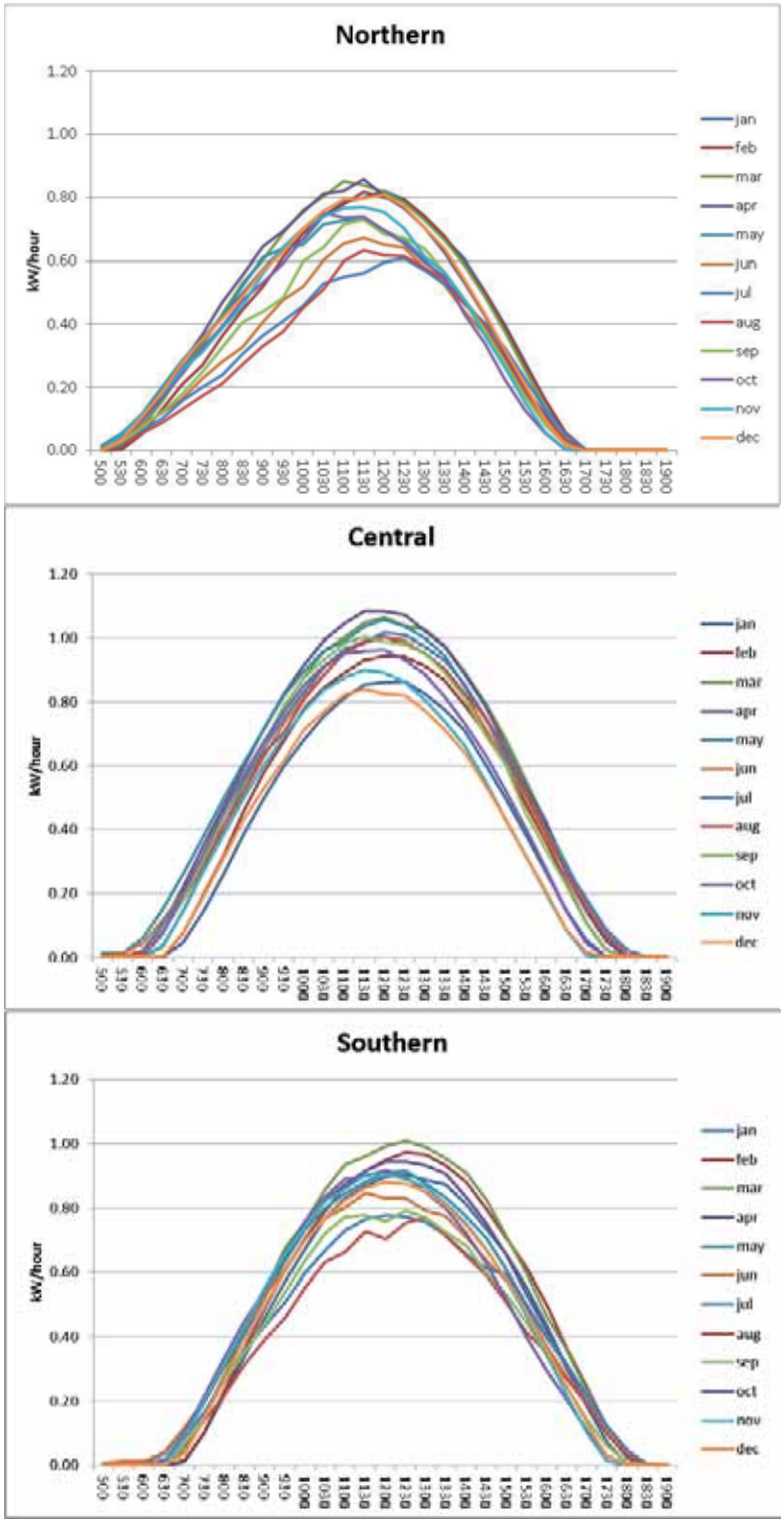

Figure 4.11: Monthly mean diurnal variation in solar radiation (calculated as the mean for each specific time of day for all three years) for the three sites shown in Figure 4.1.

4.6 Summary, discussion and conclusion

In this study we assessed the solar energy resource for Mali for the period between July 2008 and June 2011 using a remote sensing based estimate of the down-welling surface shortwave flux. We found it necessary to calibrate the remote sensing estimates, as we found a tendency for overestimation of the available solar energy at the surface compared to data from five field stations in Mali. The remote sensing estimates were adjusted on a month-by-month basis to account for seasonal differences between the remote sensing estimates and in situ data. Calibration was found to improve the coefficient of determination as well as decreasing the mean error both for the calibration and validation data. Validation using in situ data from two independent stations showed slight improvements in performance after calibration with r^2-values around 0.85 for comparisons between in situ and remote sensing estimates on days with complete data. Note that all calibration and validation was done at the daily scale, while the output of the study is monthly and yearly maps of solar radiation, justifying the approach of optimizing the calibration to avoid systematic biases instead of optimizing to get the best quality daily images.

Gap-filling was carried out to ensure a complete data-series, with no missing values. This was done by gap-filling at several different temporal scales to minimize the potential errors and ensuring a consistent dataset. Again, the approach applied was designed to produce optimal results on the monthly and yearly scale, at the expense of detail at the daily or 30-min temporal scale.

Compared to the results presented in the "Renewable energy resources in Mali – preliminary mapping"-report that showed a tendency for underestimation compared to data from the NASA PPOWER/SSE database, the presented results show a very good agreement with the in situ data (after calibration) with no significant bias. Unfortunately, the NASA-database only contains data up until 2005, so a similar comparison could not be done for the time period analyzed in this study, although the agreement with the historic NASA data (as in figures 4.8-4.10) is still useful as reference.

5 References

BAD, 2010 : Stratégie de développement de la maîtrise de l'énergie au Mali. Groupe de la Banque Africaine de Développement (BAD)

MMEE, 2007 : Stratégie Nationale pour le développement des Energies Renouvelables. Bamako: Ministère des Mines, de l'Energie et de l'Eau (MMEE)

Chapter 2 and 3, Wind Resources

Adrian, G, 1994: Zur Dynamik des Windfeldes über orographisch gegliedertem Gelände, Ber Deutschen Wettedienstes 188, Offenbach am Main 1994, 142 pp.

Adrian, G., F. Fiedler, 1991: Simulation of unstationary wind and temperature fields over complex terrain and comparison with observations. *Beitr. Phys. Atmosph*., 64:27-48
Frank, H. P., L. Landberg, 1997: Modelling the wind climate of Ireland. *Boundary-Layer Meteorology*, 85:359-378

Badger, J, X. G. Larsén, A. N. Hahmann, N. G. Mortensen, J. C. Hansen, Rong, Zhu; Zhenbin, Yang; Chunhong, Yuan. Methods to assess uncertainty of wind resource estimates determined by mesoscale modelling. EWEA Annual Event 2011. Brussels (BE), 14-17 Mar, 2011. In proceedings 5 pages p.

Frank, H. P., O. Rathmann, N. G. Mortensen, L. Landberg, 2001: The Numerical Wind Atlas – the KAMM/WAsP Method, Risoe National Laboratory, Roskilde, Denmark. ISBN 87-550-2850-0, Risø-R-1252(EN).

Frank, H. P., L. Landberg, 1997. Modelling the wind climate of Ireland. Boundary-Layer Meteorology, 85:359-378

Frey-Buness, F., D. Heimann, R. Sausen, 1995. A statistical-dynamical downscaling procedure for global climate simulations. *Theor. Appl. Climatol*., 50:117-131

Kalnay E, Kanamitsou M, Kistler R, Collins W, Deaven D, Gandin L, Irebell M, Saha S, White G, Woollen J, Zhu Y, Leetmaa A, Reynolds R, Chelliah M, Ebisuzaki W, Huggins W, Janowiak J, Mo KC, Ropelewski C, Wang J, Jenne R, Joseph D, 1996. The NCEP/NCAR 40-year reanalysis project. *Bulletin of the American Meteorological Society* **77**: 437-471

Klemp, J.B., D.R. Durran, 1983. An upper boundary condition permitting internal gravity wave radiation in numerical mesoscale models. Mon. Wea. Rev. 1983, 111, 430-444.

Mortensen, N.G., J.C. Hansen, J. Badger, B.H. Jørgensen, C.B. Hasager, L. Georgy Youssef, U. Said Said, A. Abd El-Salam Moussa, M. Akmal Mahmoud, A. El Sayed Yousef, A. Mahmoud Awad, M. Abd-El Raheem Ahmed, M. A.M. Sayed, M. Hussein Korany, M. Abd-El Baky Tarad, 2005. Wind Atlas for Egypt, Measurements and Modelling 1991-2005. New and Renewable Energy Authority, Egyptian Meteorological Authority and Risø National Laboratory. ISBN 87-550-3493-4. 258 pp.

Mortensen, N.G., D.N. Heathfield, L. Myllerup, L. Landberg and O. Rathmann 2007. Wind Atlas Analysis and Application Program: WAsP 9 Help Facility. Risø National Laboratory, Technical University of Denmark, Roskilde, Denmark. 353 topics. ISBN 978-87-550-3607-9.

Kamissoko, 2008. Rapport de Mission: Relatif à l'installation de quatre (4) équipements de mesure dans le cadre du Projet d'Etudes du Gisement Eolien de Tombouctou (PEGET), CNESOLER, Mali

Kamissoko, 2009a. Rapport de Mission: Relatif à l'acheminement et l'installation de deux (2) équipements de mesure dans le cadre du Projet d'Etudes du Gisement Eolien de Tombouctou (PEGET), CNESOLER, Mali

Kamissoko, 2009b. Rapport des activités du projet d'études du gisement éolien de Tombouctou. CNESOLER, Mali

Kamissoko, 2010. Rapport de Mission : Relatif à l'implantation de quatre (04) mâts de mesure du vent et du rayonnement solaire, CNESOLER, Mali

Troen, I., E. L. Petersen, 1989. European Wind Atlas. Risø National Laboratory for the Commission of the European Communities, Roskilde, Denmark, ISBN 87-550-1482-8.

Internet links

[1] ftp://e0srp01u.ecs.nasa.gov

[2] http://edcsns17.cr.usgs.gov/glcc/

[3] http://www.cdc.noaa.gov/cdc/reanalysis/

Chapter 4, Solar resources

EUMETSAT, 2011. Product User Manual Down-welling Surface Shortwave Flux (DSSF), Issue 2.6v2.

EUMETSAT, 2011. Validation Report. Down-welling Surface Shortwave Flux (DSSF), Issue I/2011 v4

Schmetz, J., Pili, P., Tjemkes, S., Just, D., Kerkmann, J., Rota, S., Ratier, A., 2002. An Introduction to Meteosat Second Generation (MSG). Bulletin of the American Meteorological Society 83, 977-992.

Internet links

[1] http://landsaf.meteo.pt/

[2] http://eosweb.larc.nasa.gov/sse/

APPENDIX A: Overview of the timing of the measurements

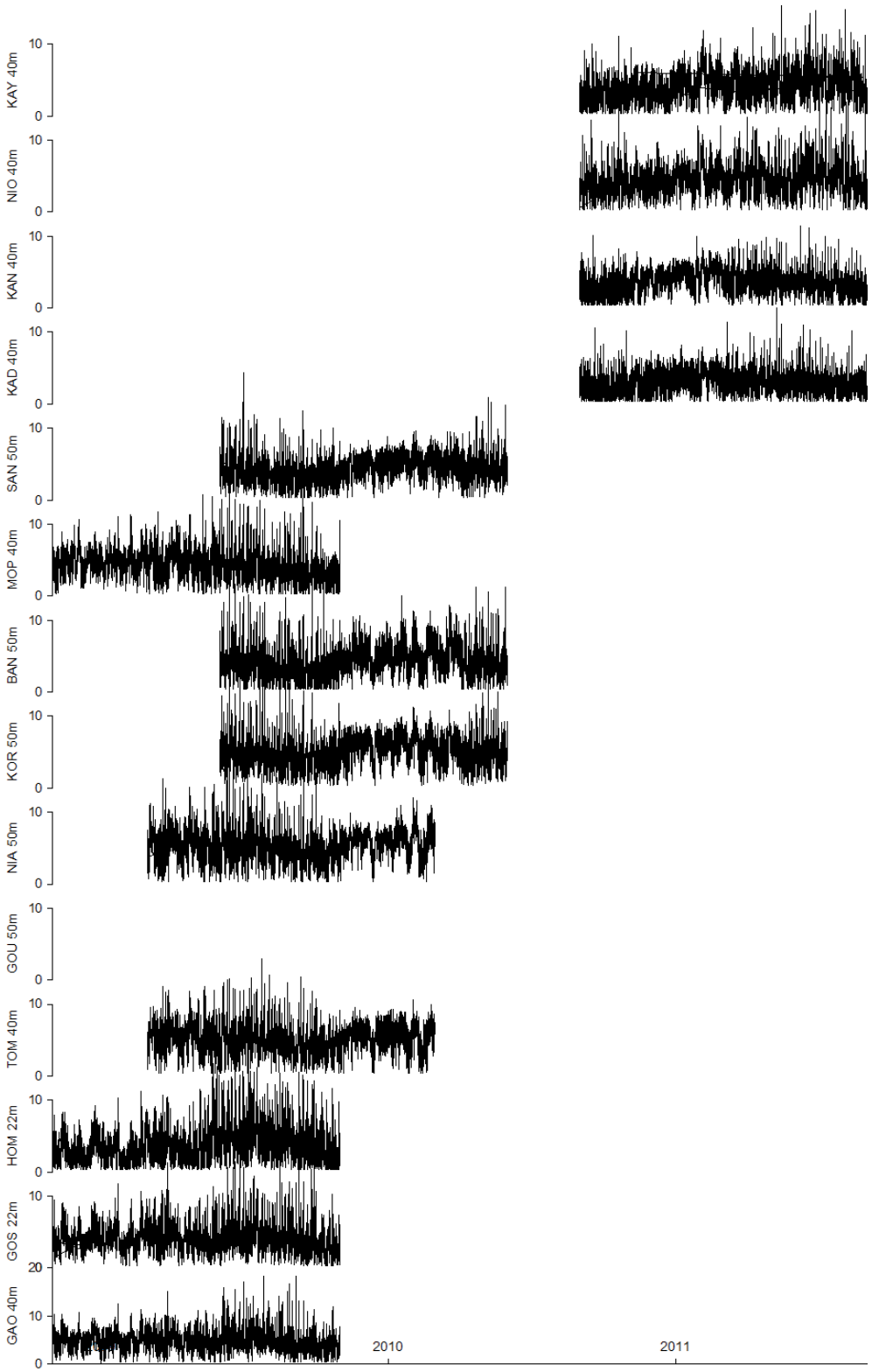

Figure 1: Overview of the timing of the measurements. (Data source: CNESOLER, 2012)

APPENDIX B: Measured wind speed and solar radiation

Four graphs of the wind statistics have been prepared based on one year of data from each station:

- The frequency distributions of the wind directions (the wind rose), divided into 12 wind direction sectors.
- The frequency distributions of the wind speeds (the histogram), divided into 1 m/s wind speed bins, with indication of the parameters for the fitted Weibull distribution function (A and k), the average wind speed (U) and the power density (P) for standard air density (1.225 kg/m^3).
- The variations over the year of the monthly average wind speeds (blue), turbulence intensities (blue dashed) and power densities (red) (@ 1 kg/m^3 air density).
- The monthly average variations over the day of the hourly average wind speeds (blue) and power densities (red) for two selected months – the months with the highest (solid) and lowest (dashed) average power density.

In addition, two plots of the solar radiation statistics have been prepared for the stations with solar radiation data:

- The variations over the year of the monthly average and maximum solar radiations and monthly average air temperatures.
- The monthly average variations over the day of the hourly average solar radiations and air temperatures for January and July.

The stations are organised by their locations from east towards west:

- Kayes
- Nioro
- Kangaba
- Kadiolo
- San
- Mopti
- Bandiagara
- Koro
- Niafunke
- Goundam
- Tombouctou
- Hombori
- Gossi
- Gao

Kayes

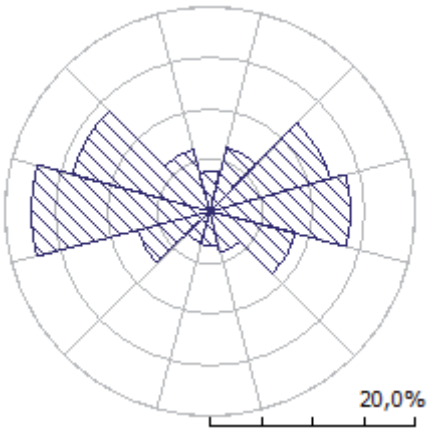
20,0%

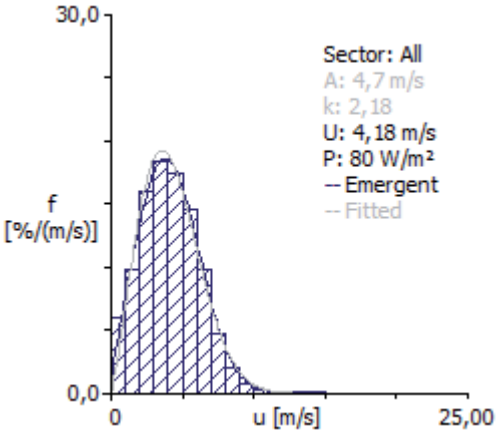
30,0
f
[%/(m/s)]
0,0
0
u [m/s]
25,00
Sector: All
A: 4,7 m/s
k: 2,18
U: 4,18 m/s
P: 80 W/m²
Emergent
Fitted

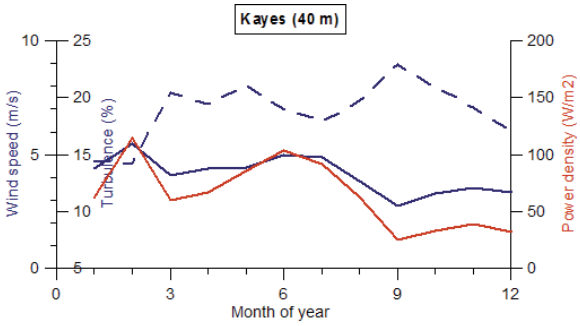
Kayes (40 m)
Wind speed (m/s)
Turbulence (%)
Power density (W/m2)
Month of year

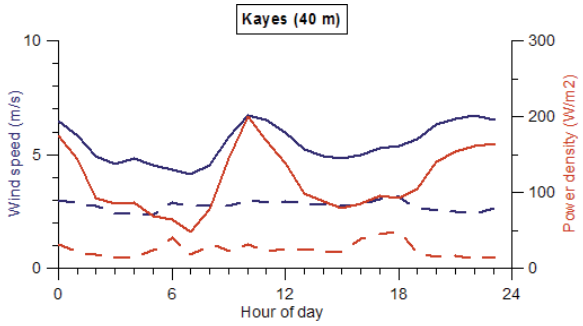
Kayes (40 m)
Wind speed (m/s)
Power density (W/m2)
Hour of day

Nioro

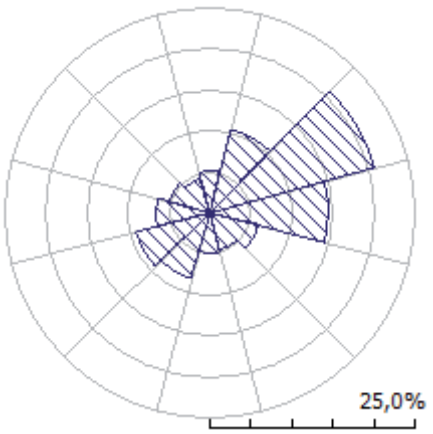
25,0%

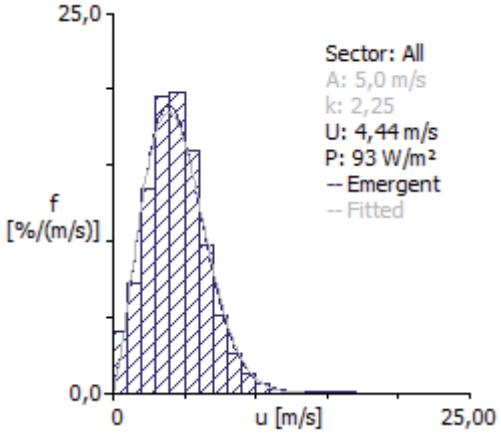
25,0
f
[%/(m/s)]
0,0
0
u [m/s]
25,00
Sector: All
A: 5,0 m/s
k: 2,25
U: 4,44 m/s
P: 93 W/m²
Emergent
Fitted

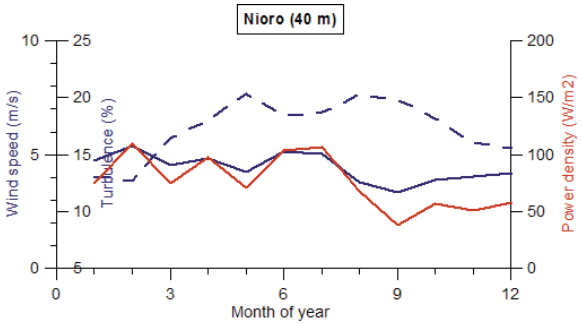
Nioro (40 m)
Wind speed (m/s)
Turbulence (%)
Power density (W/m2)
Month of year

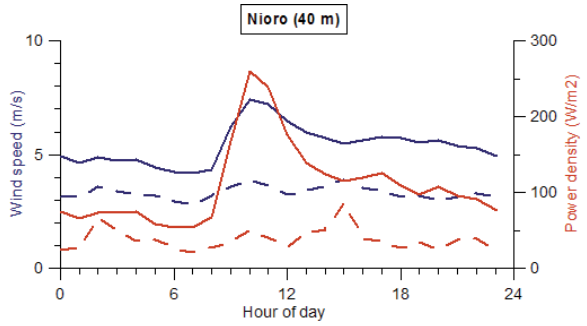
Nioro (40 m)
Wind speed (m/s)
Power density (W/m2)
Hour of day

Kangaba

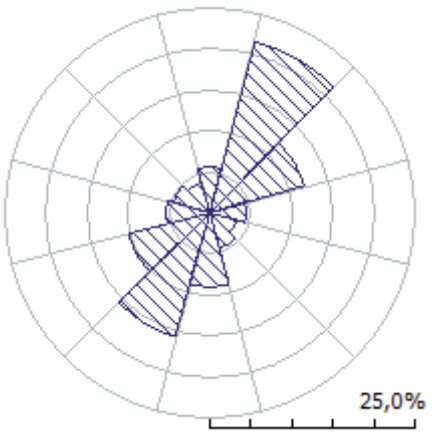
25,0%

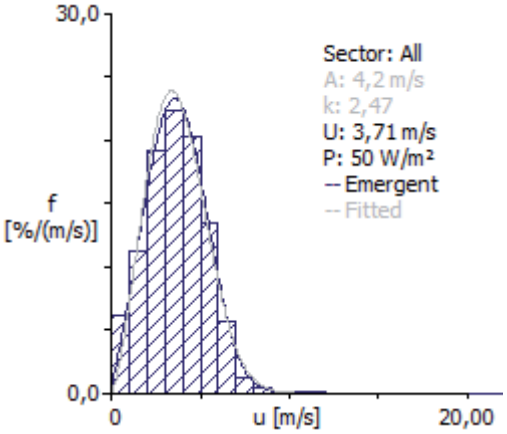
30,0
f
[%/(m/s)]
0,0
0
u [m/s]
20,00
Sector: All
A: 4,2 m/s
k: 2,47
U: 3,71 m/s
P: 50 W/m²
Emergent
Fitted

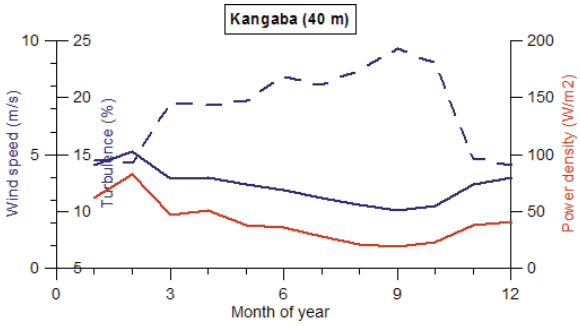
Kangaba (40 m)
Wind speed (m/s)
Turbulence (%)
Power density (W/m2)
Month of year

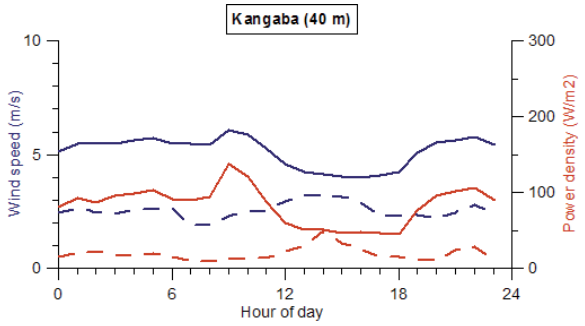
Kangaba (40 m)
Wind speed (m/s)
Power density (W/m2)
Hour of day

Kadiolo

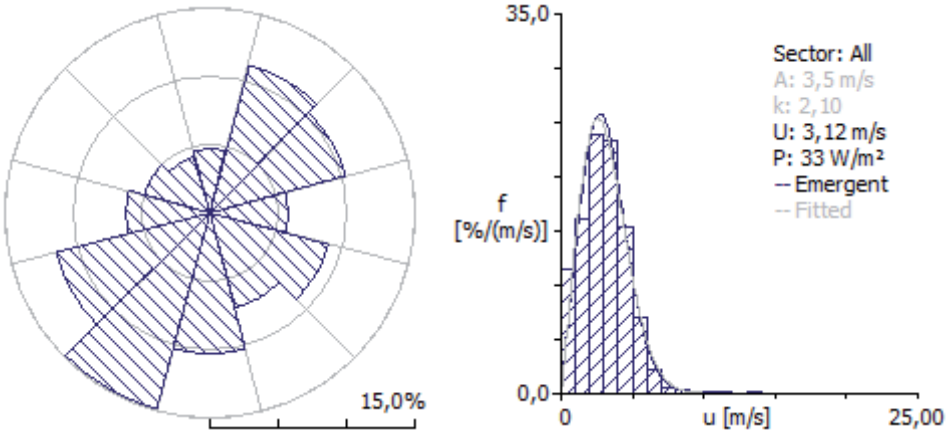
15,0%
35,0
f
[%/(m/s)]
0,0
0
u [m/s]
25,00
Sector: All
A: 3,5 m/s
k: 2,10
U: 3,12 m/s
P: 33 W/m²
Emergent
Fitted

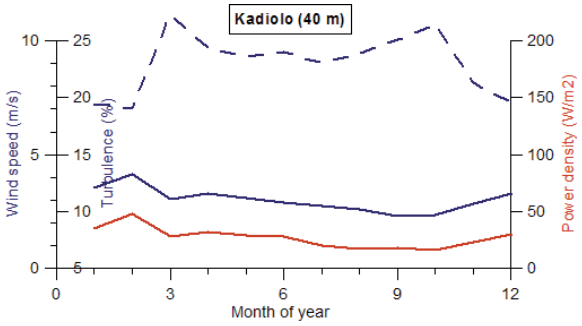
Kadiolo (40 m)
Wind speed (m/s)
Turbulence (%)
Power density (W/m2)
Month of year

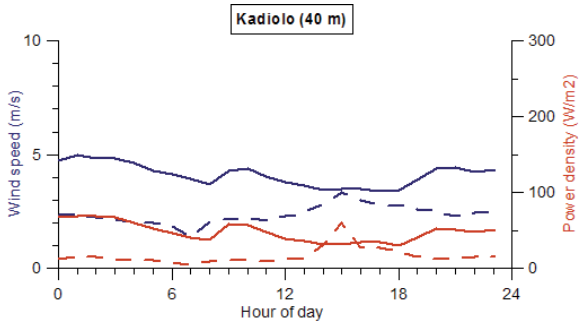
Kadiolo (40 m)
Wind speed (m/s)
Power density (W/m2)
Hour of day

San

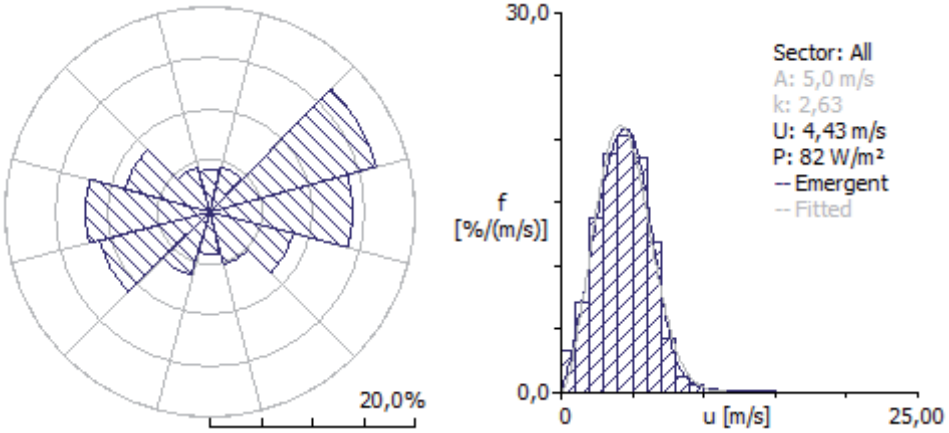
20,0%
30,0
f
[%/(m/s)]
0,0
0
u [m/s]
25,00
Sector: All
A: 5,0 m/s
k: 2,63
U: 4,43 m/s
P: 82 W/m²
Emergent
Fitted

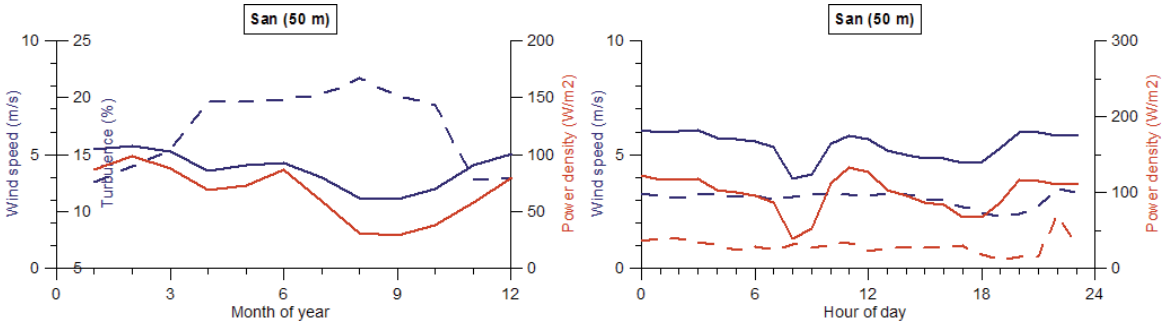
San (50 m)
Wind speed (m/s)
Turbulence (%)
Power density (W/m2)
Month of year
San (50 m)
Wind speed (m/s)
Power density (W/m2)
Hour of day

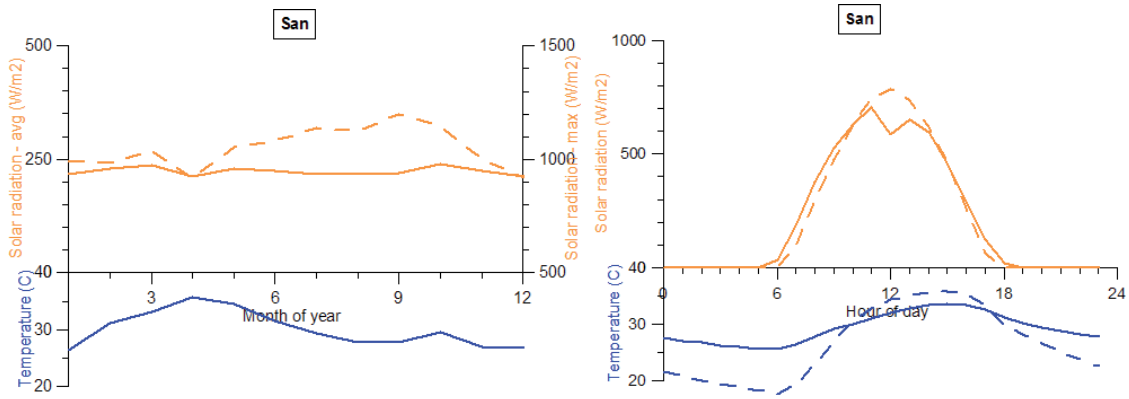
San
Solar radiation - avg (W/m2)
Solar radiation - max (W/m2)
Temperature (C)
Month of year
San
Solar radiation (W/m2)
Temperature (C)
Hour of day

Mopti

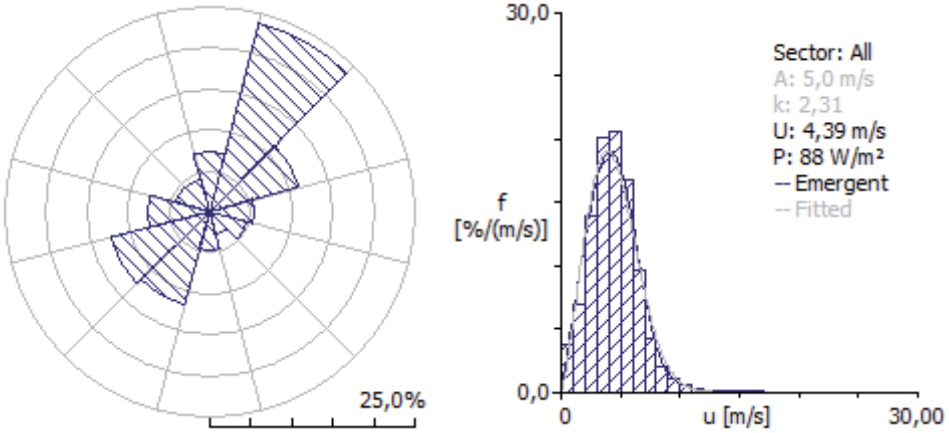
25,0%
30,0
f
[%/(m/s)]
0,0
0
u [m/s]
30,00
Sector: All
A: 5,0 m/s
k: 2,31
U: 4,39 m/s
P: 88 W/m²
Emergent
Fitted

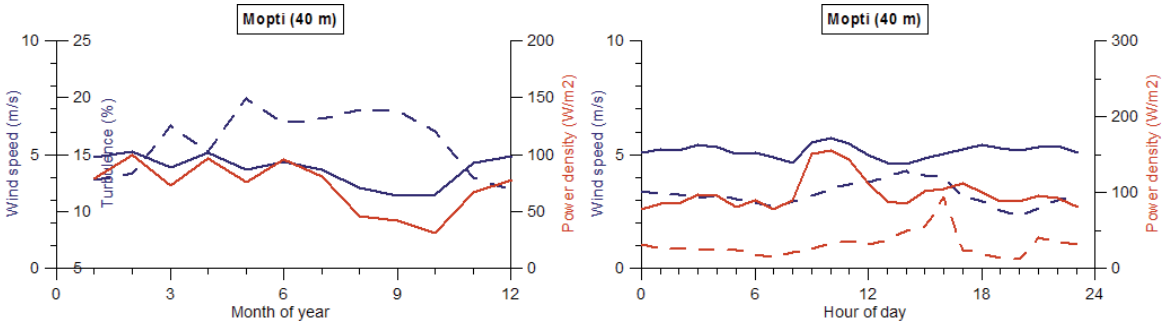
Mopti (40 m)
Wind speed (m/s)
Turbulence (%)
Power density (W/m2)
Month of year
Mopti (40 m)
Wind speed (m/s)
Power density (W/m2)
Hour of day

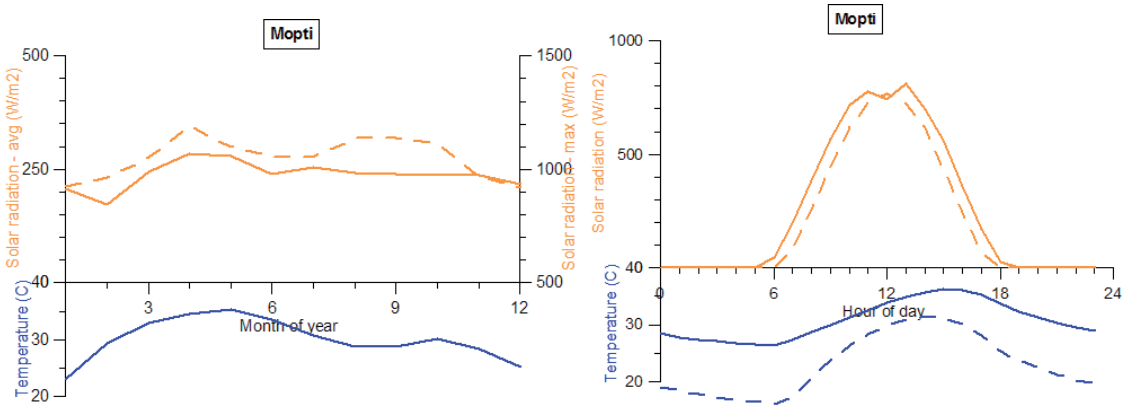
Mopti
Solar radiation - avg (W/m2)
Solar radiation - max (W/m2)
Temperature (C)
Month of year
Mopti
Solar radiation (W/m2)
Temperature (C)
Hour of day

Bandiagara

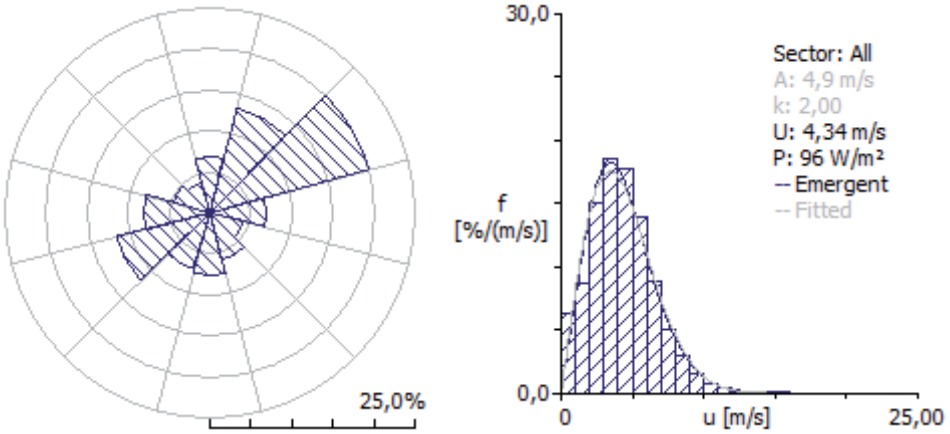
25,0%
30,0
f
[%/(m/s)]
0,0
0
u [m/s]
25,00
Sector: All
A: 4,9 m/s
k: 2,00
U: 4,34 m/s
P: 96 W/m²
Emergent
Fitted

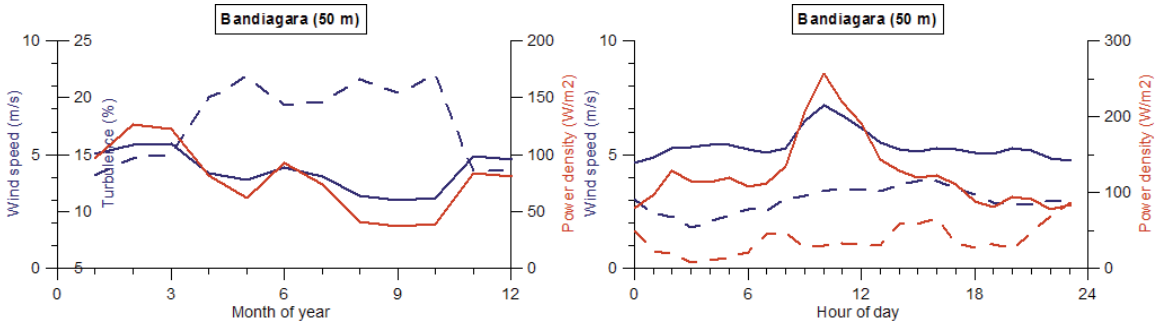
Bandiagara (50 m)
Wind speed (m/s)
Turbulence (%)
Power density (W/m2)
Month of year
Bandiagara (50 m)
Wind speed (m/s)
Power density (W/m2)
Hour of day

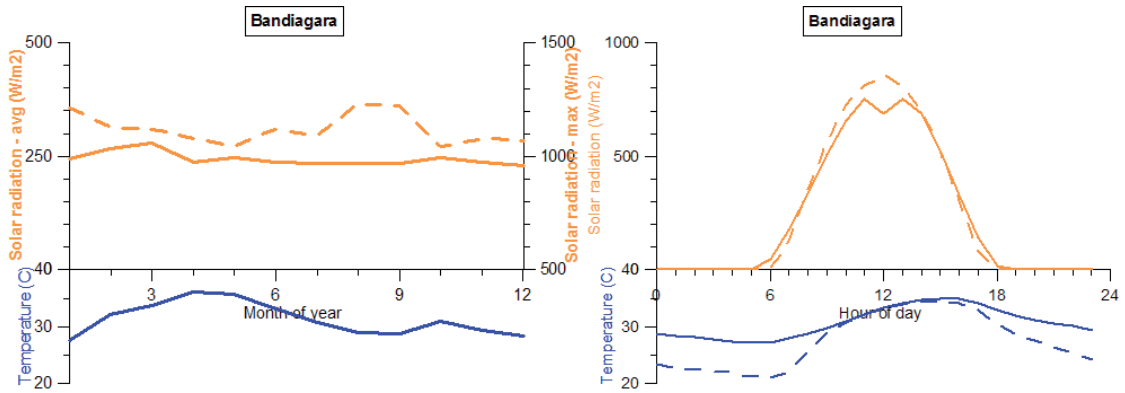
Bandiagara
Solar radiation - avg (W/m2)
Temperature (C)
Month of year
Bandiagara
Solar radiation - max (W/m2)
Solar radiation (W/m2)
Temperature (C)
Hour of day

Koro

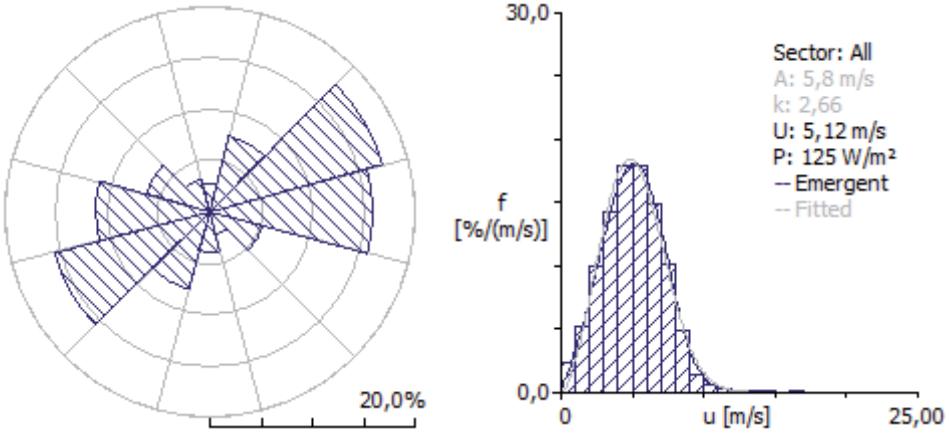
20,0%
30,0
f
[%/(m/s)]
0,0
0
u [m/s]
25,00
Sector: All
A: 5,8 m/s
k: 2,66
U: 5,12 m/s
P: 125 W/m²
Emergent
Fitted

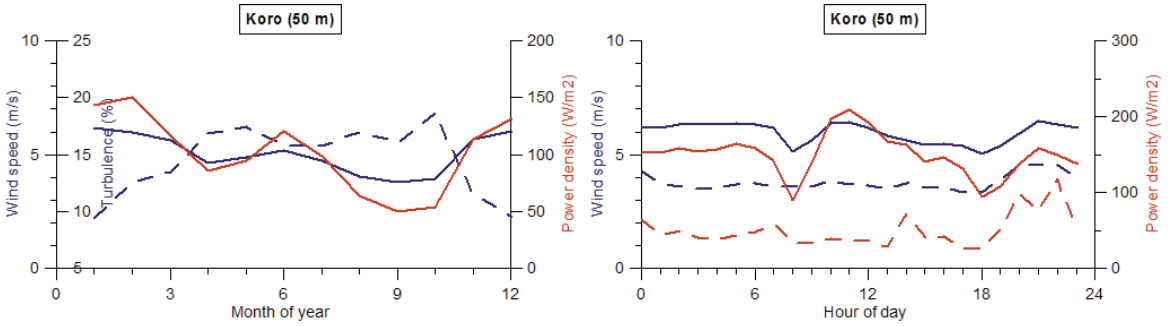
Koro (50 m)
Wind speed (m/s)
Turbulence (%)
Power density (W/m2)
Month of year
Koro (50 m)
Wind speed (m/s)
Power density (W/m2)
Hour of day

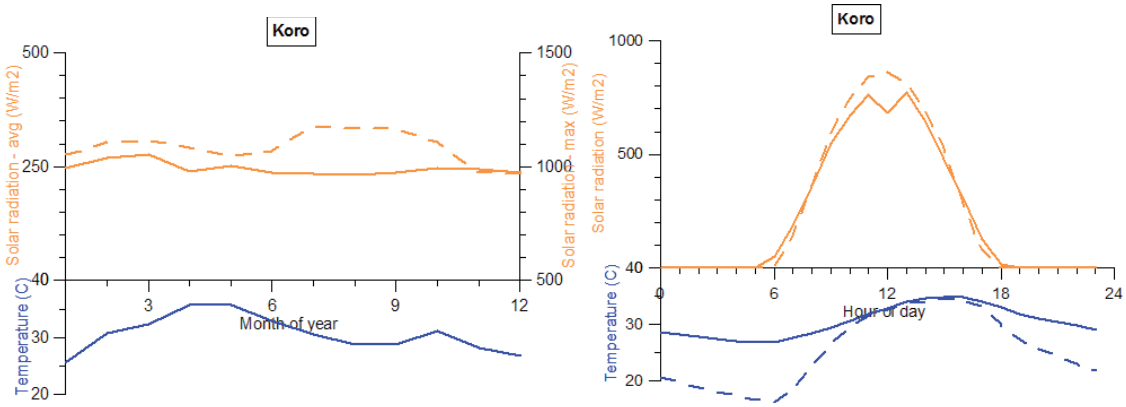
Koro
Solar radiation - avg (W/m2)
Solar radiation - max (W/m2)
Temperature (C)
Month of year
Koro
Solar radiation (W/m2)
Temperature (C)
Hour of day

Niafunke

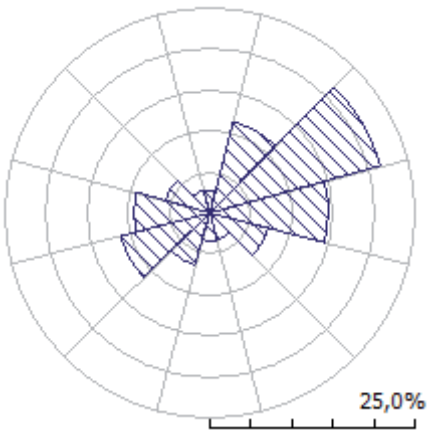
25,0%

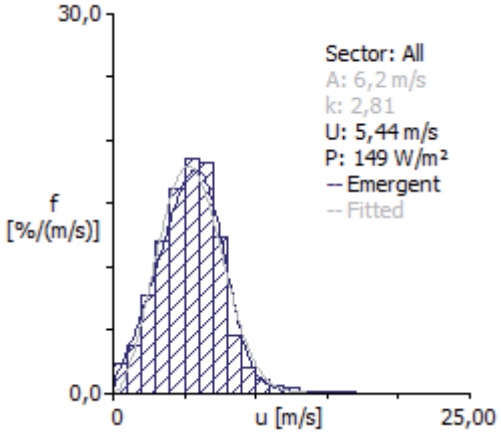
30,0
f
[%/(m/s)]
0,0
0
u [m/s]
25,00
Sector: All
A: 6,2 m/s
k: 2,81
U: 5,44 m/s
P: 149 W/m²
Emergent
Fitted

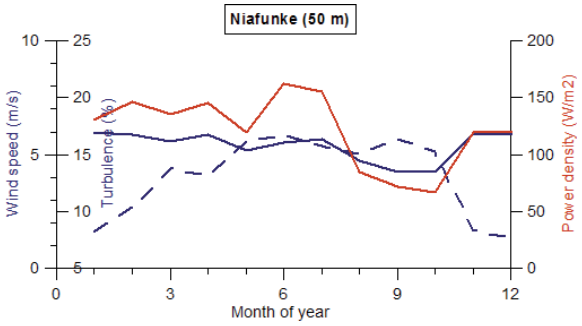
Niafunke (50 m)
Wind speed (m/s)
Turbulence (%)
Power density (W/m2)
Month of year

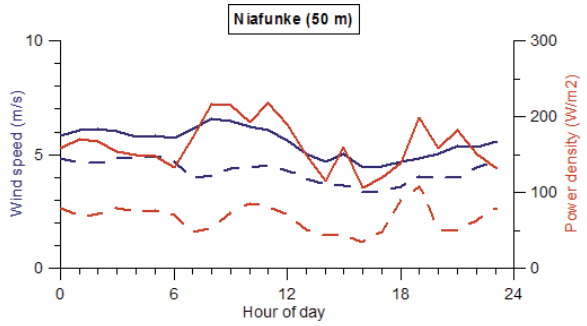
Niafunke (50 m)
Wind speed (m/s)
Power density (W/m2)
Hour of day

Goundam

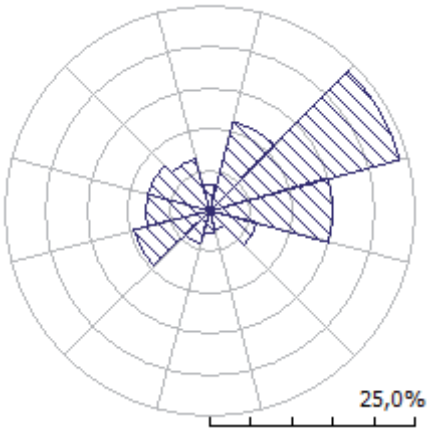
25,0%

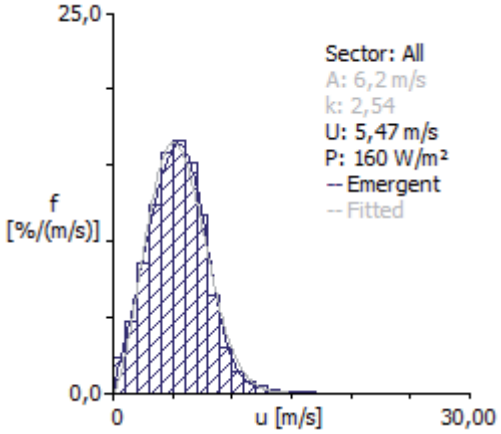
25,0
f
[%/(m/s)]
0,0
0
u [m/s]
30,00
Sector: All
A: 6,2 m/s
k: 2,54
U: 5,47 m/s
P: 160 W/m²
Emergent
Fitted

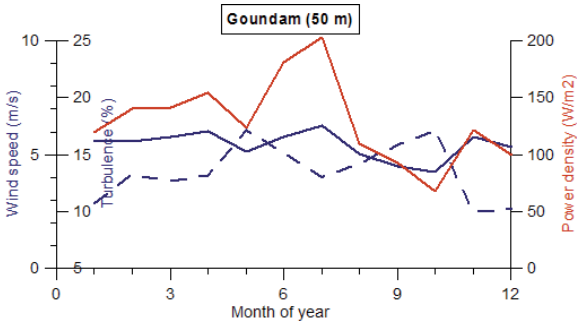
Goundam (50 m)
Wind speed (m/s)
Turbulence (%)
Power density (W/m2)
Month of year

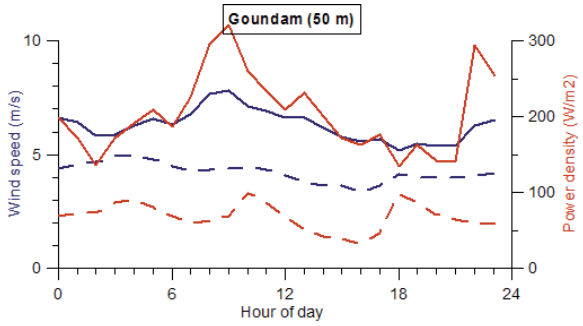
Goundam (50 m)
Wind speed (m/s)
Power density (W/m2)
Hour of day

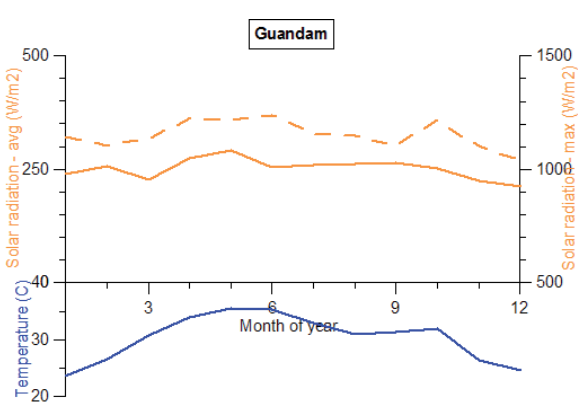
Guandam
Solar radiation - avg (W/m2)
Solar radiation - max (W/m2)
Temperature (C)
Month of year

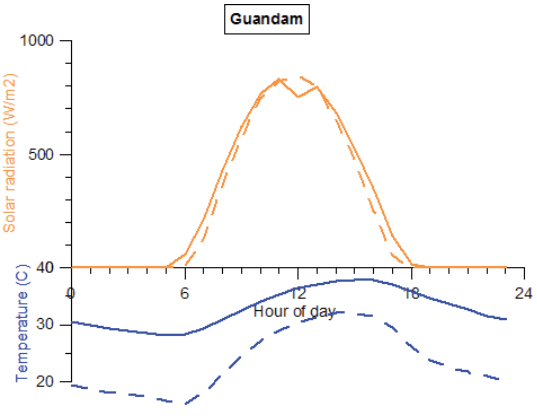
Guandam
Solar radiation (W/m2)
Temperature (C)
Hour of day

Tombouctou

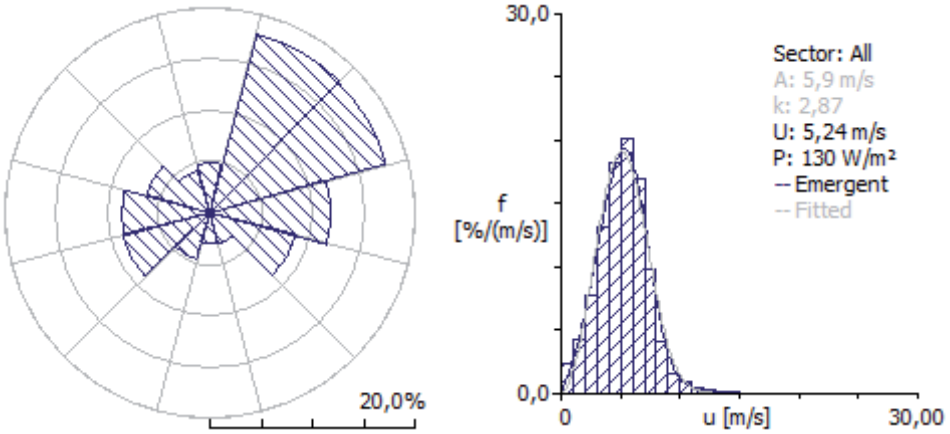
20,0%
30,0
f
[%/(m/s)]
0,0
0
u [m/s]
30,00
Sector: All
A: 5,9 m/s
k: 2,87
U: 5,24 m/s
P: 130 W/m²
Emergent
Fitted

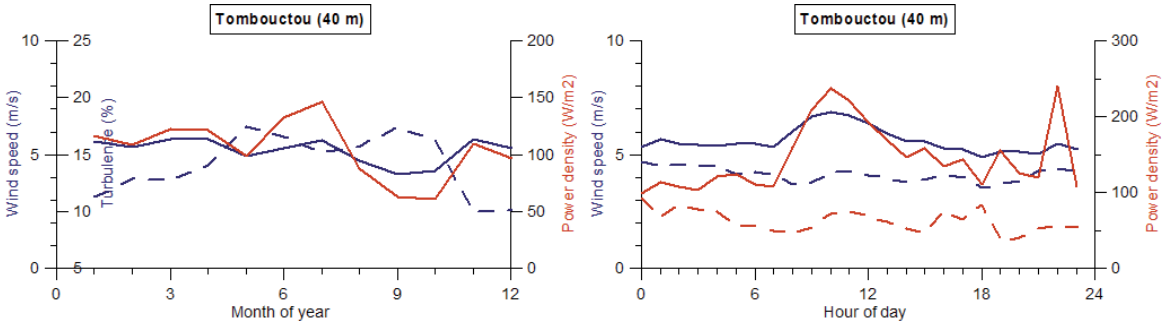
Tombouctou (40 m)
Wind speed (m/s)
Turbulence (%)
Power density (W/m2)
Month of year
Tombouctou (40 m)
Wind speed (m/s)
Power density (W/m2)
Hour of day

Hombori

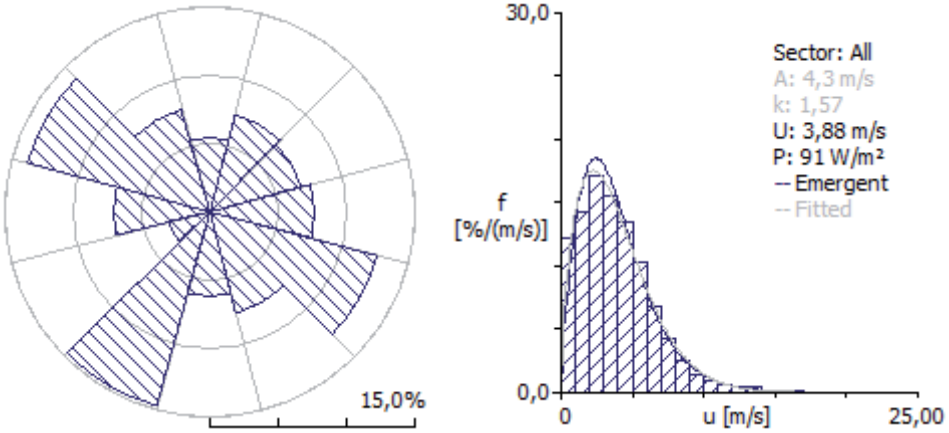
15,0%
30,0
0,0
f
[%/(m/s)]
0
u [m/s]
25,00
Sector: All
A: 4,3 m/s
k: 1,57
U: 3,88 m/s
P: 91 W/m²
Emergent
Fitted

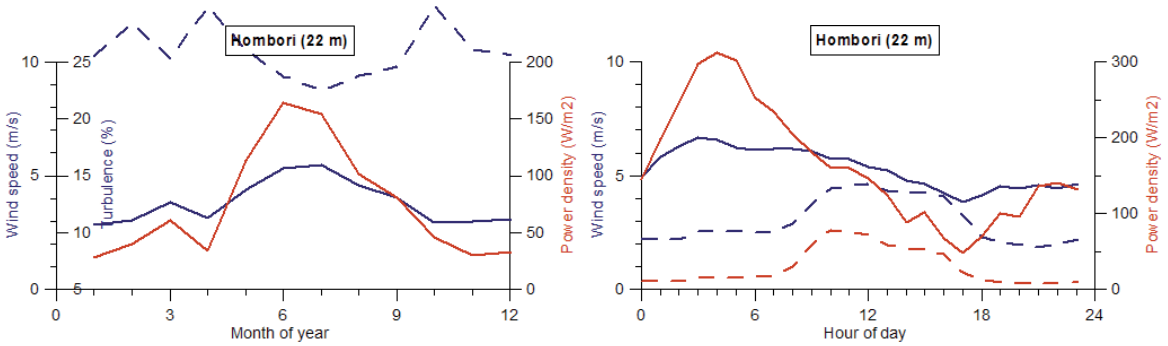
Hombori (22 m)
Wind speed (m/s)
Turbulence (%)
Power density (W/m2)
Month of year
Hombori (22 m)
Wind speed (m/s)
Power density (W/m2)
Hour of day

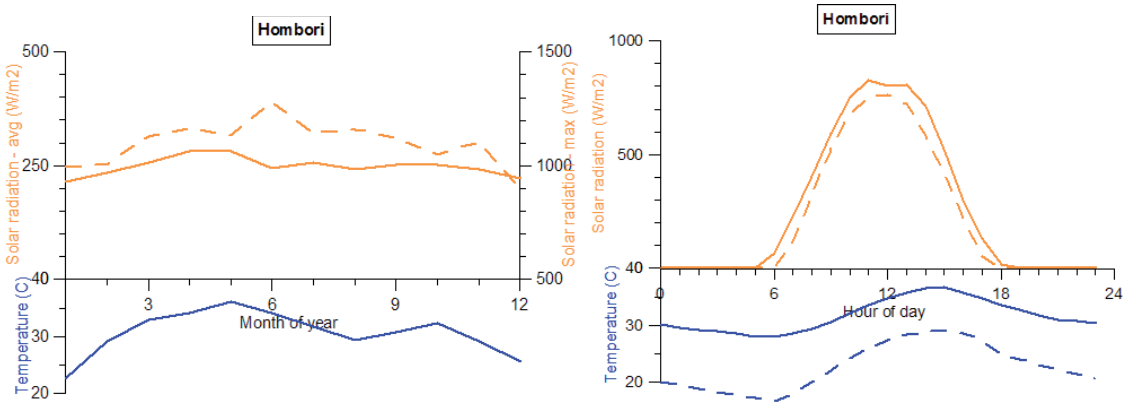
Hombori
Solar radiation - avg (W/m2)
Solar radiation - max (W/m2)
Temperature (C)
Month of year
Hombori
Solar radiation (W/m2)
Temperature (C)
Hour of day

Gossi

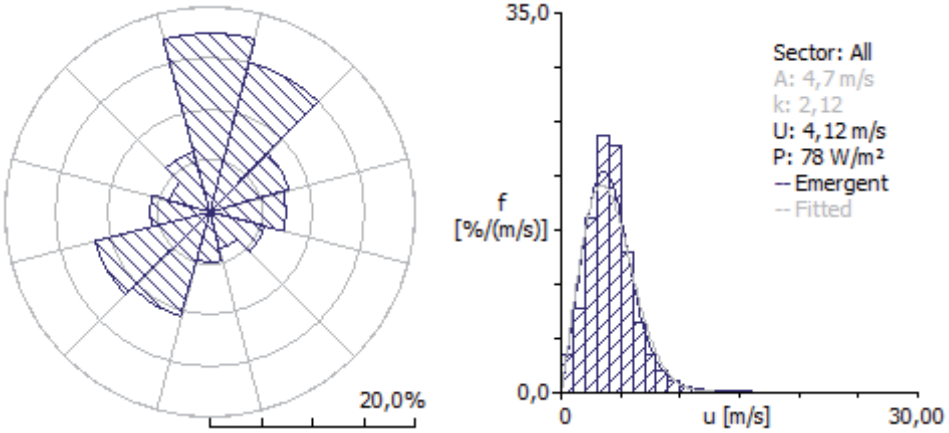
20,0%
35,0
f
[%/(m/s)]
0,0
0
u [m/s]
30,00
Sector: All
A: 4,7 m/s
k: 2,12
U: 4,12 m/s
P: 78 W/m²
Emergent
Fitted

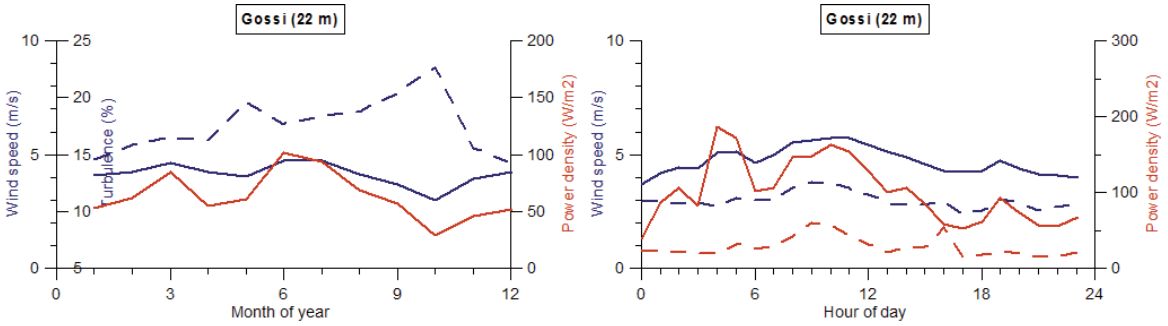
Gossi (22 m)
Wind speed (m/s)
Turbulence (%)
Power density (W/m2)
Month of year
Gossi (22 m)
Wind speed (m/s)
Power density (W/m2)
Hour of day

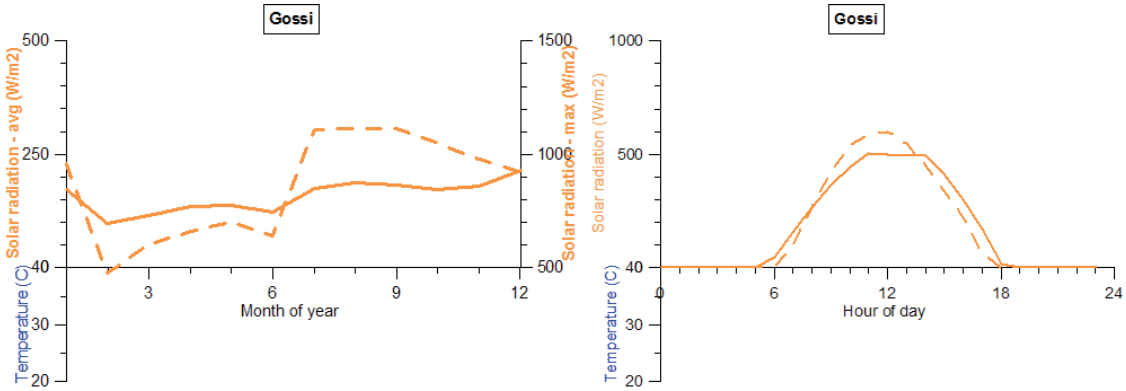
Gossi
Solar radiation - avg (W/m2)
Solar radiation - max (W/m2)
Temperature (C)
Month of year
Gossi
Solar radiation (W/m2)
Temperature (C)
Hour of day

Gao

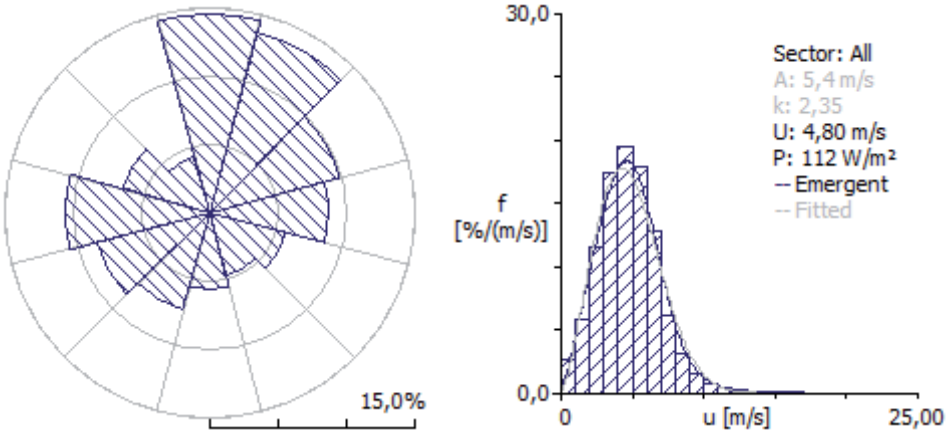
15,0%
30,0
f
[%/(m/s)]
0,0
0
u [m/s]
25,00
Sector: All
A: 5,4 m/s
k: 2,35
U: 4,80 m/s
P: 112 W/m²
Emergent
Fitted

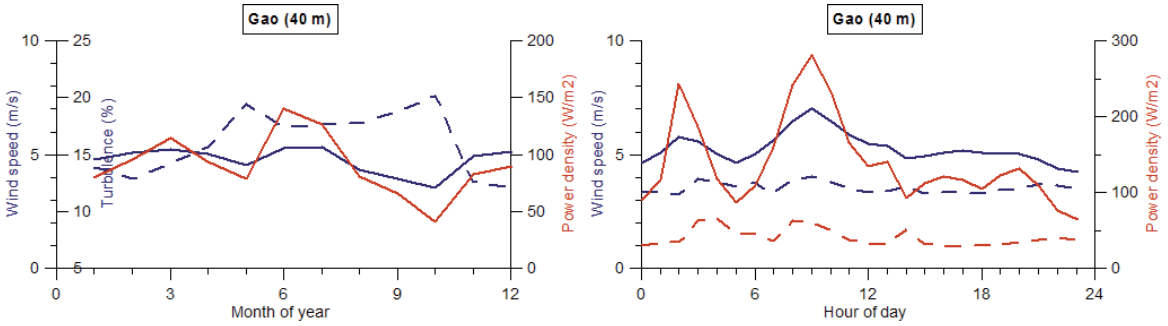
Gao (40 m)
Wind speed (m/s)
Turbulance (%)
Power density (W/m2)
Month of year
Gao (40 m)
Wind speed (m/s)
Power density (W/m2)
Hour of day

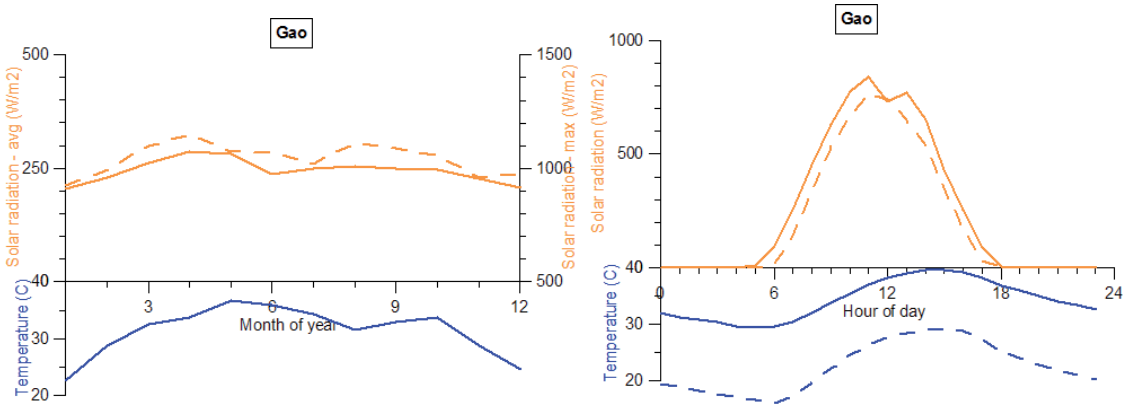
Gao
Solar radiation - avg (W/m2)
Solar radiation - max (W/m2)
Temperature (C)
Month of year
Gao
Solar radiation (W/m2)
Temperature (C)
Hour of day

APPENDIX C: Sensor serial numbers

NRG Systems ® sensor serial numbers are listed below:

Bandiagara: 95271, 95270, 95269, 95266
Gao: 42199, 42197, 42188, 42181
Gossi: 42198,42191, 42190, 42189
Goundam: 77737, 77736, 77735, 77734
Hombori: 42196, 42195, 42194, 42192
Koro: 95279, 95278, 95256, 95252
Niafunke: 77739, 77738, 77731, 77730
San: 95283, 95282, 95280, 95281
Sevare: 42212, 42211, 42193, 42200
Tombouctou: 77733, 77732, 77729, 77728
Kadiolo: 133776, 133777, 95207, 95208
Kangaba: 133774, 133773, 133771, 133770
Kayes: 95201,95202, 95203, 95204
Nioro: 95254, 95255, 95210, 95211

APPENDIX D: Maps of annual and monthly solar radiation

This appendix contains the solar radiation maps on a monthly and yearly scale.

1 Yearly averages (per day) in kWh/m^2/day for the three years of data (July-June)

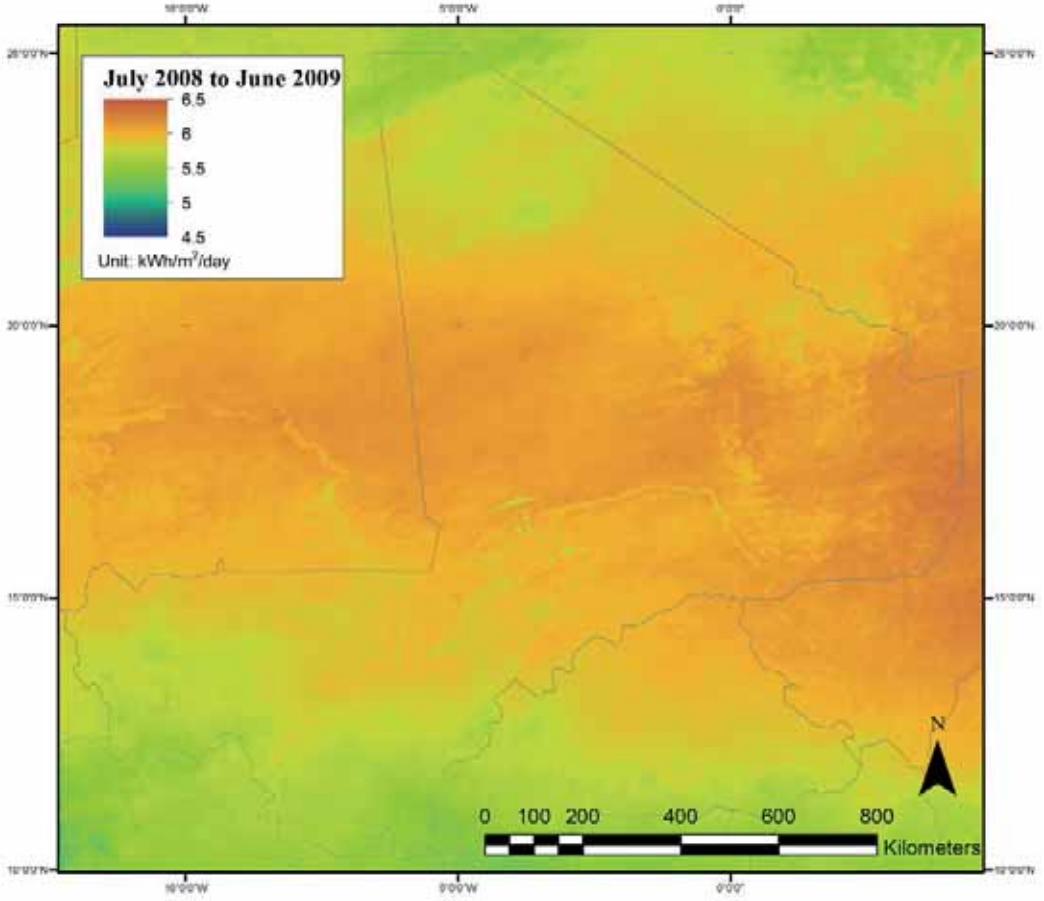
July 2008 to June 2009
6.5
6
5.5
5
4.5
Unit: kWh/m²/day
N
0 100 200 400 600 800
Kilometers

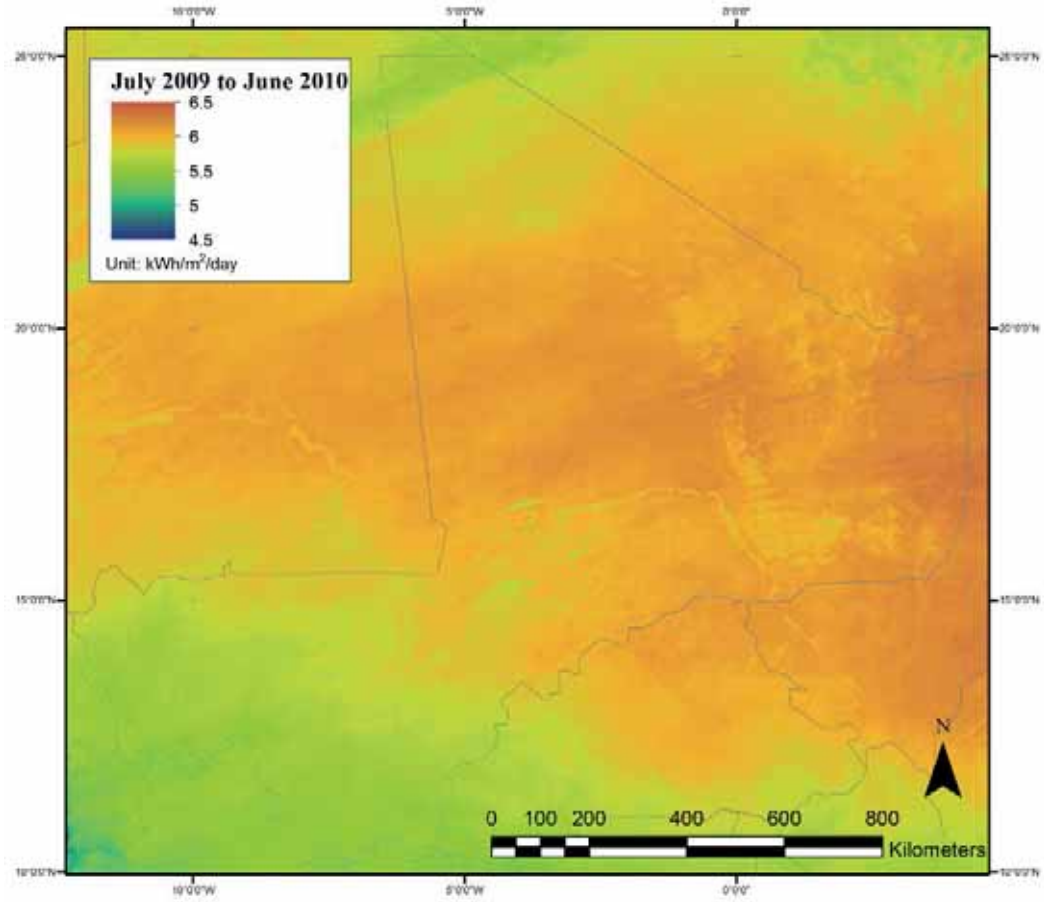
July 2009 to June 2010
6.5
6
5.5
5
4.5
Unit: kWh/m²/day
N
0 100 200 400 600 800
Kilometers

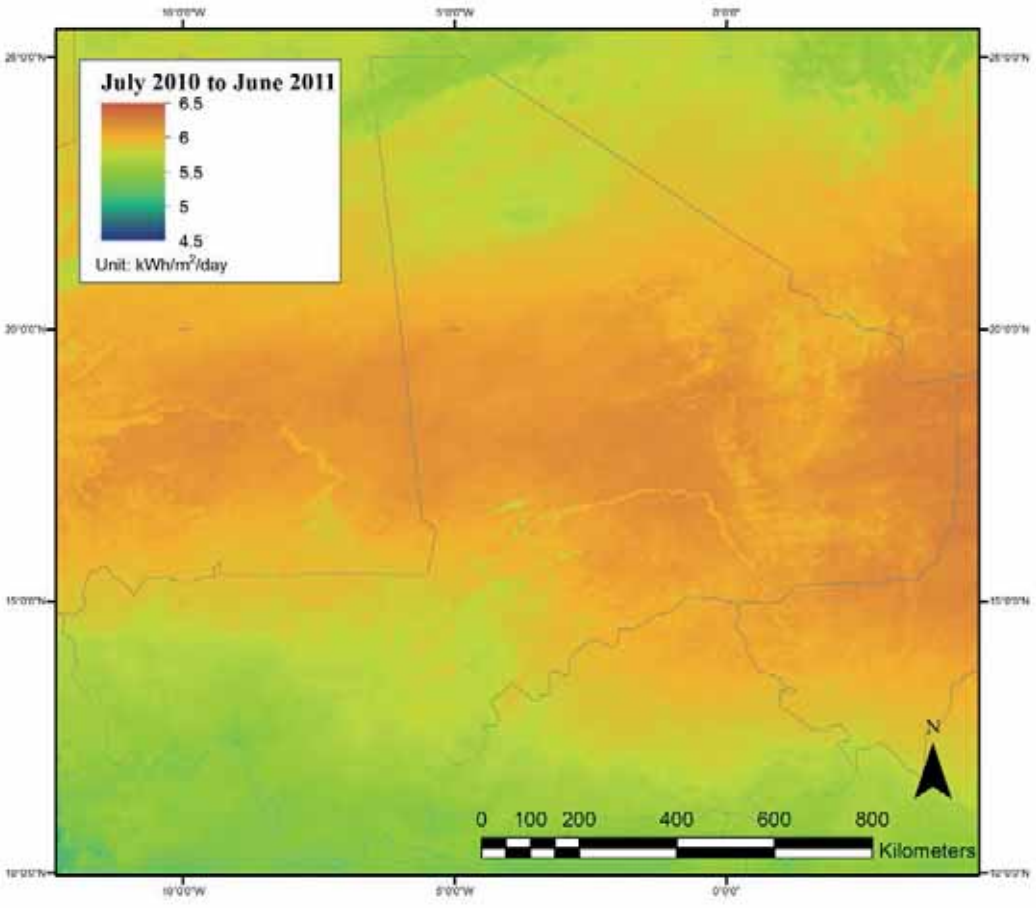
July 2010 to June 2011
6.5
6
5.5
5
4.5
Unit: kWh/m2/day
N
0 100 200 400 600 800
Kilometers

2 Yearly averages (per day) in kWh/m^2/day for the years 2009 and 2010

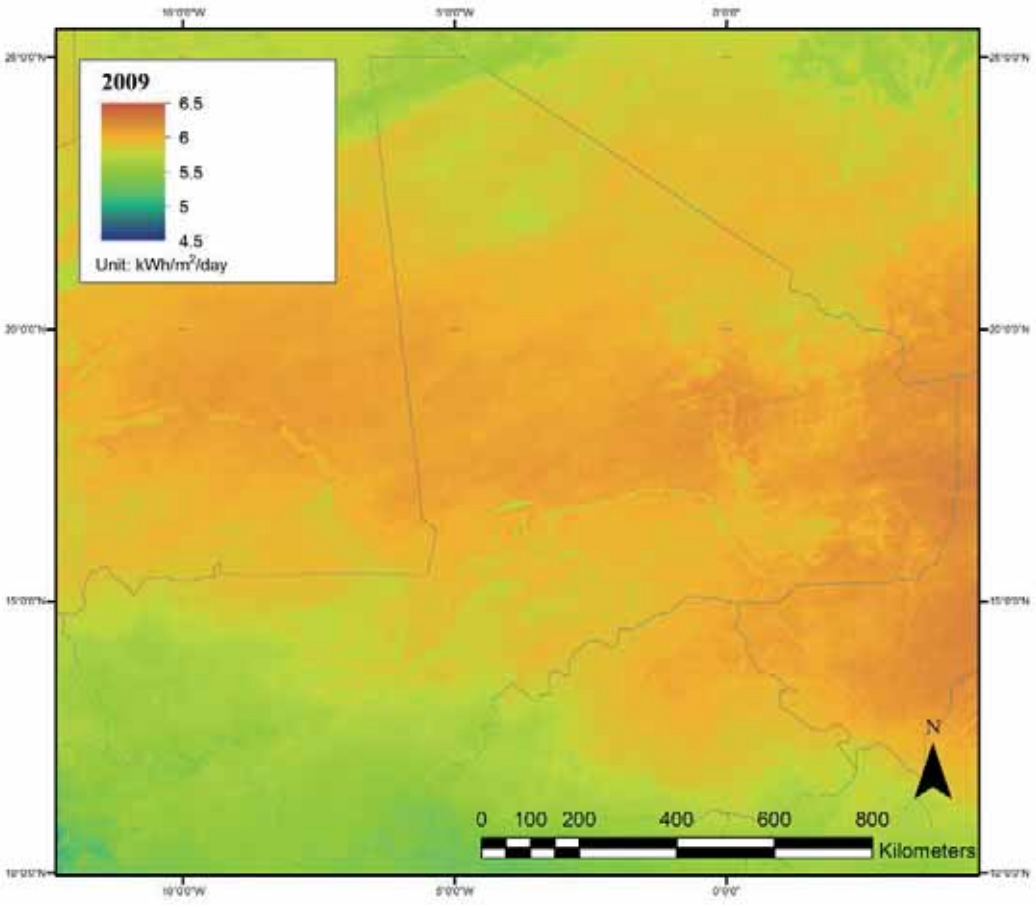
2009
6.5
6
5.5
5
4.5
Unit: kWh/m²/day
N
0 100 200 400 600 800
Kilometers

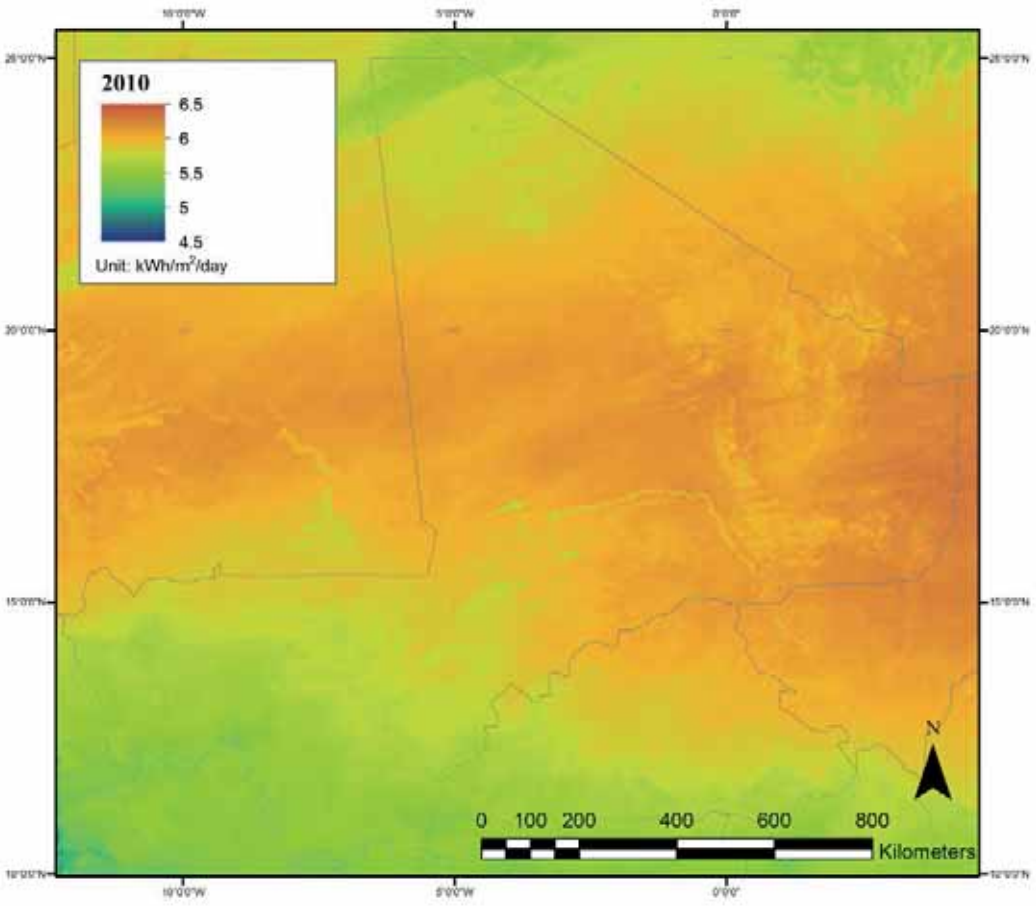
2010
6.5
6
5.5
5
4.5
Unit: kWh/m²/day
N
0 100 200 400 600 800
Kilometers

3 Monthly daily average in kWh/m^2/day for the period between 2008-07-01 and 2011-06-30

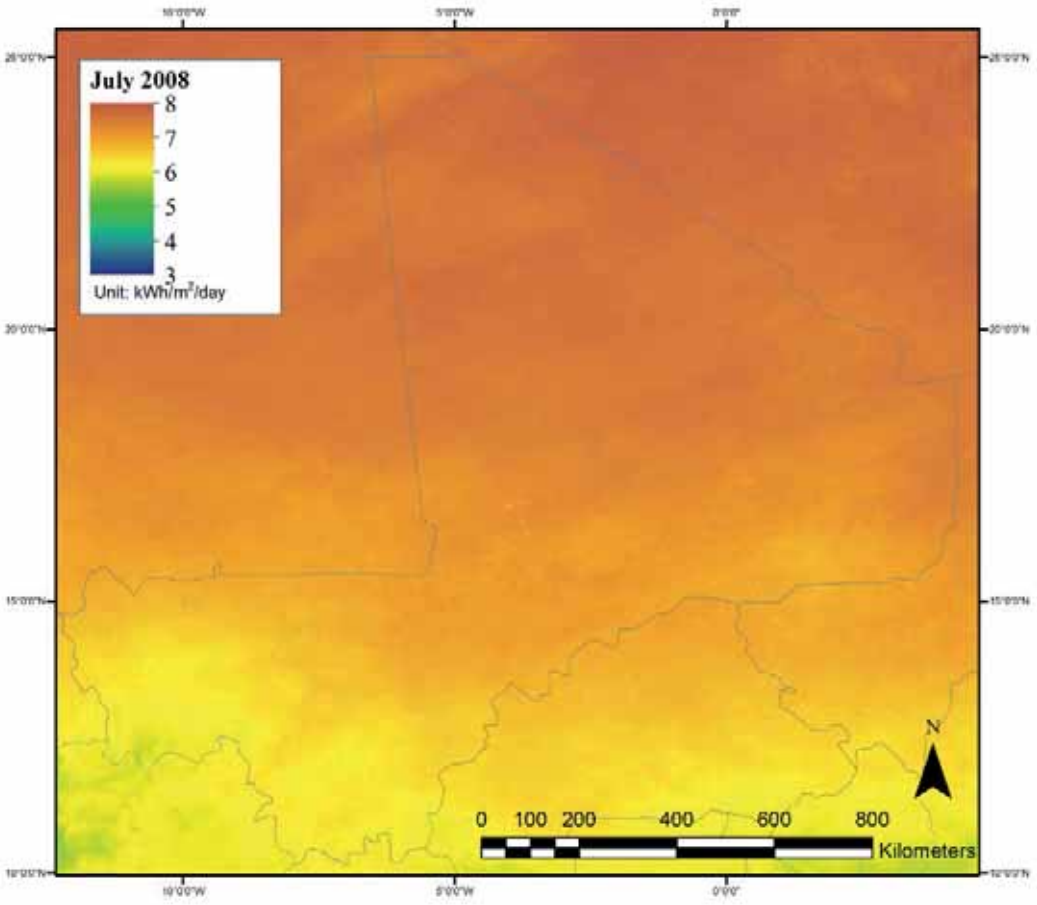
July 2008
8
7
6
5
4
3
Unit: kWh/m²/day
N
0 100 200 400 600 800
Kilometers

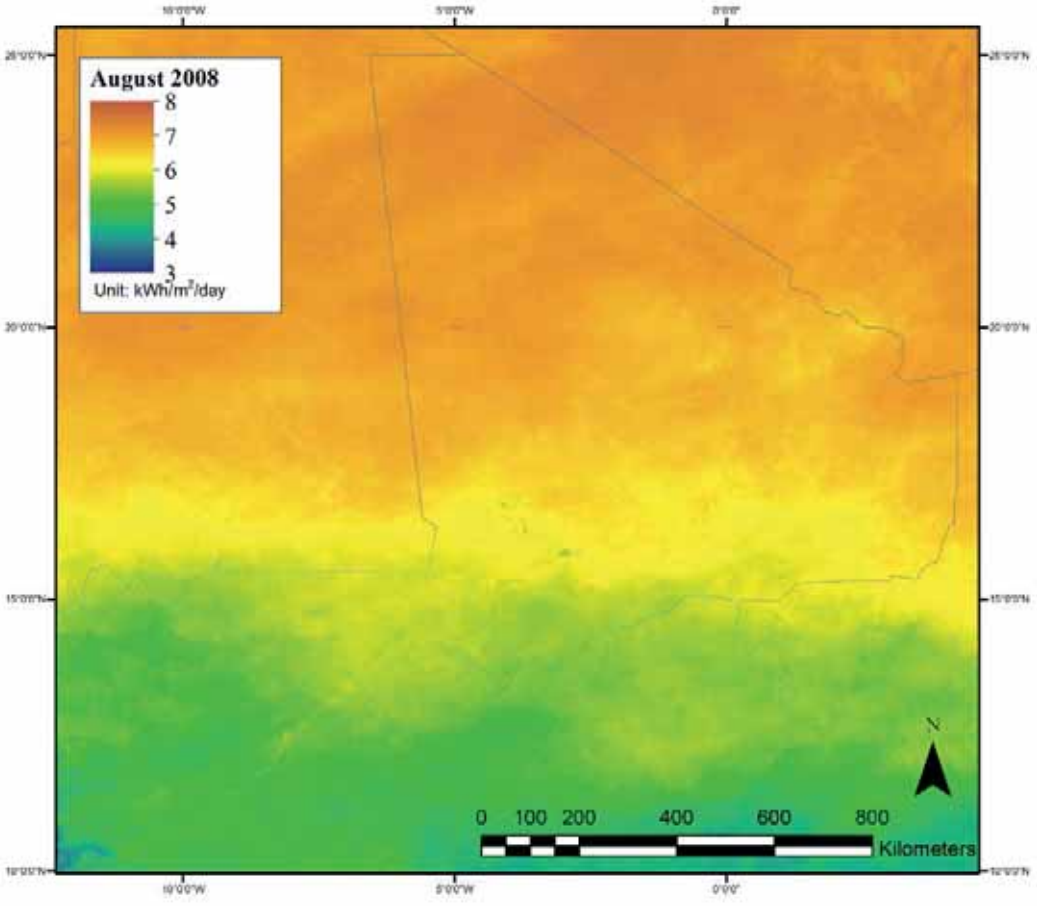
August 2008
8
7
6
5
4
3
Unit: kWh/m²/day
N
0 100 200 400 600 800
Kilometers

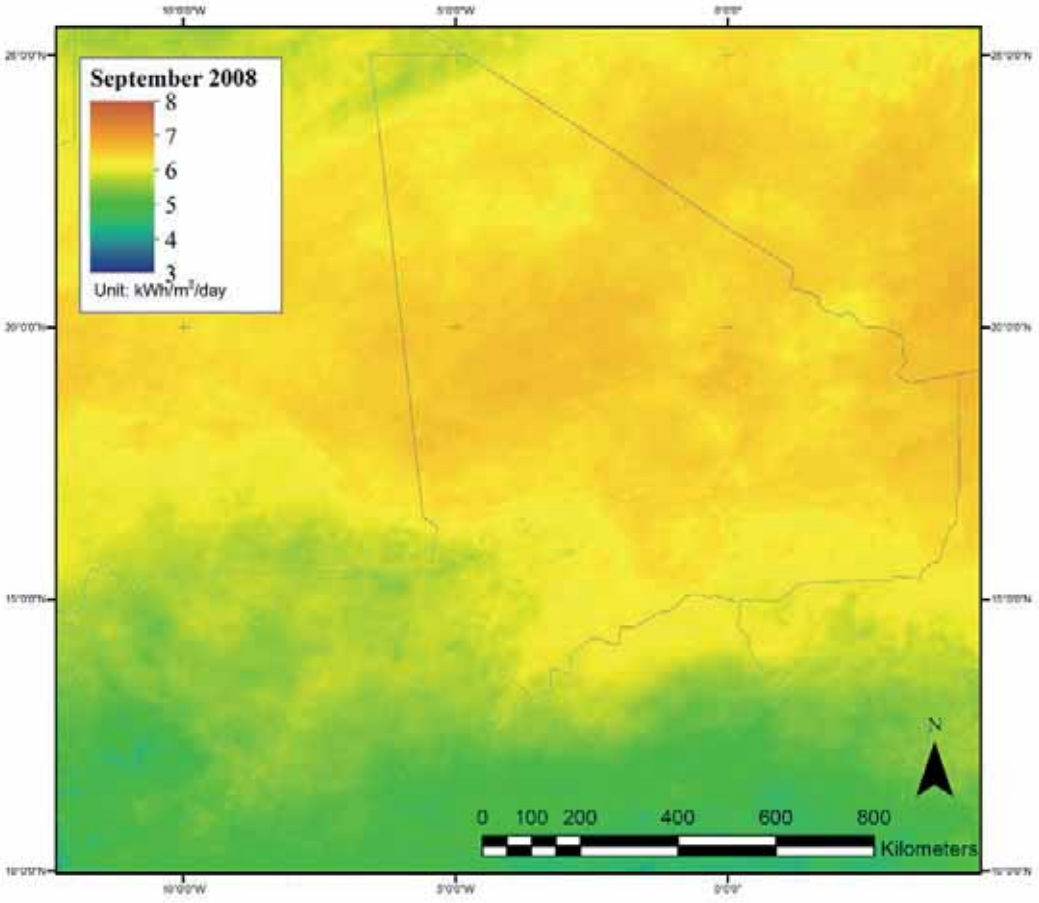
September 2008
8
7
6
5
4
3
Unit: kWh/m²/day
N
0 100 200 400 600 800
Kilometers

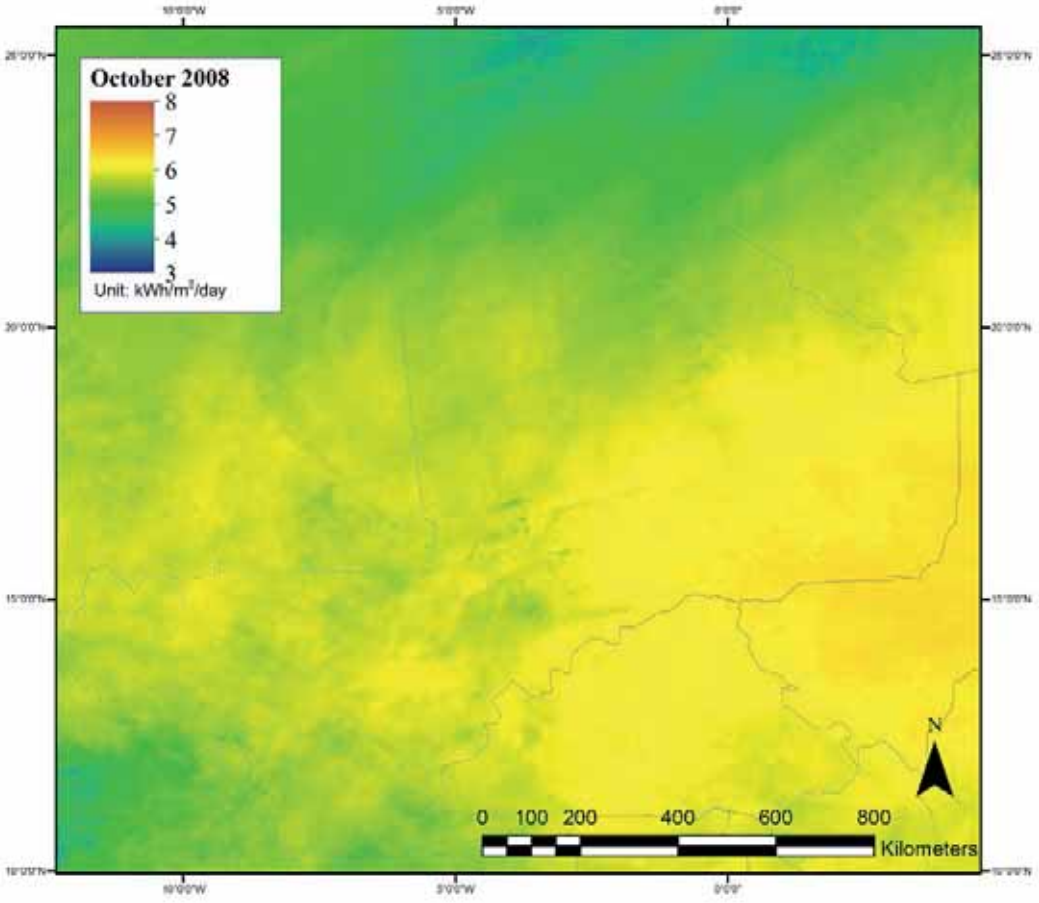
October 2008
8
7
6
5
4
3
Unit: kWh/m²/day
N
0 100 200 400 600 800
Kilometers

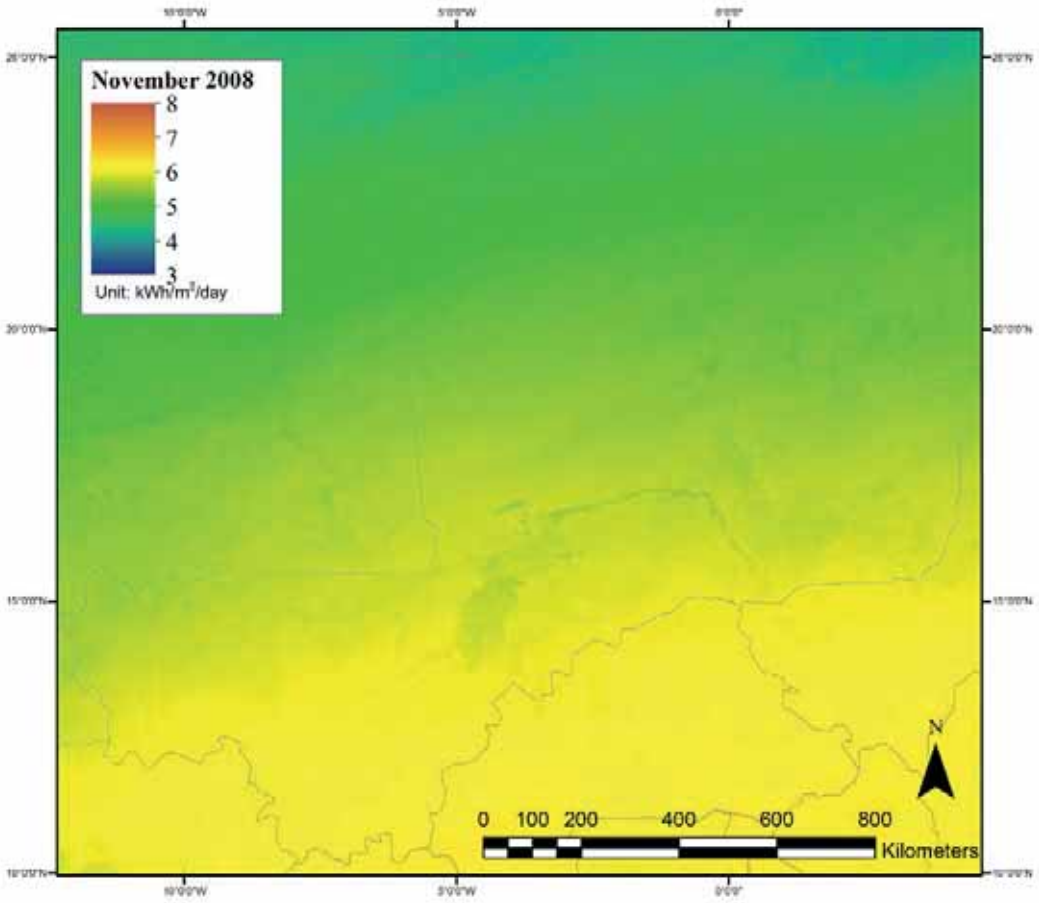
November 2008
8
7
6
5
4
3
Unit: kWh/m²/day
N
0 100 200 400 600 800
Kilometers

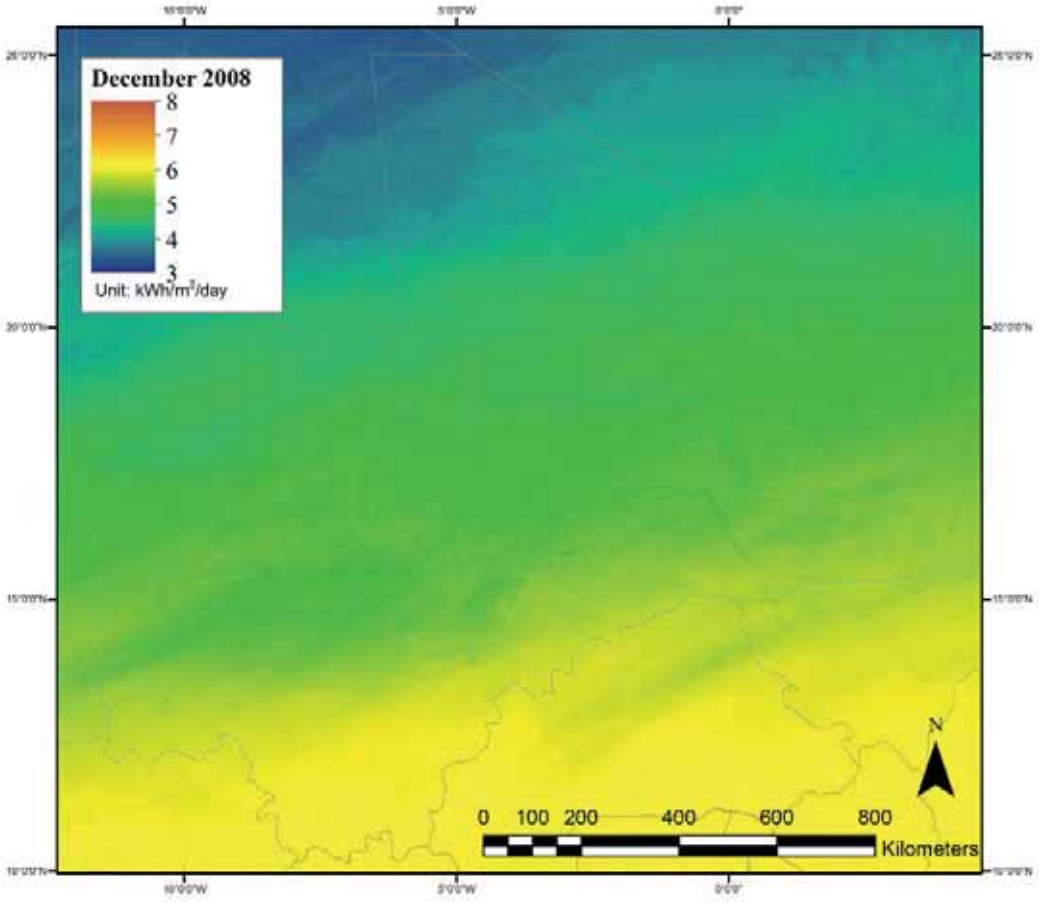
December 2008
8
7
6
5
4
3
Unit: kWh/m²/day
N
0 100 200 400 600 800
Kilometers

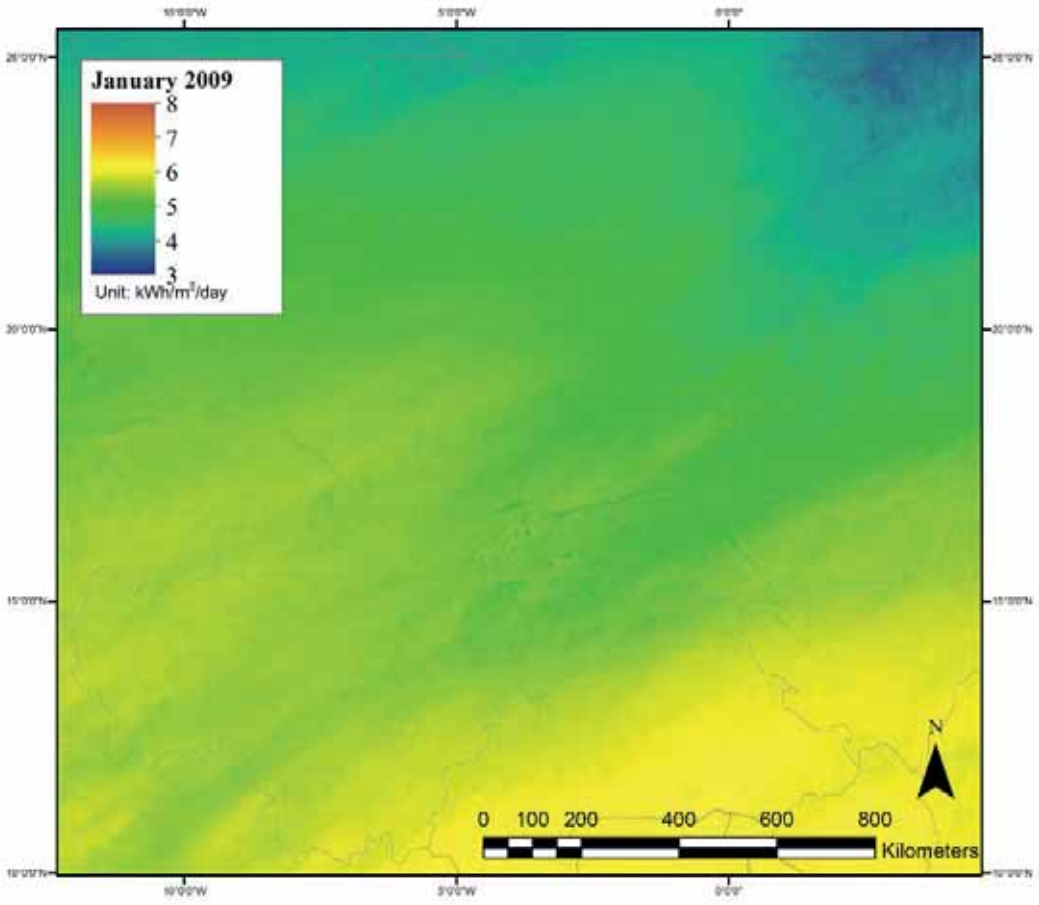
January 2009
8
7
6
5
4
3
Unit: kWh/m²/day
N
0 100 200 400 600 800
Kilometers

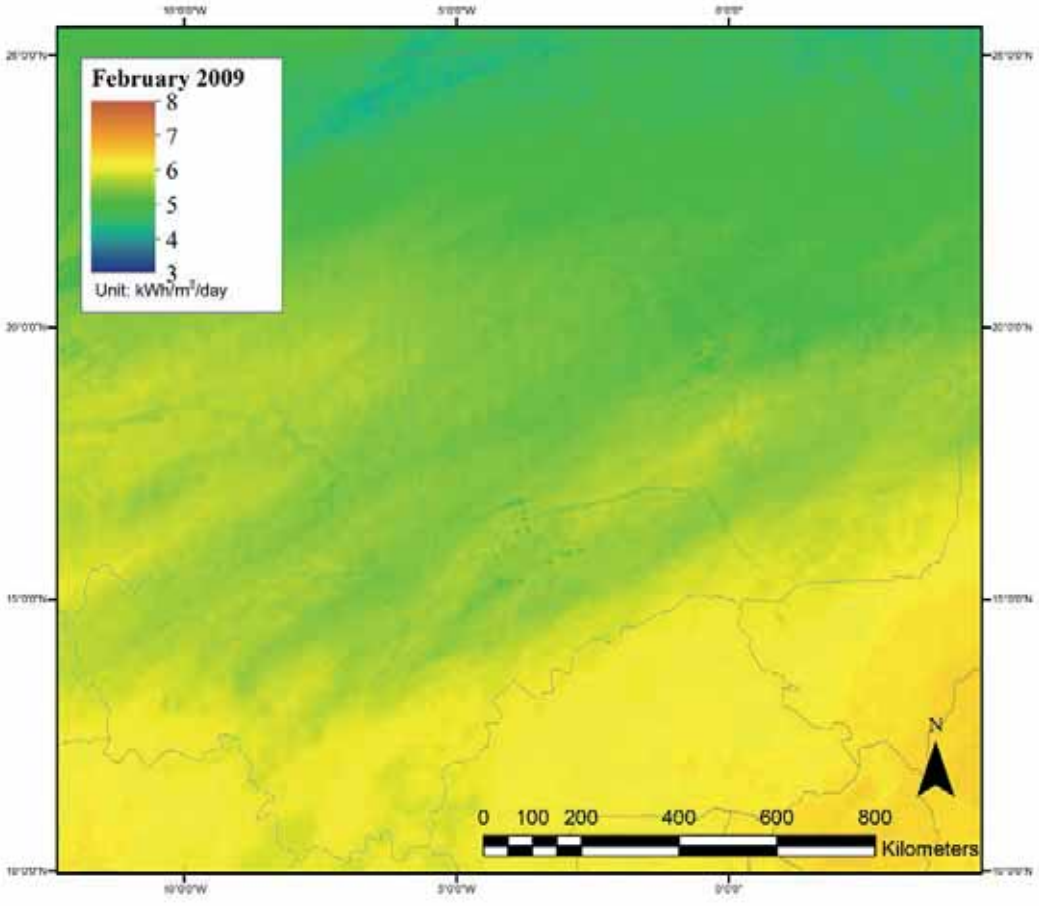
February 2009
8
7
6
5
4
3
Unit: kWh/m²/day
N
0 100 200 400 600 800
Kilometers

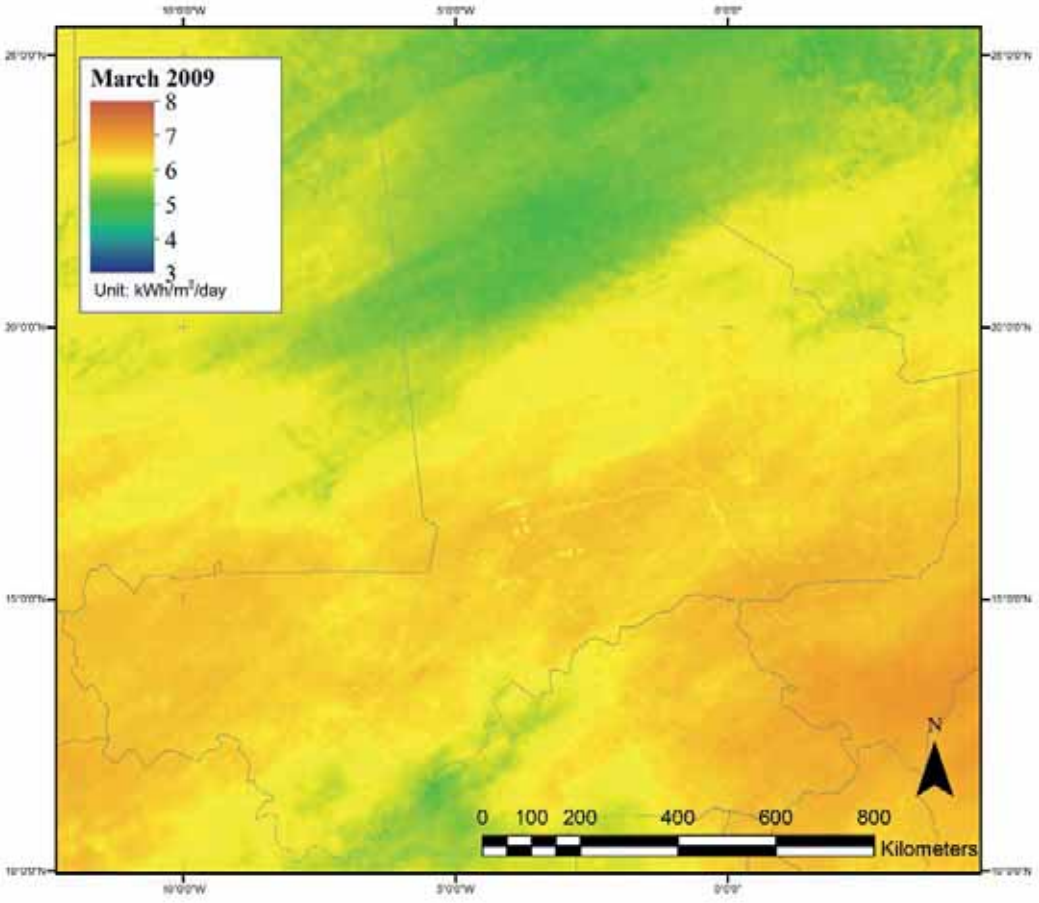
March 2009
8
7
6
5
4
3
Unit: kWh/m²/day
N
0 100 200 400 600 800
Kilometers

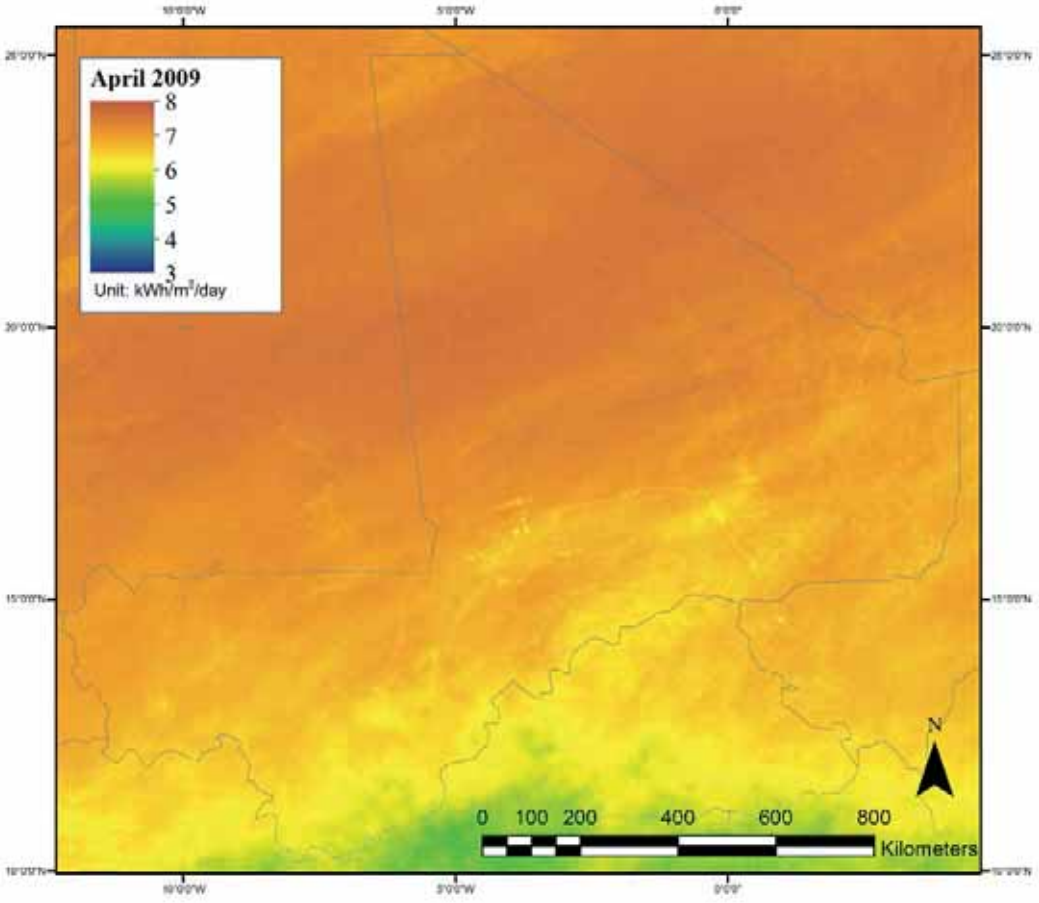
April 2009
8
7
6
5
4
3
Unit: kWh/m²/day
N
0 100 200 400 600 800
Kilometers

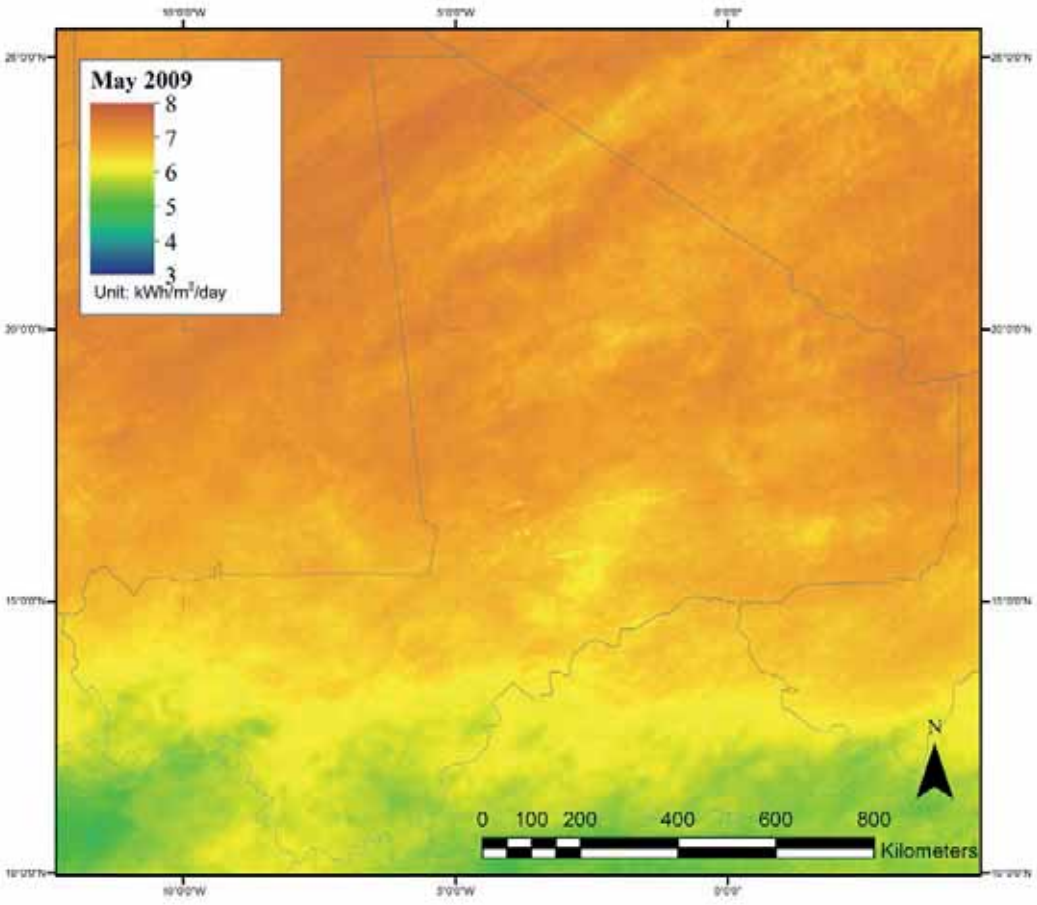
May 2009
8
7
6
5
4
3
Unit: kWh/m²/day
N
0 100 200 400 600 800
Kilometers

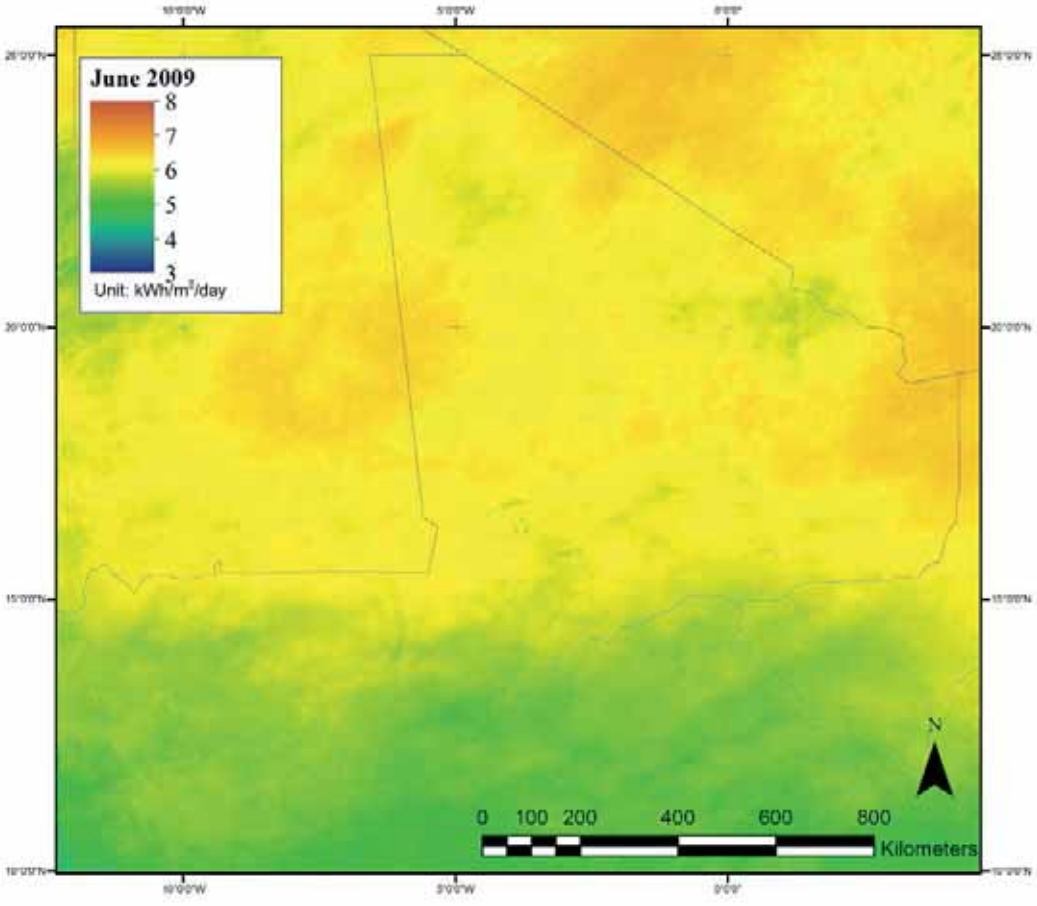
June 2009
8
7
6
5
4
3
Unit: kWh/m²/day
N
0 100 200 400 600 800
Kilometers

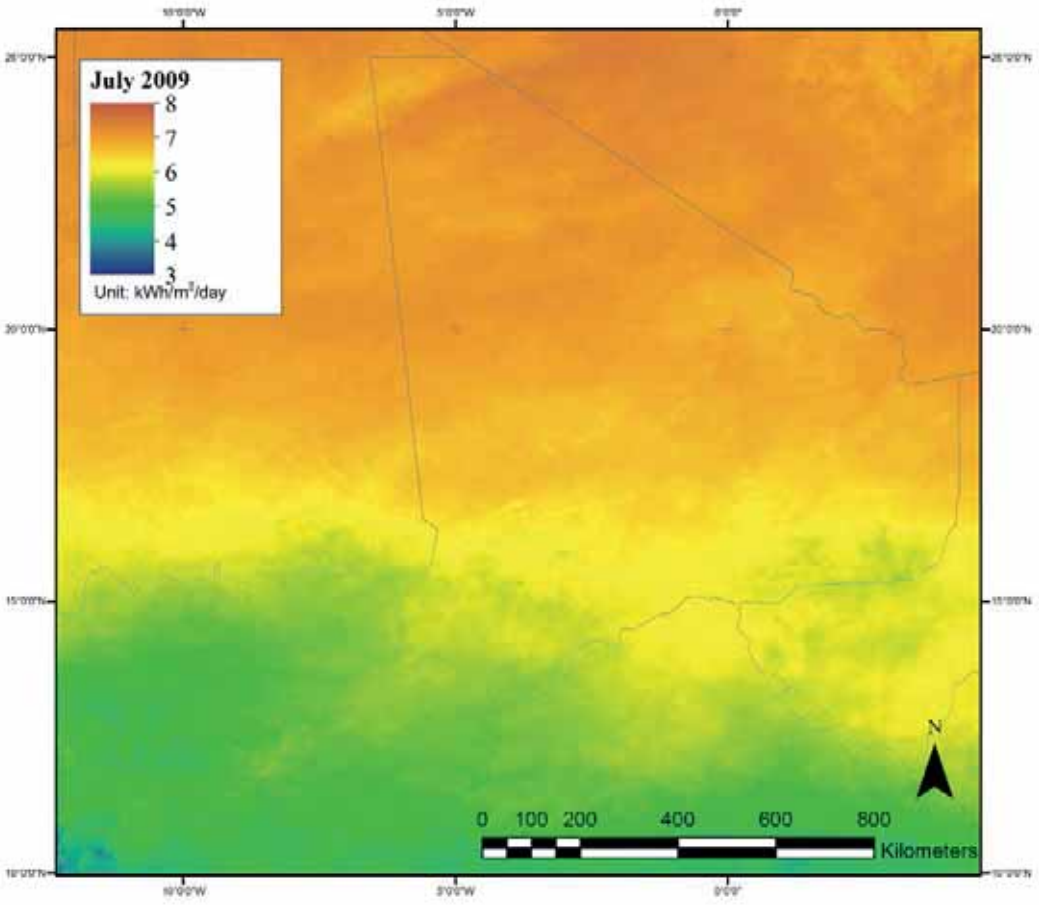
July 2009
8
7
6
5
4
3
Unit: kWh/m²/day
N
0 100 200 400 600 800
Kilometers

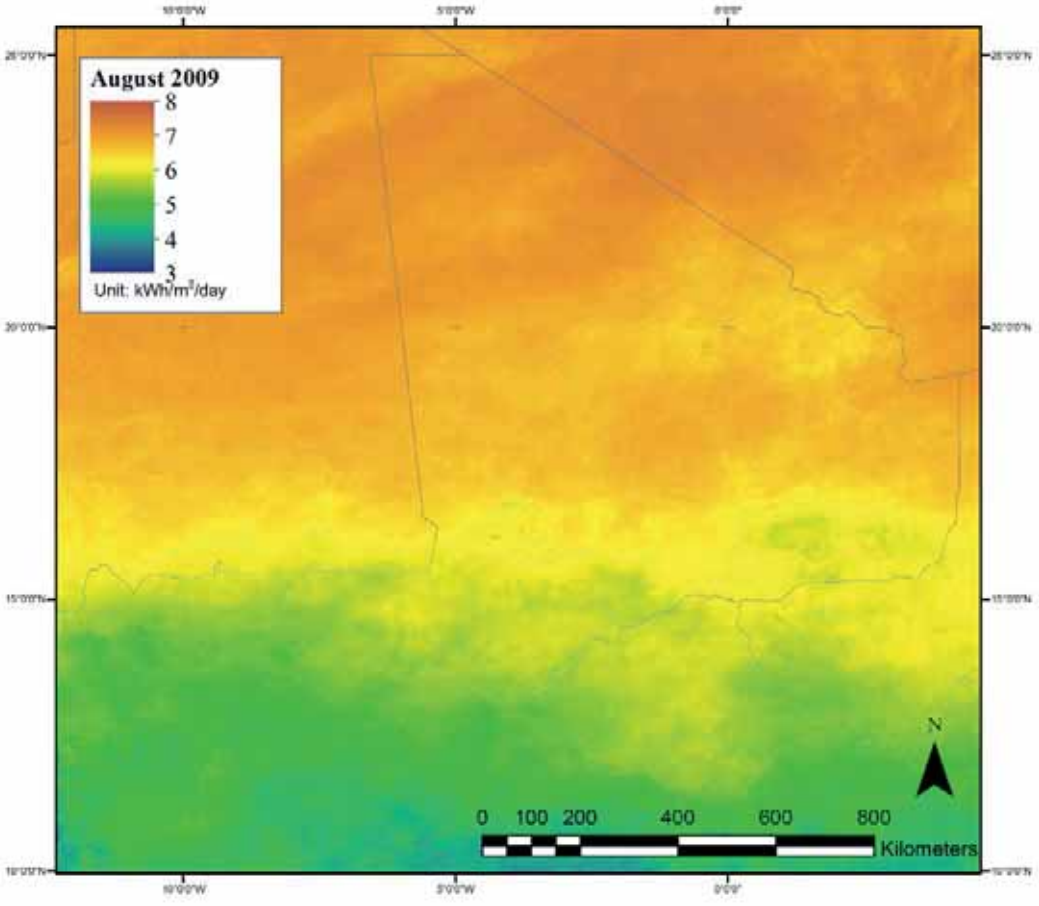
August 2009
8
7
6
5
4
3
Unit: kWh/m²/day
N
0 100 200 400 600 800
Kilometers

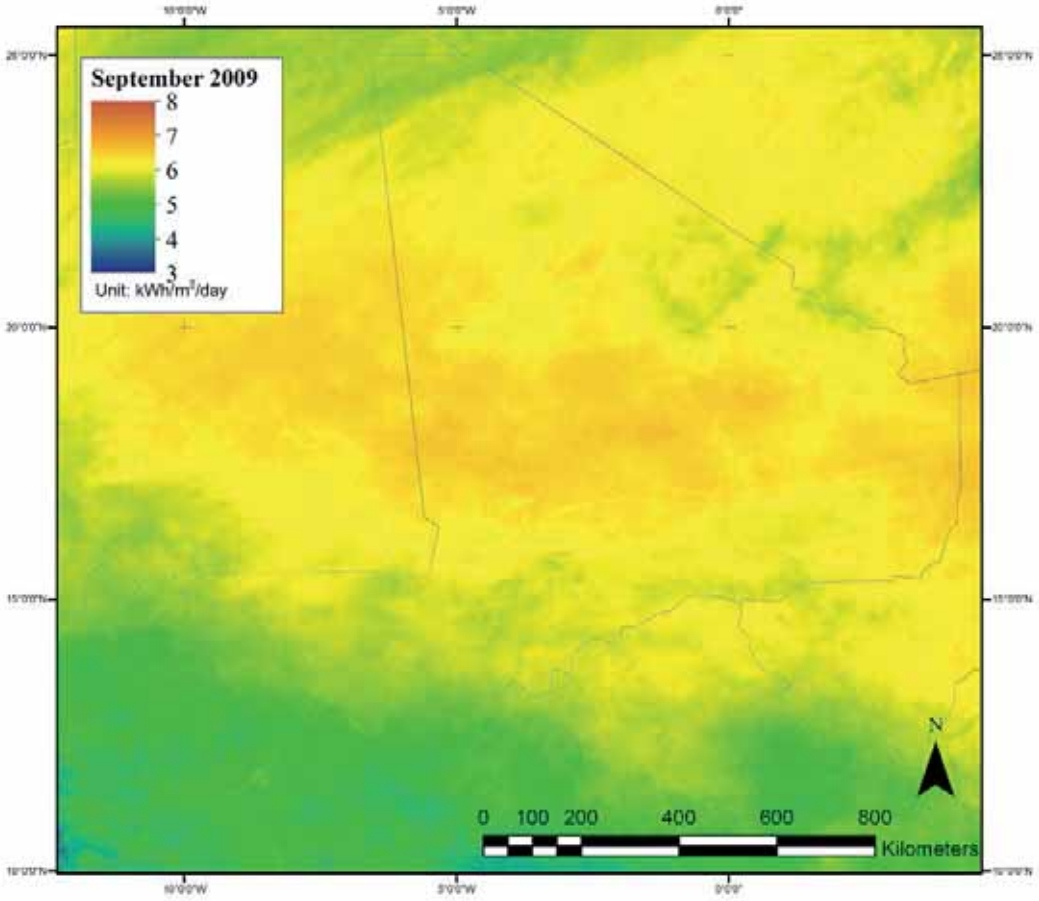
September 2009
8
7
6
5
4
3
Unit: kWh/m²/day
N
0 100 200 400 600 800
Kilometers

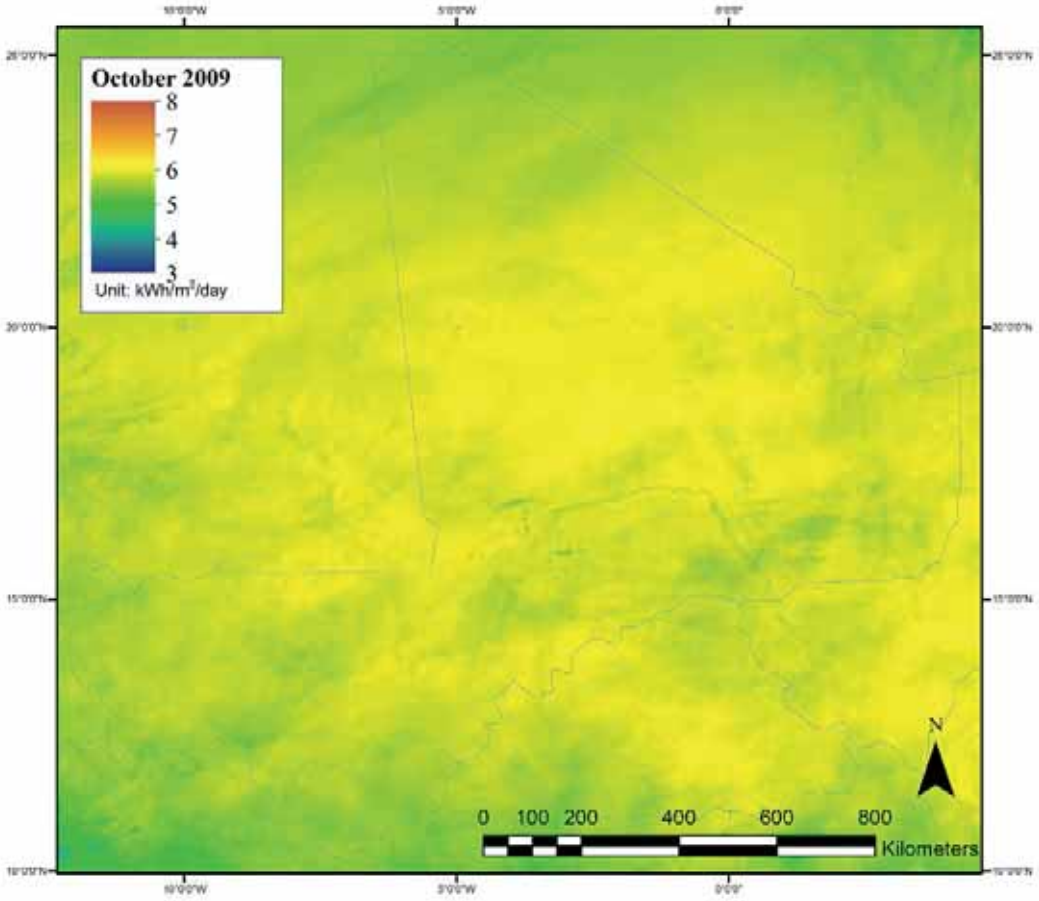
October 2009
8
7
6
5
4
3
Unit: kWh/m²/day
N
0 100 200 400 600 800
Kilometers

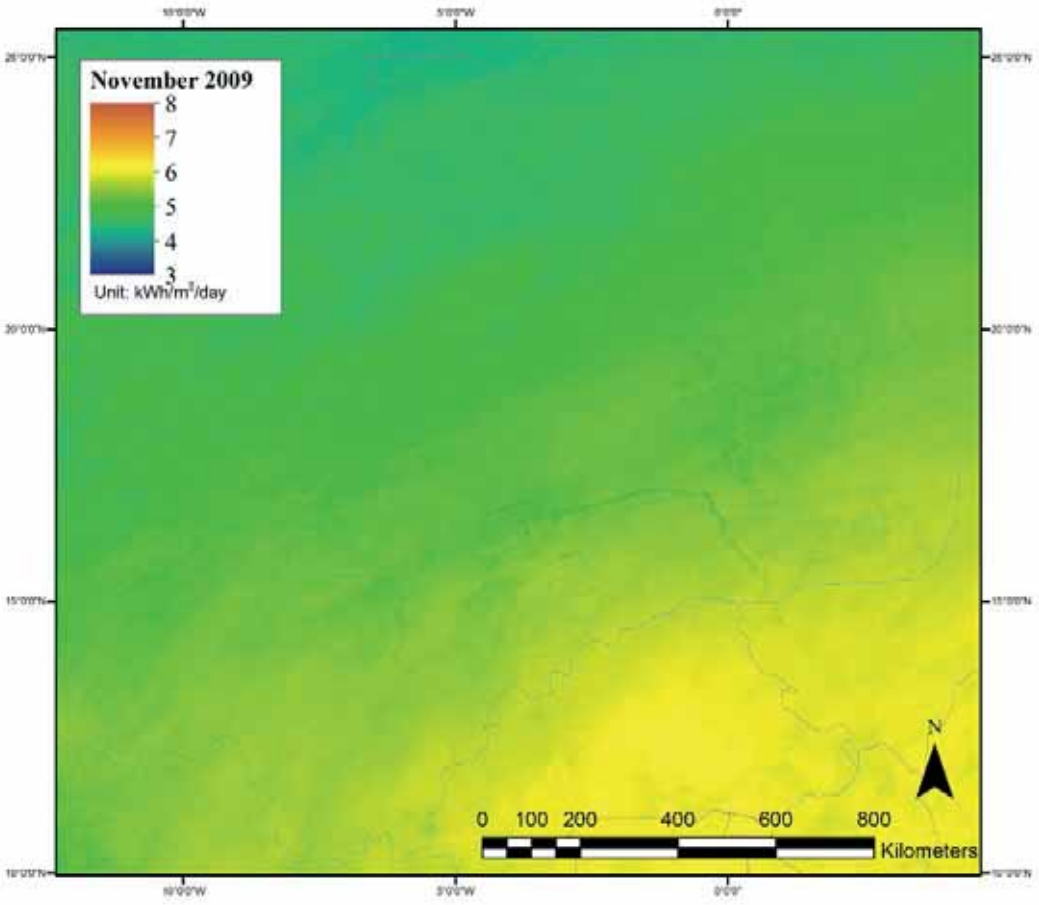
November 2009
8
7
6
5
4
3
Unit: kWh/m²/day
N
0 100 200 400 600 800
Kilometers

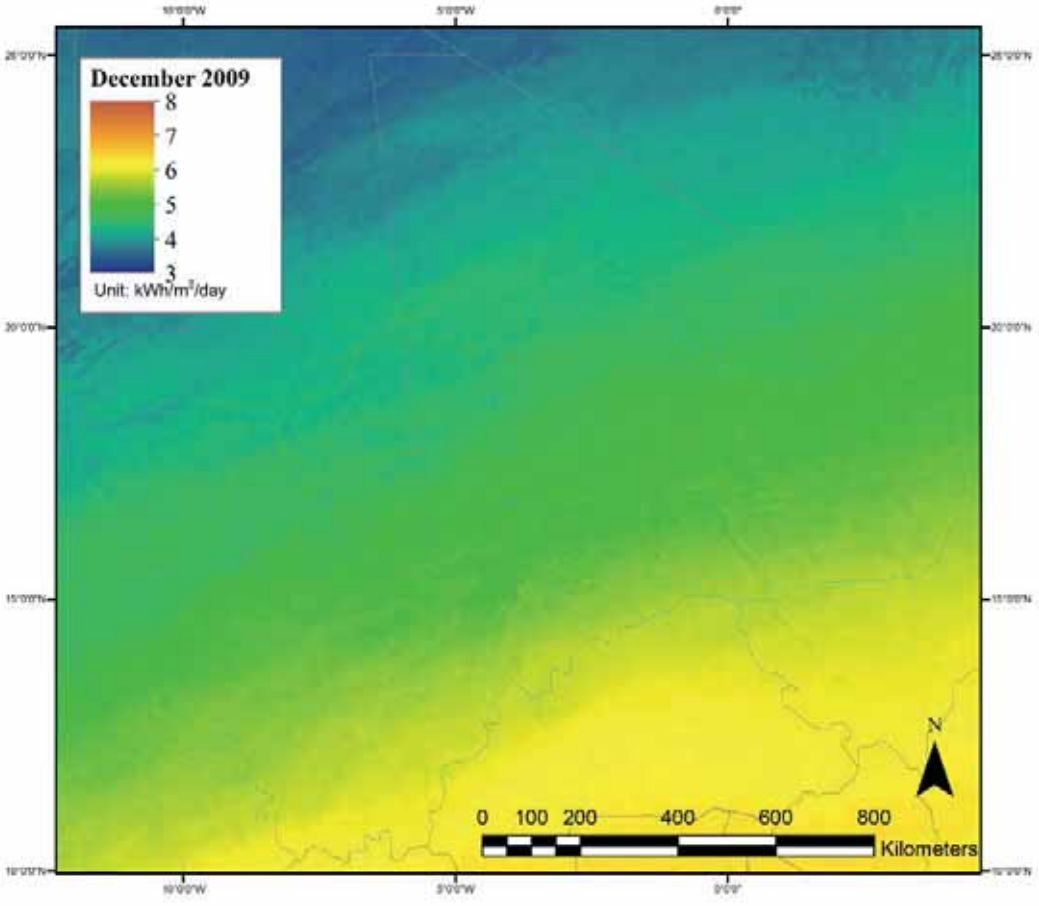
December 2009
8
7
6
5
4
3
Unit: kWh/m²/day
N
0 100 200 400 600 800
Kilometers

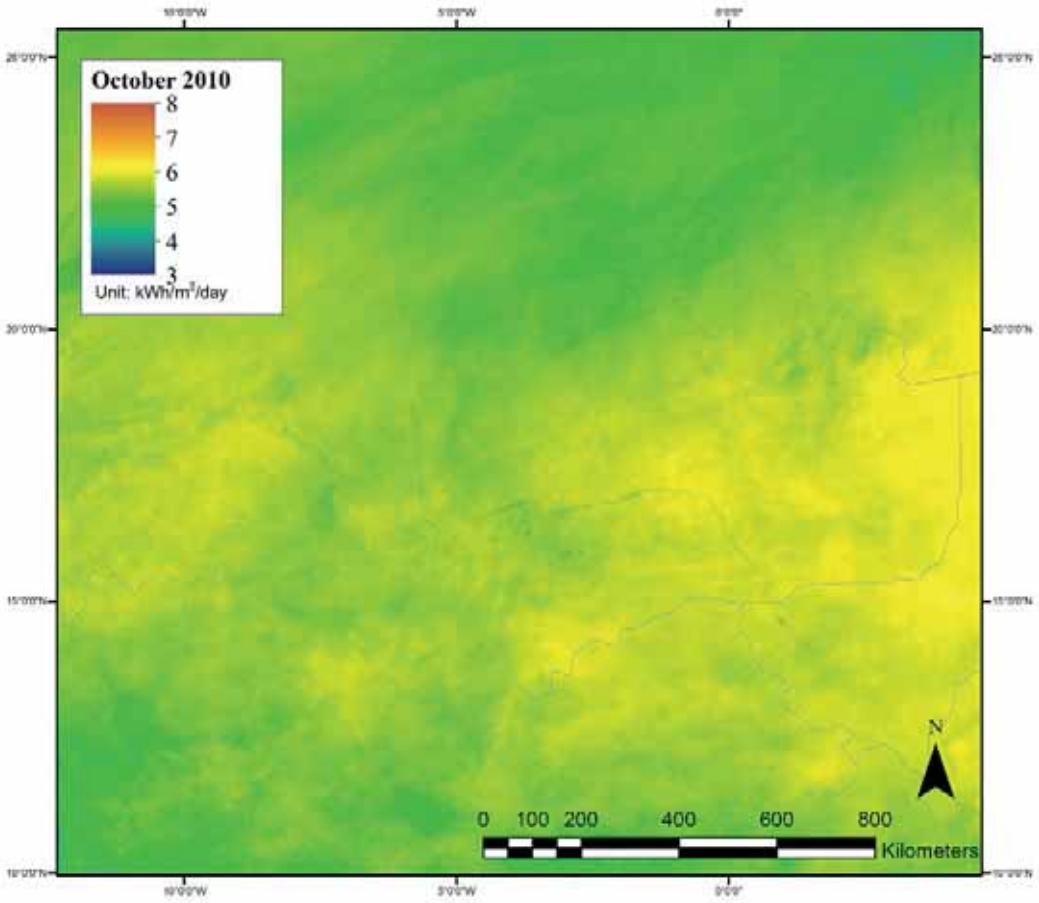
October 2010
8
7
6
5
4
3
Unit: kWh/m²/day
N
0 100 200 400 600 800
Kilometers

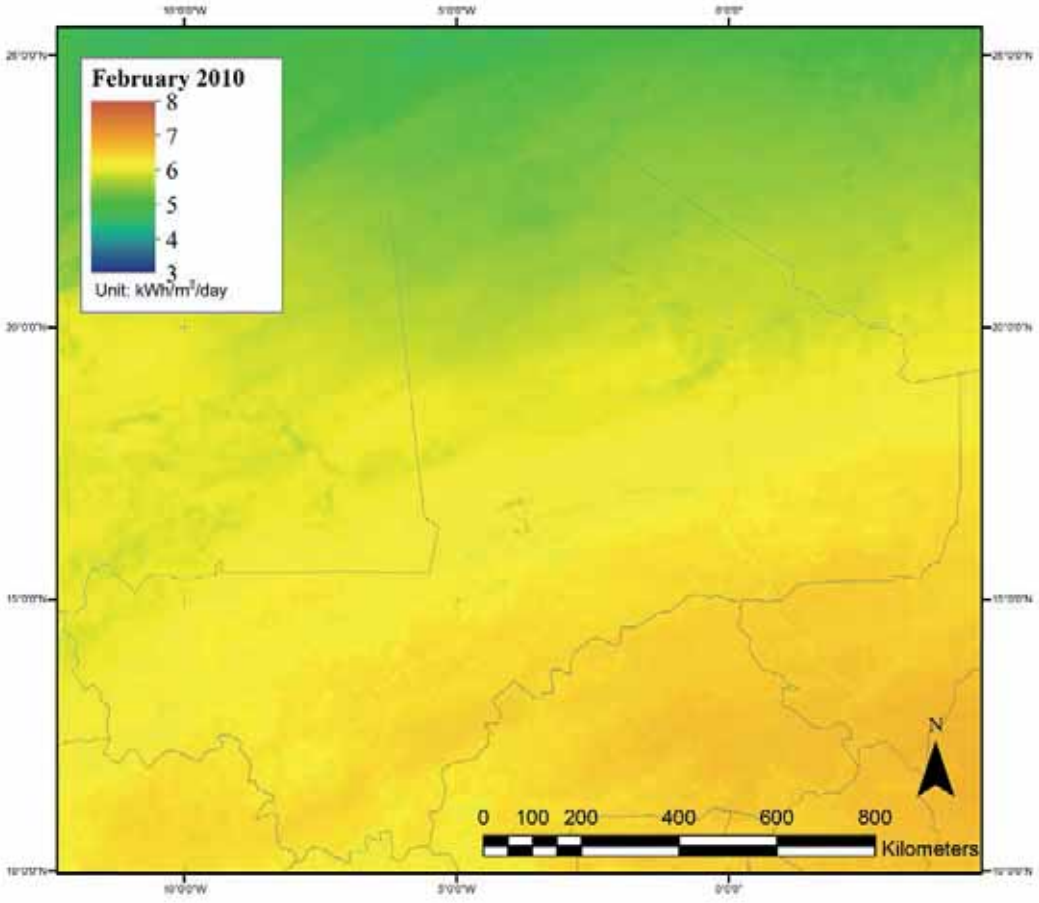
February 2010
8
7
6
5
4
3
Unit: kWh/m²/day
N
0 100 200 400 600 800
Kilometers

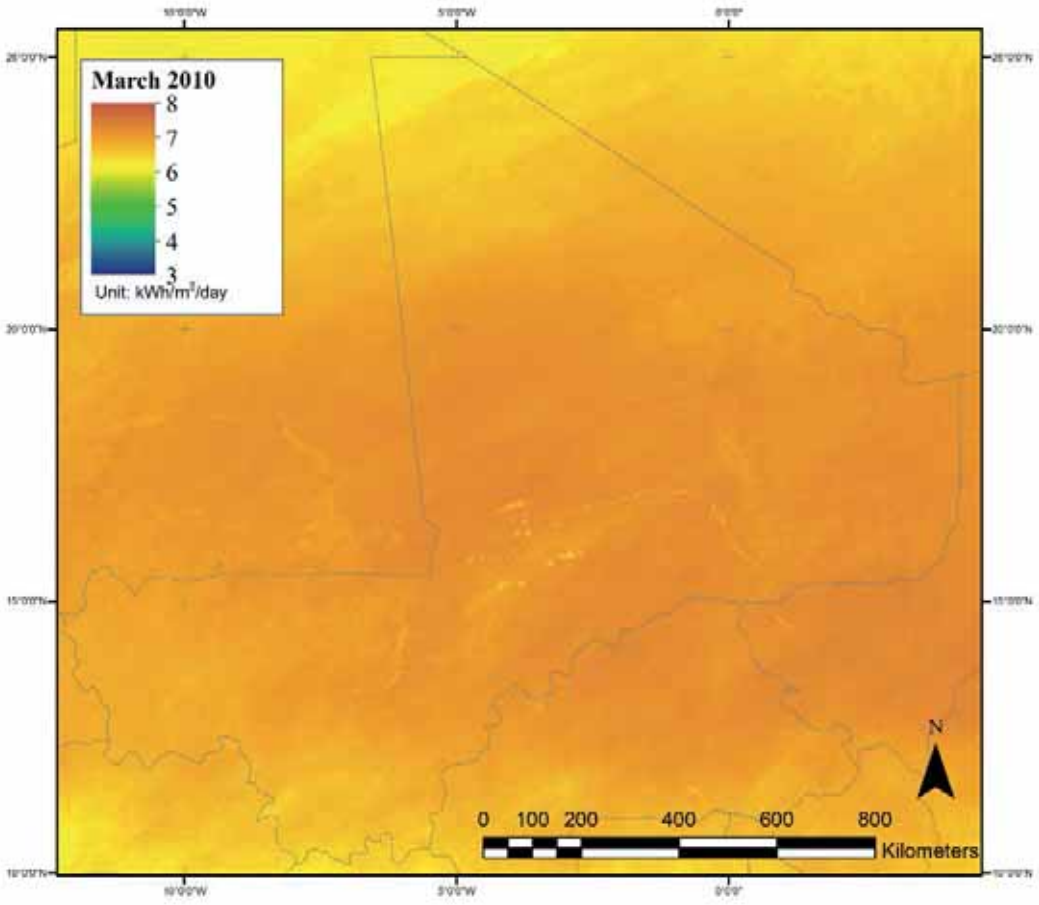
March 2010
8
7
6
5
4
3
Unit: kWh/m²/day
N
0 100 200 400 600 800
Kilometers

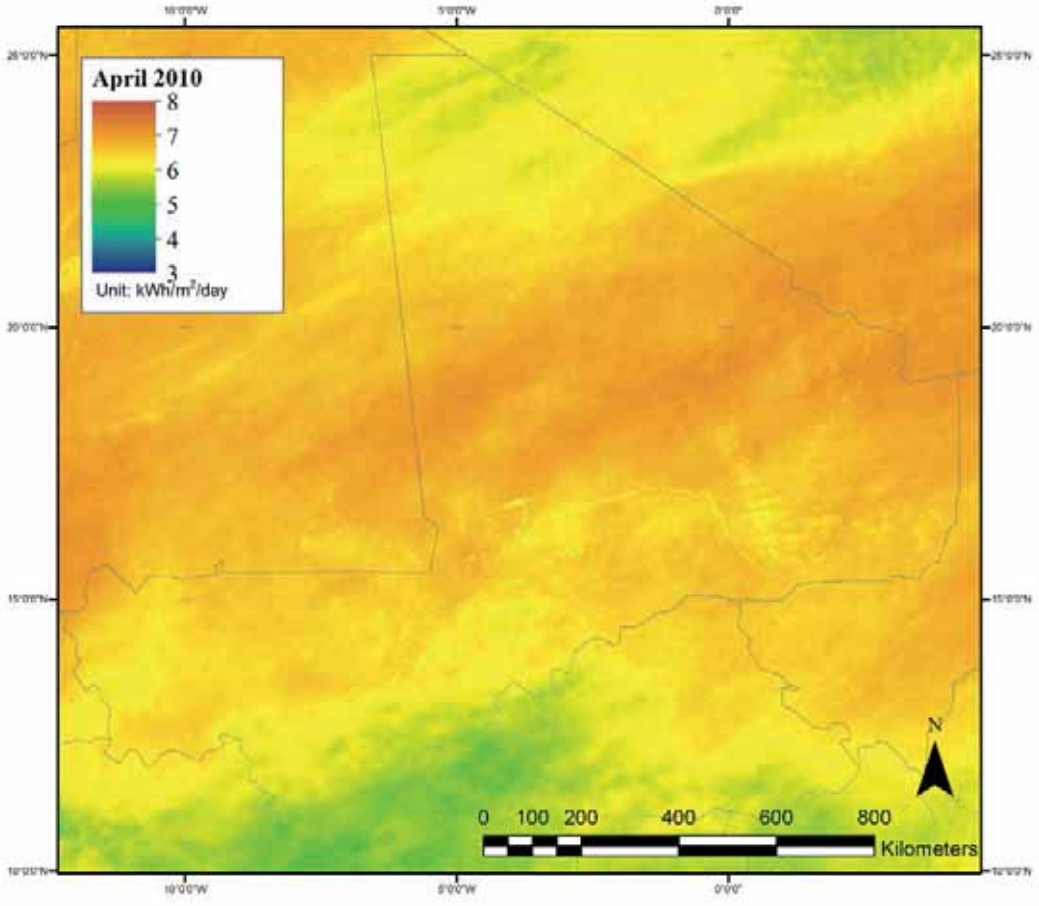
April 2010
8
7
6
5
4
3
Unit: kWh/m²/day
N
0 100 200 400 600 800
Kilometers

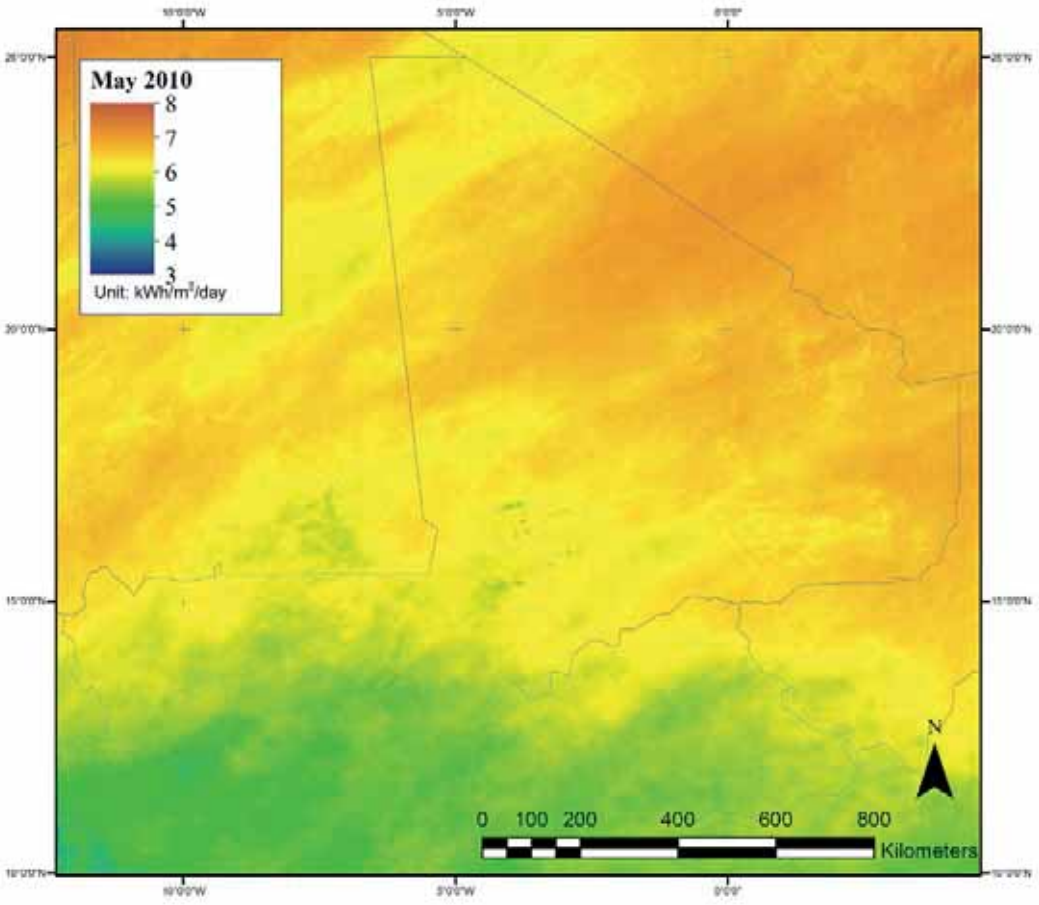
May 2010
8
7
6
5
4
3
Unit: kWh/m²/day
N
0 100 200 400 600 800
Kilometers

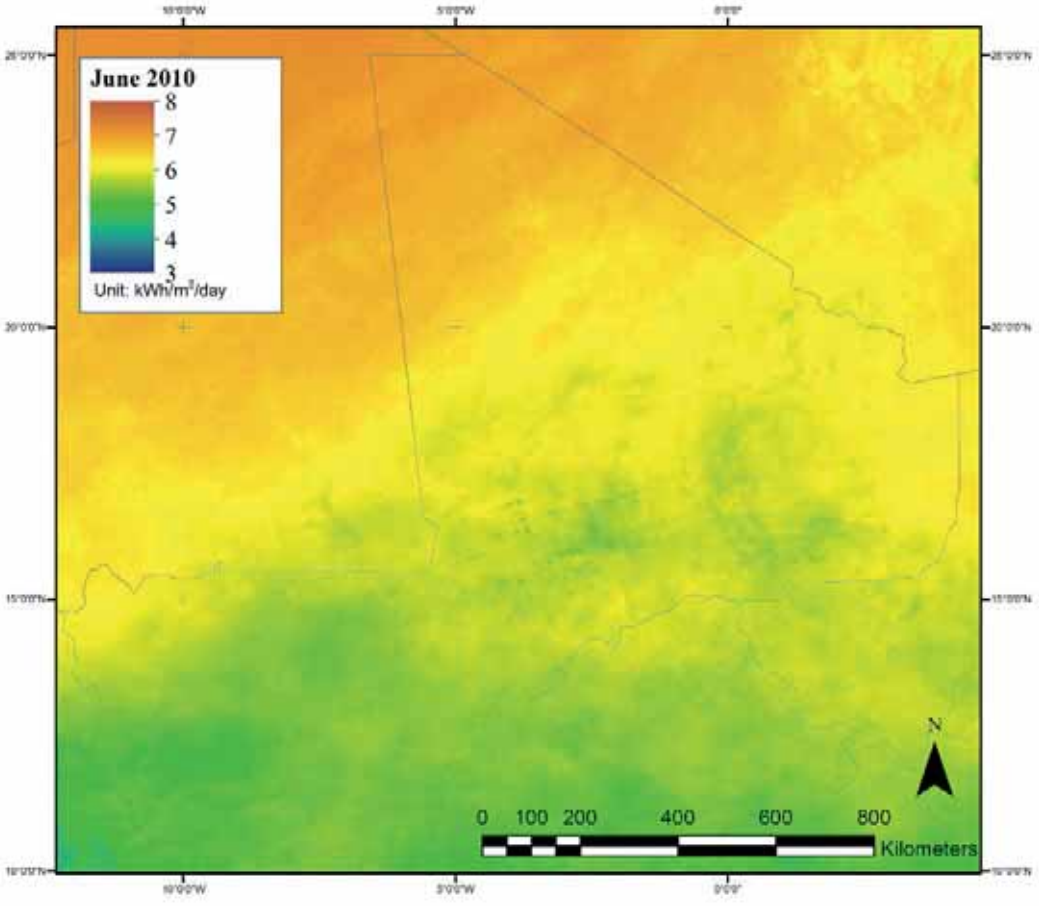
June 2010
8
7
6
5
4
3
Unit: kWh/m²/day
N
0 100 200 400 600 800
Kilometers

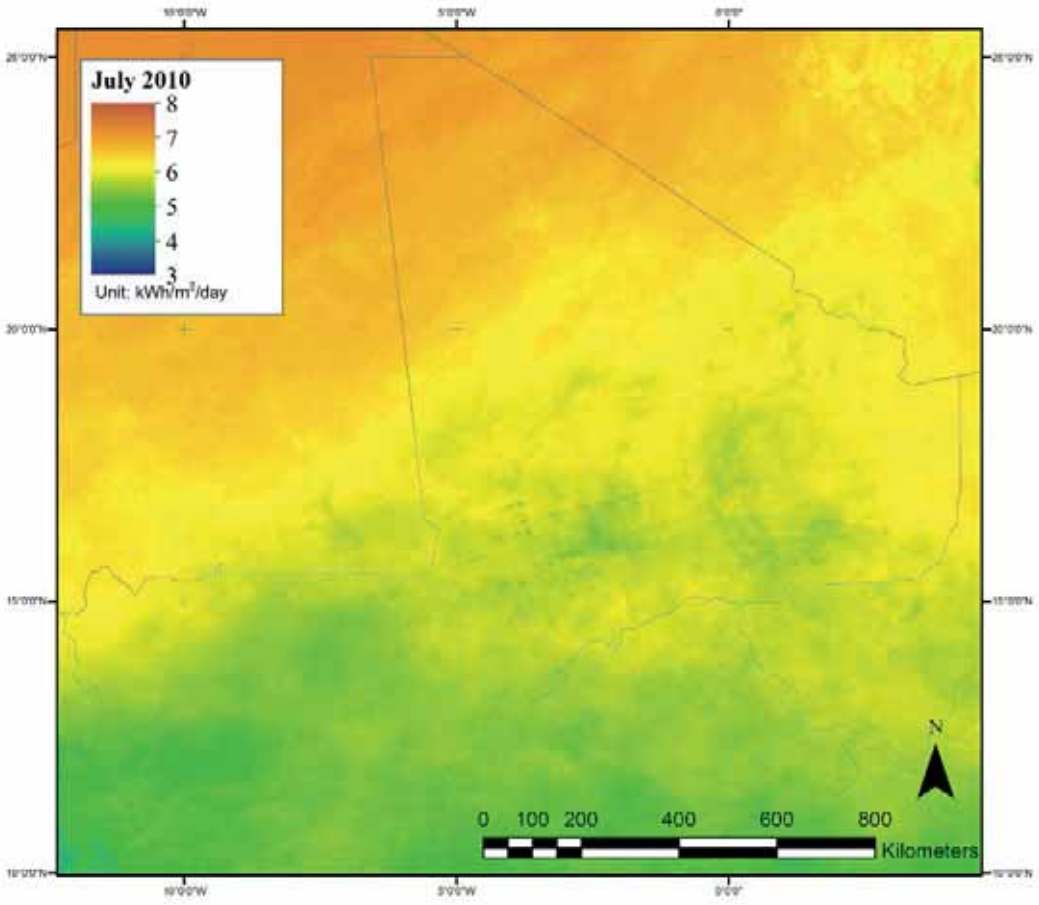
July 2010
8
7
6
5
4
3
Unit: kWh/m²/day
N
0 100 200 400 600 800
Kilometers

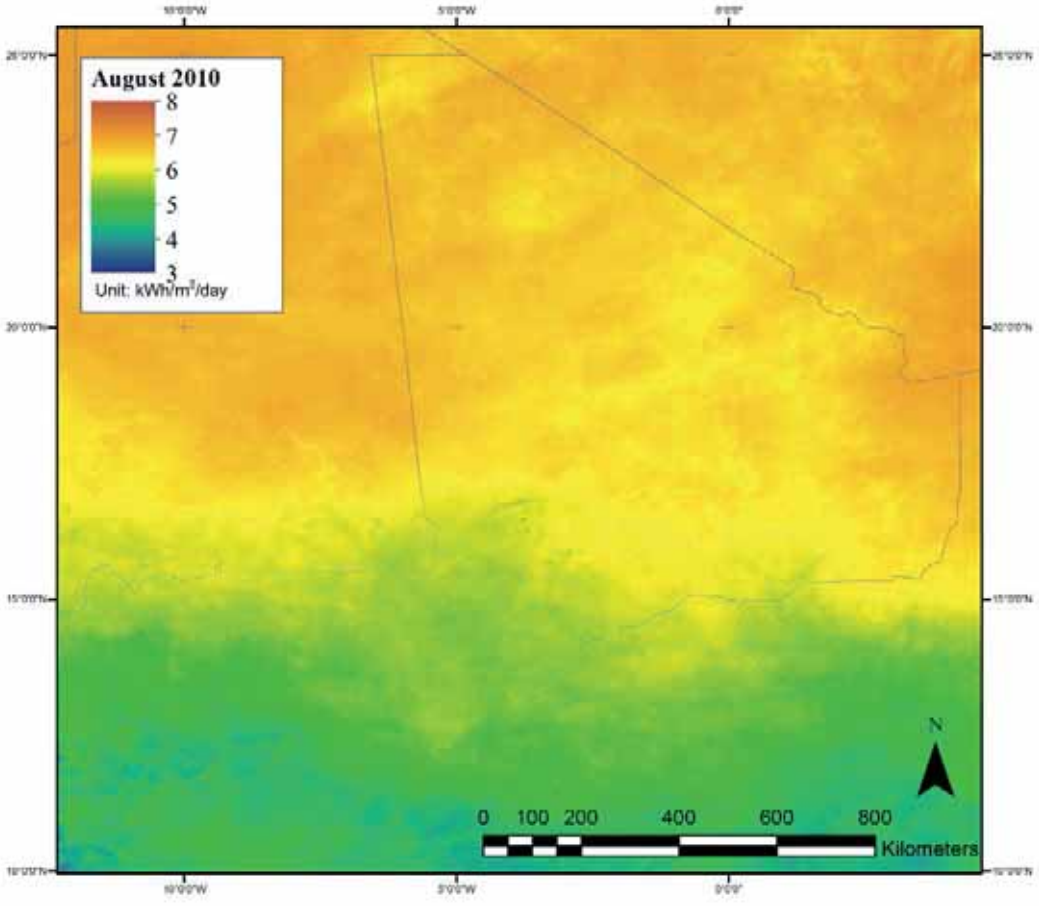
August 2010
8
7
6
5
4
3
Unit: kWh/m²/day
N
0 100 200 400 600 800
Kilometers

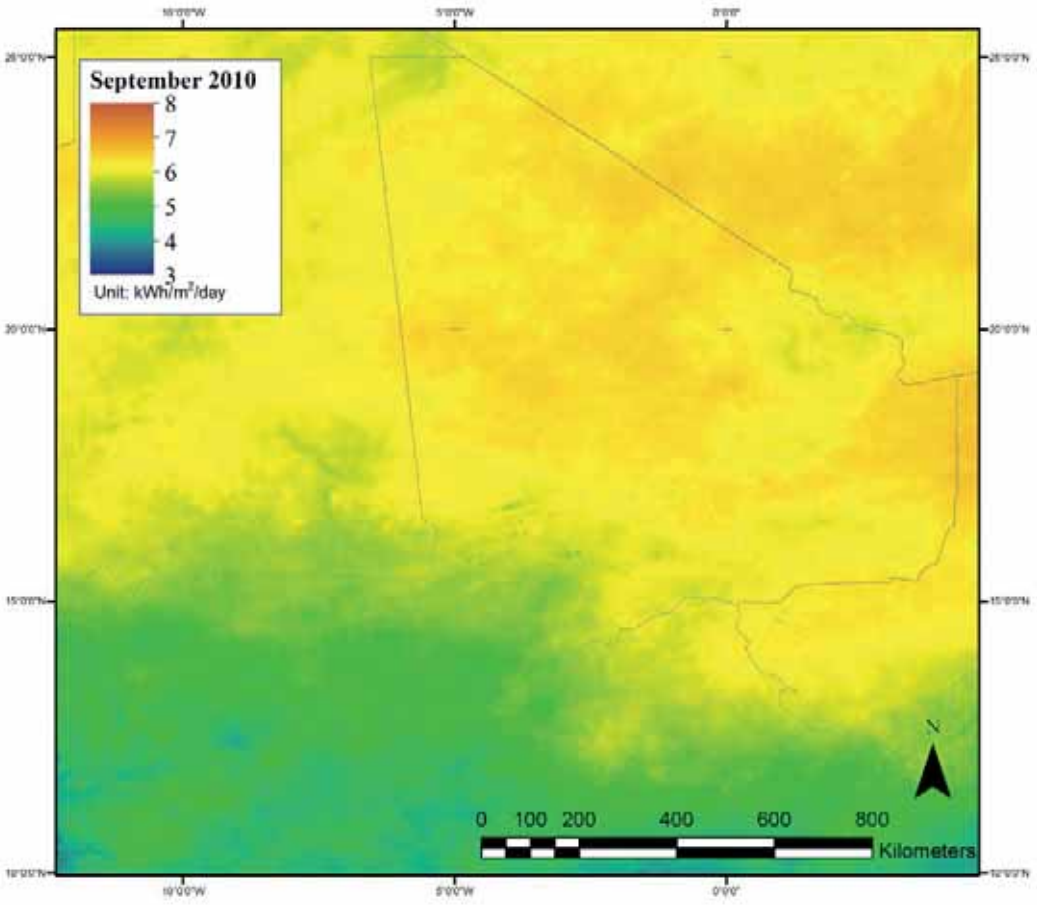
September 2010
8
7
6
5
4
3
Unit: kWh/m²/day
N
0 100 200 400 600 800
Kilometers

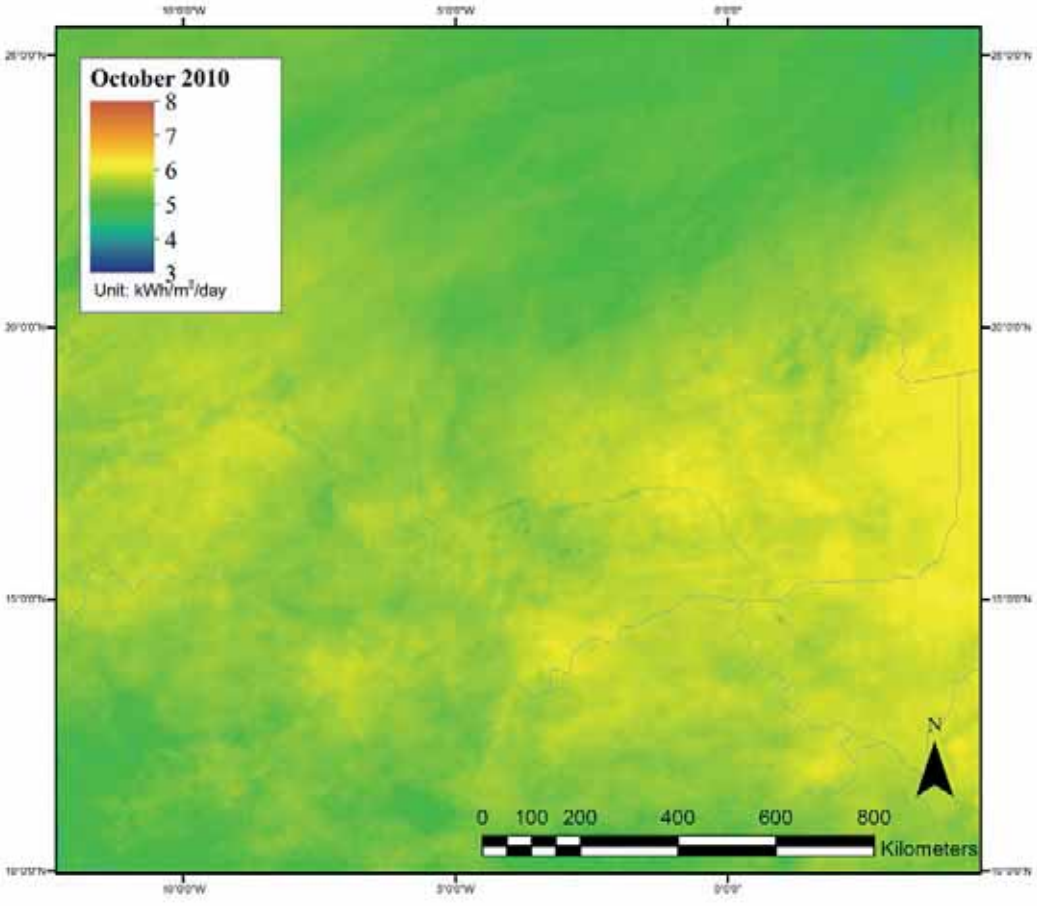
October 2010
8
7
6
5
4
3
Unit: kWh/m²/day
N
0 100 200 400 600 800
Kilometers

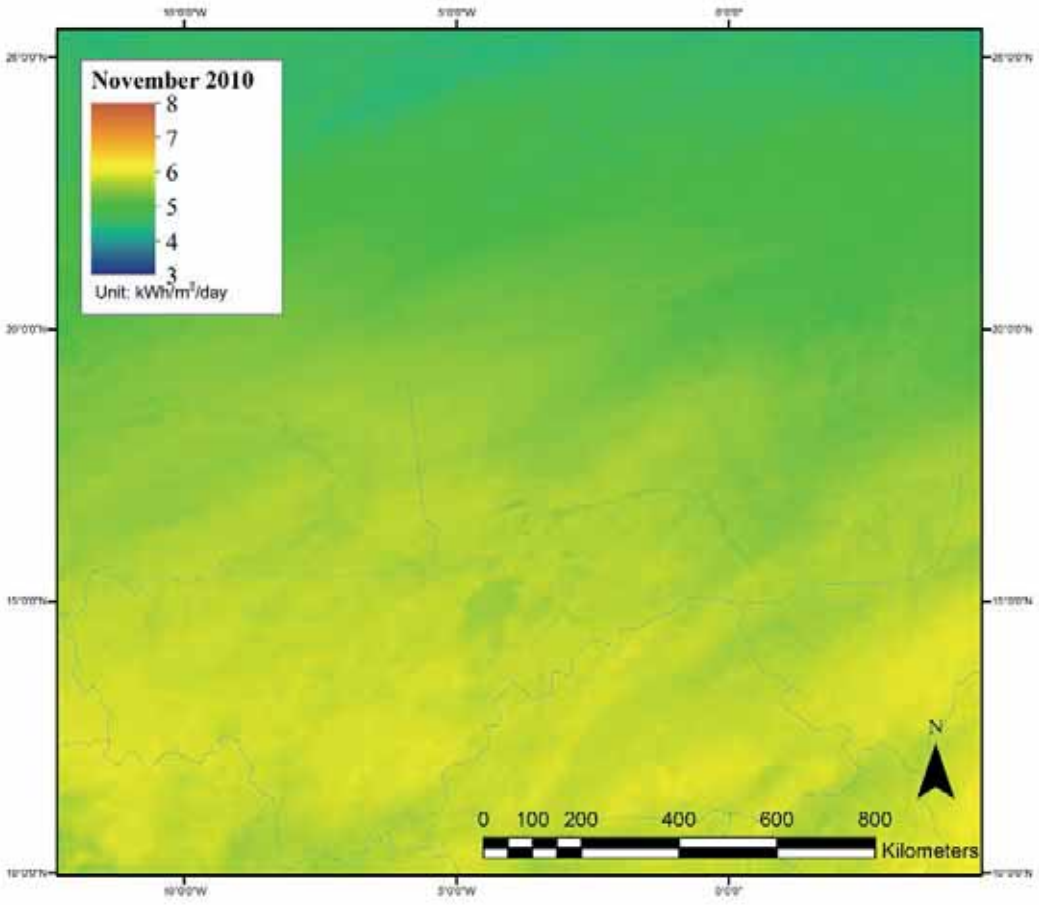
November 2010
8
7
6
5
4
3
Unit: kWh/m²/day
N
0 100 200 400 600 800
Kilometers

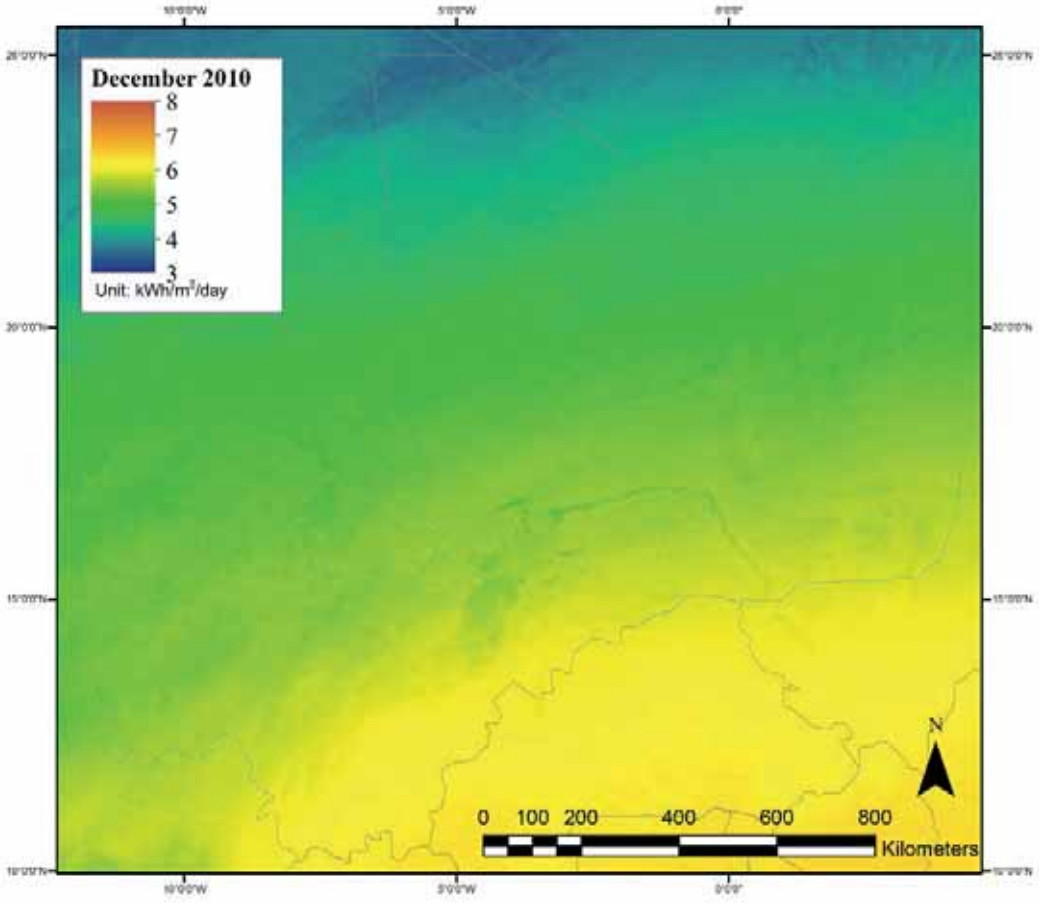
December 2010
8
7
6
5
4
3
Unit: kWh/m²/day
N
0 100 200 400 600 800
Kilometers

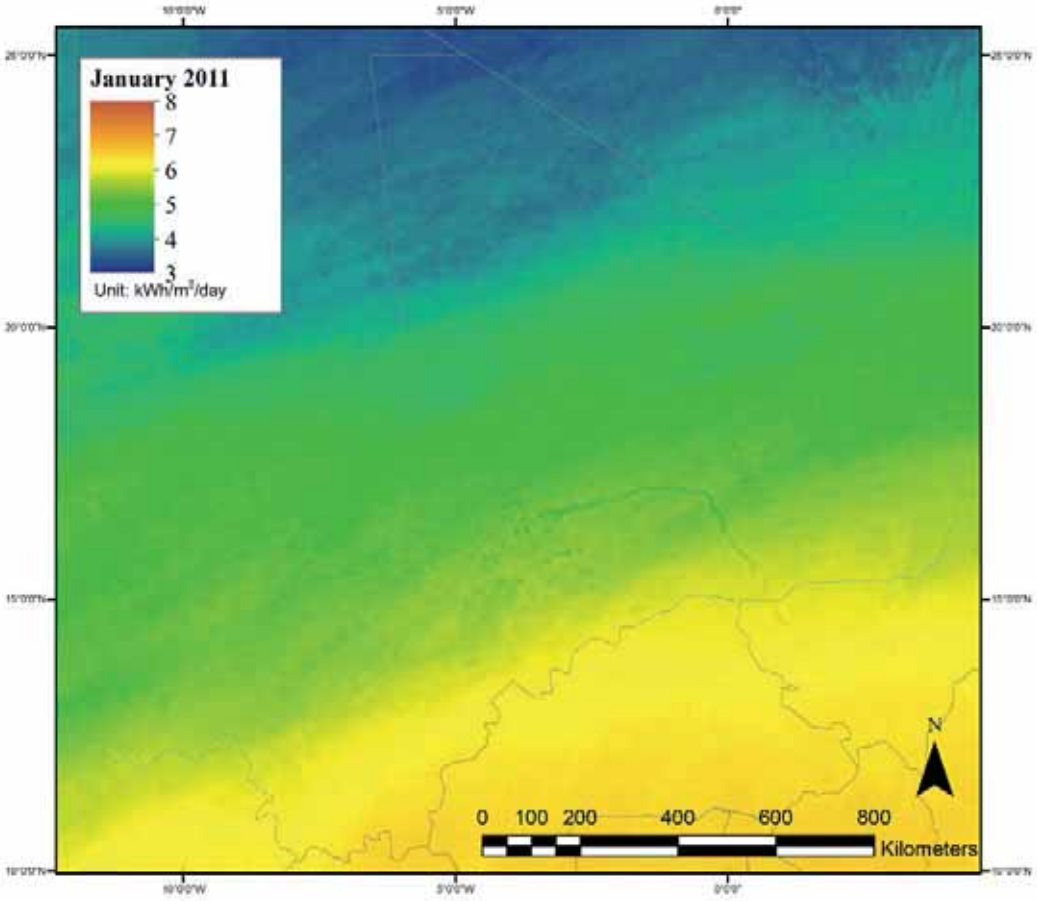
January 2011
8
7
6
5
4
3
Unit: kWh/m²/day
N
0 100 200 400 600 800
Kilometers

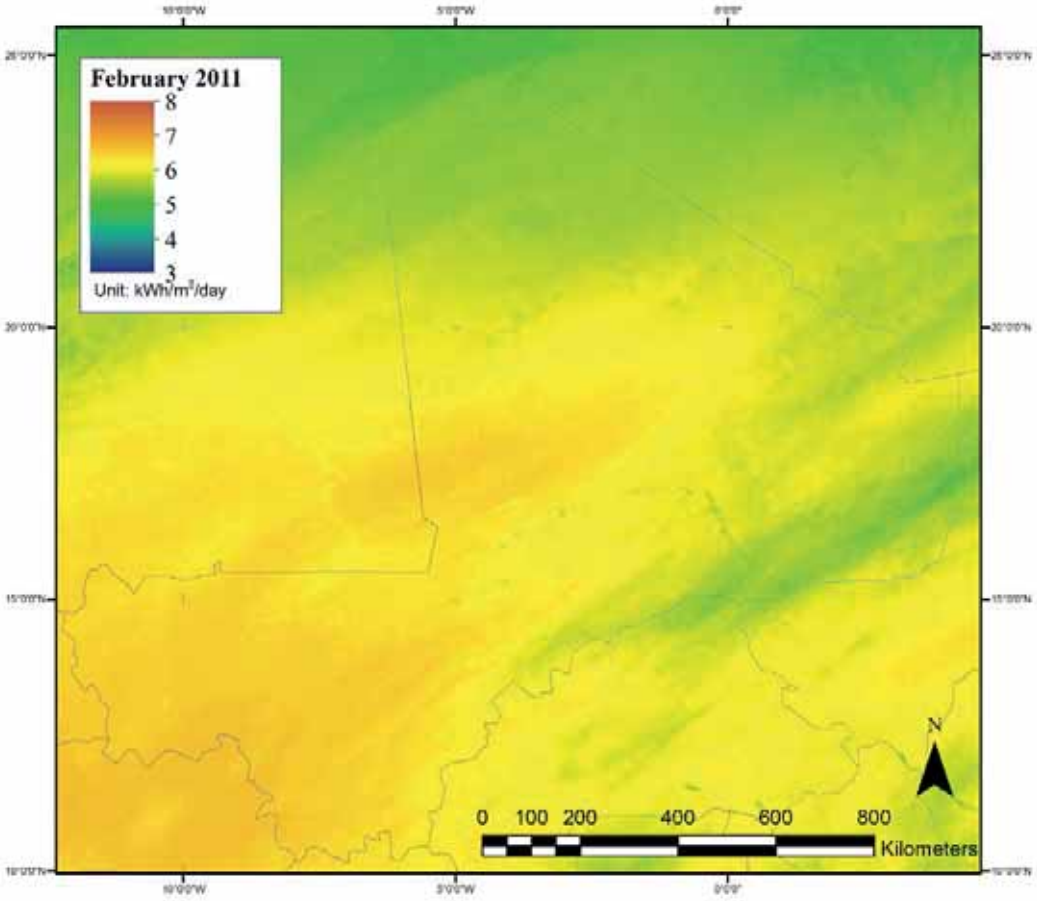
February 2011
8
7
6
5
4
3
Unit: kWh/m²/day
N
0 100 200 400 600 800
Kilometers

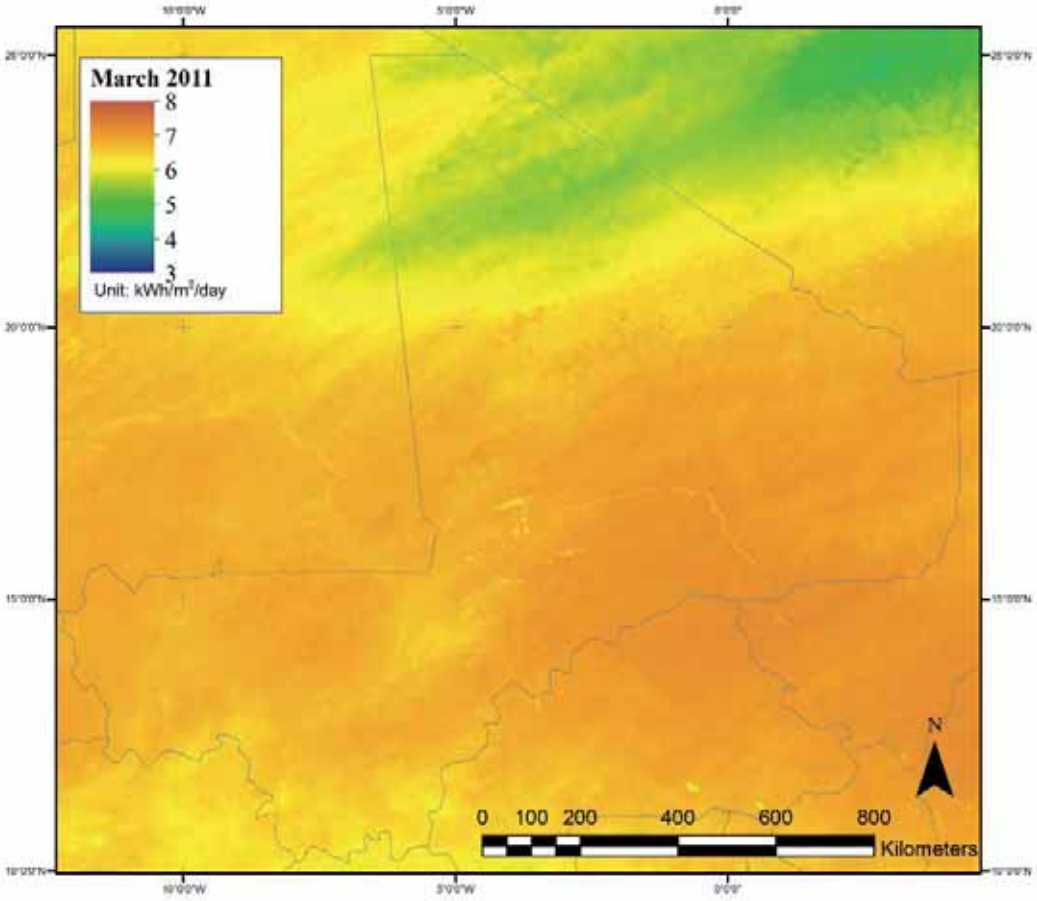
March 2011
8
7
6
5
4
3
Unit: kWh/m²/day
N
0 100 200 400 600 800
Kilometers

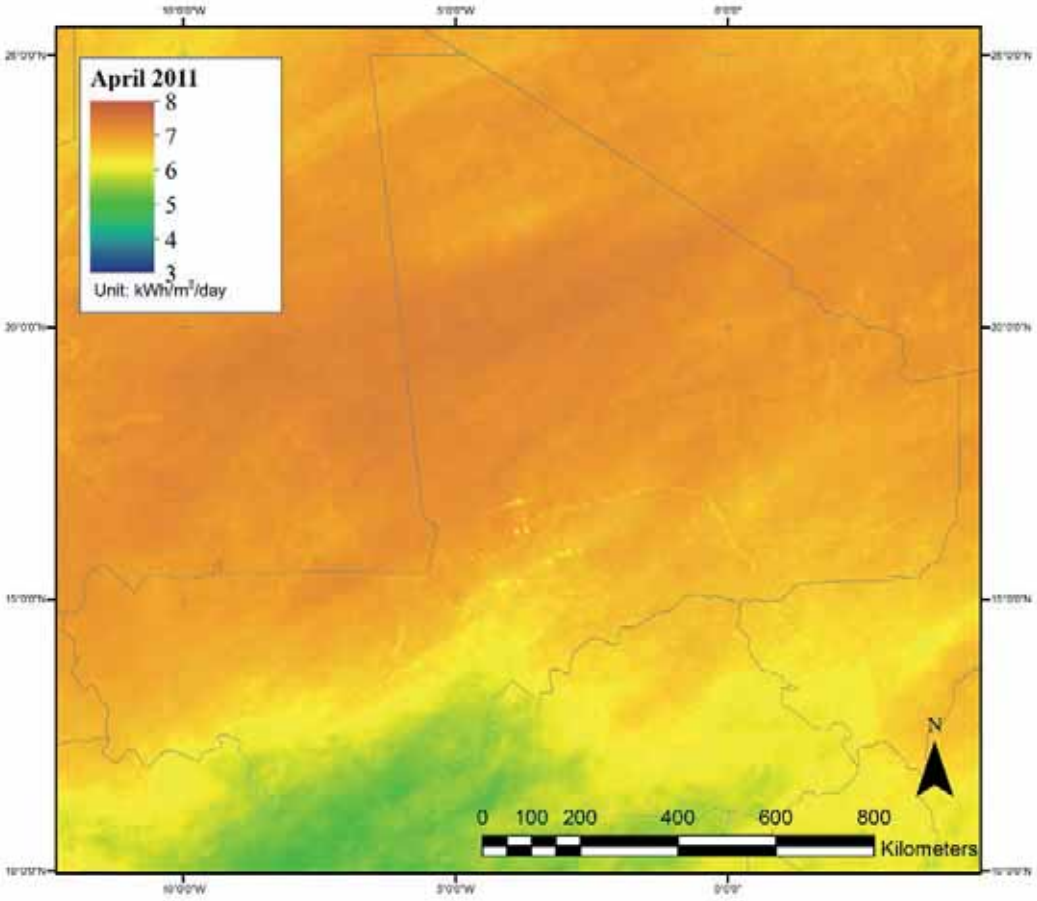
April 2011
8
7
6
5
4
3
Unit: kWh/m²/day
N
0 100 200 400 600 800
Kilometers

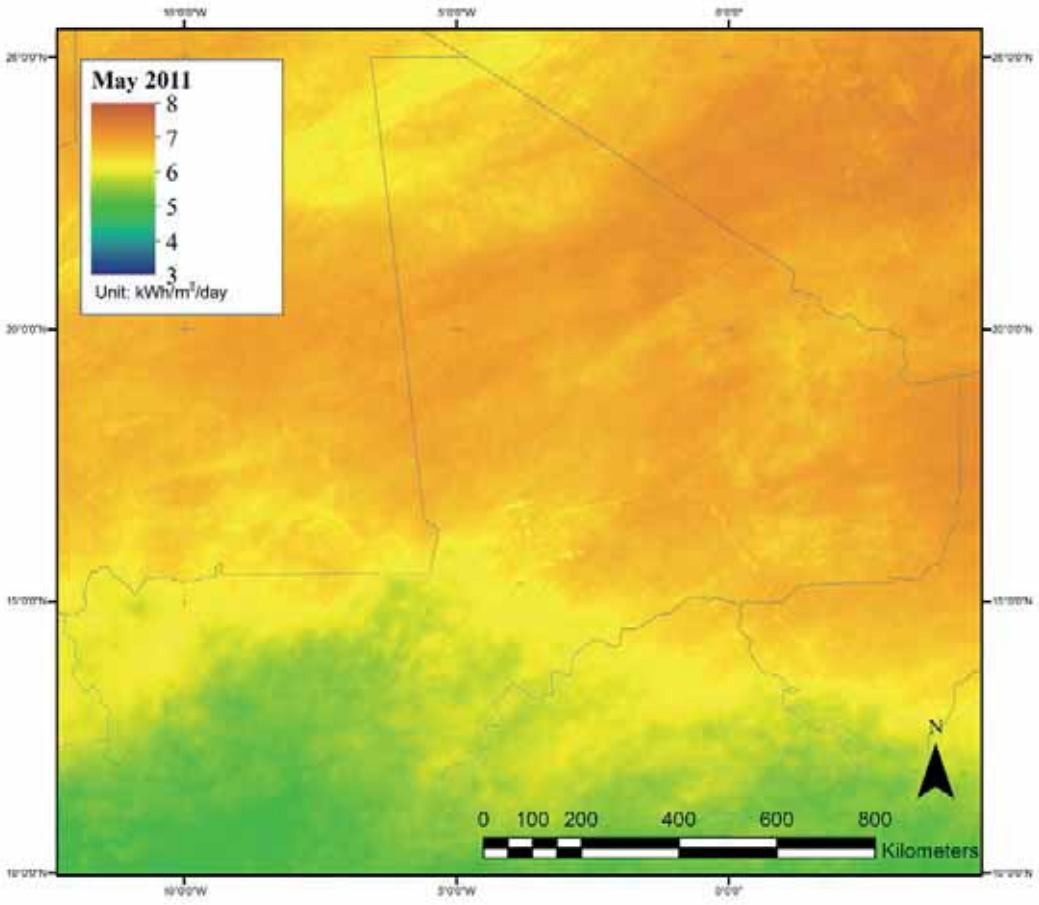
May 2011
8
7
6
5
4
3
Unit: kWh/m²/day
N
0 100 200 400 600 800
Kilometers

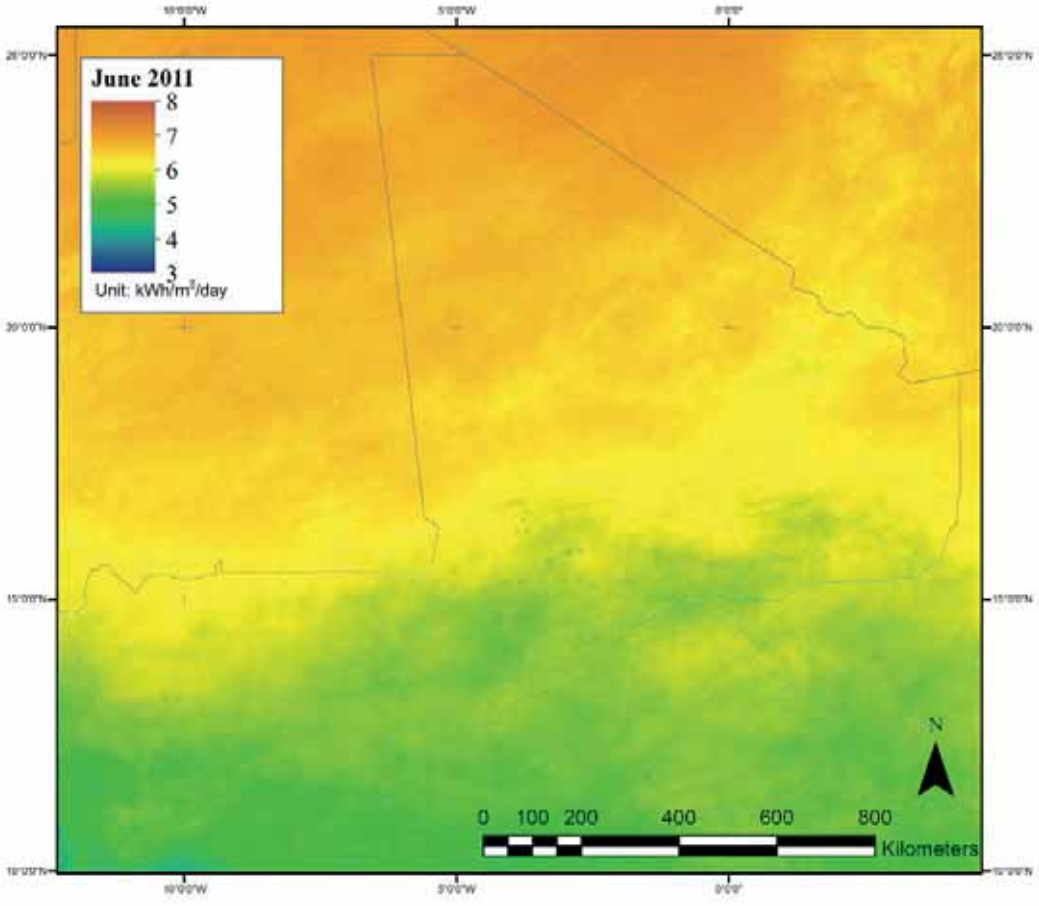
June 2011
8
7
6
5
4
3
Unit: kWh/m²/day
N
0 100 200 400 600 800
Kilometers

4 Monthly daily average in kWh/m^2/day, averaged for the three years covered in this study.

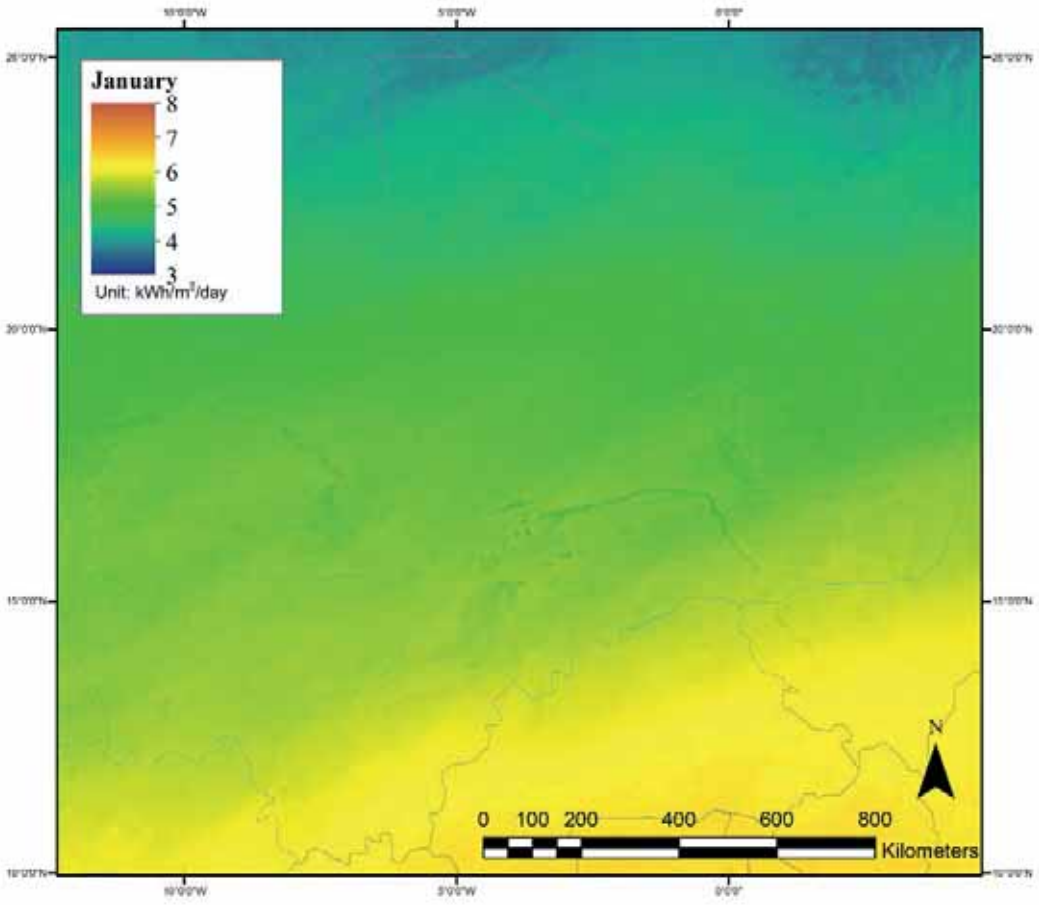
January
8
7
6
5
4
3
Unit: kWh/m²/day
N
0 100 200 400 600 800
Kilometers

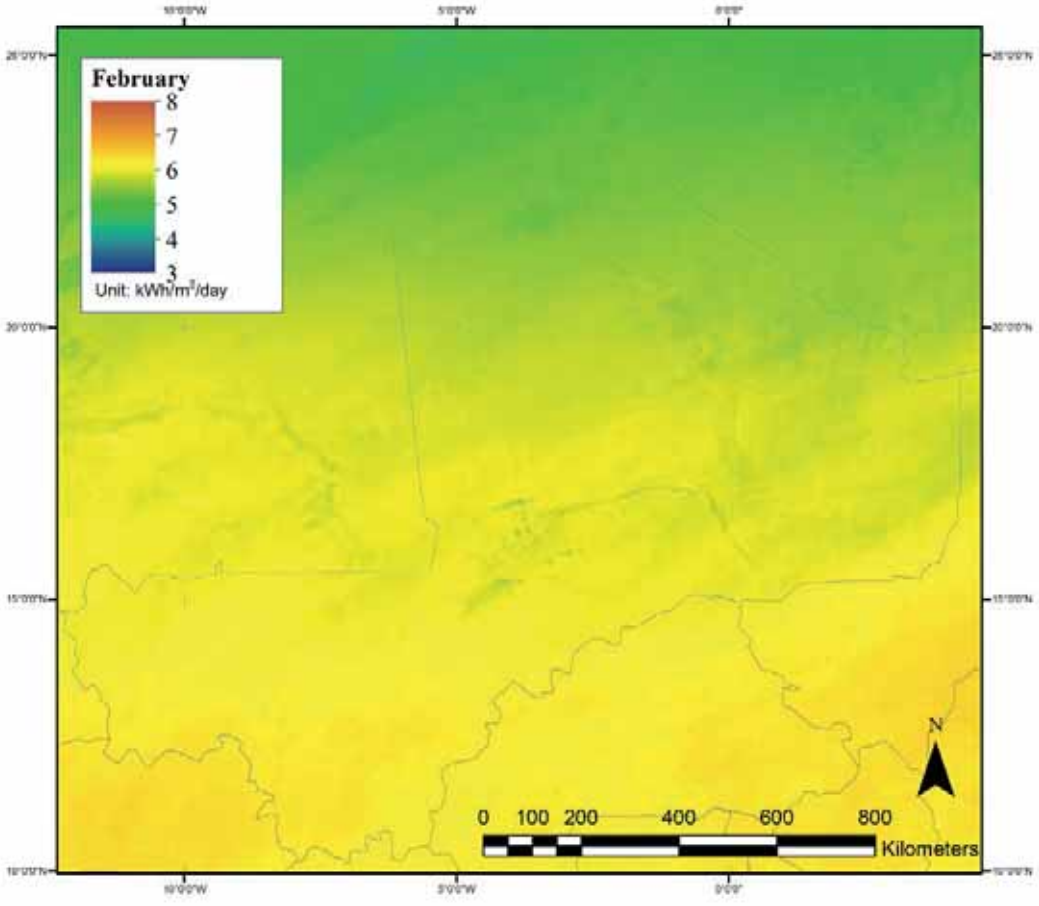
February
8
7
6
5
4
3
Unit: kWh/m²/day
N
0 100 200 400 600 800
Kilometers

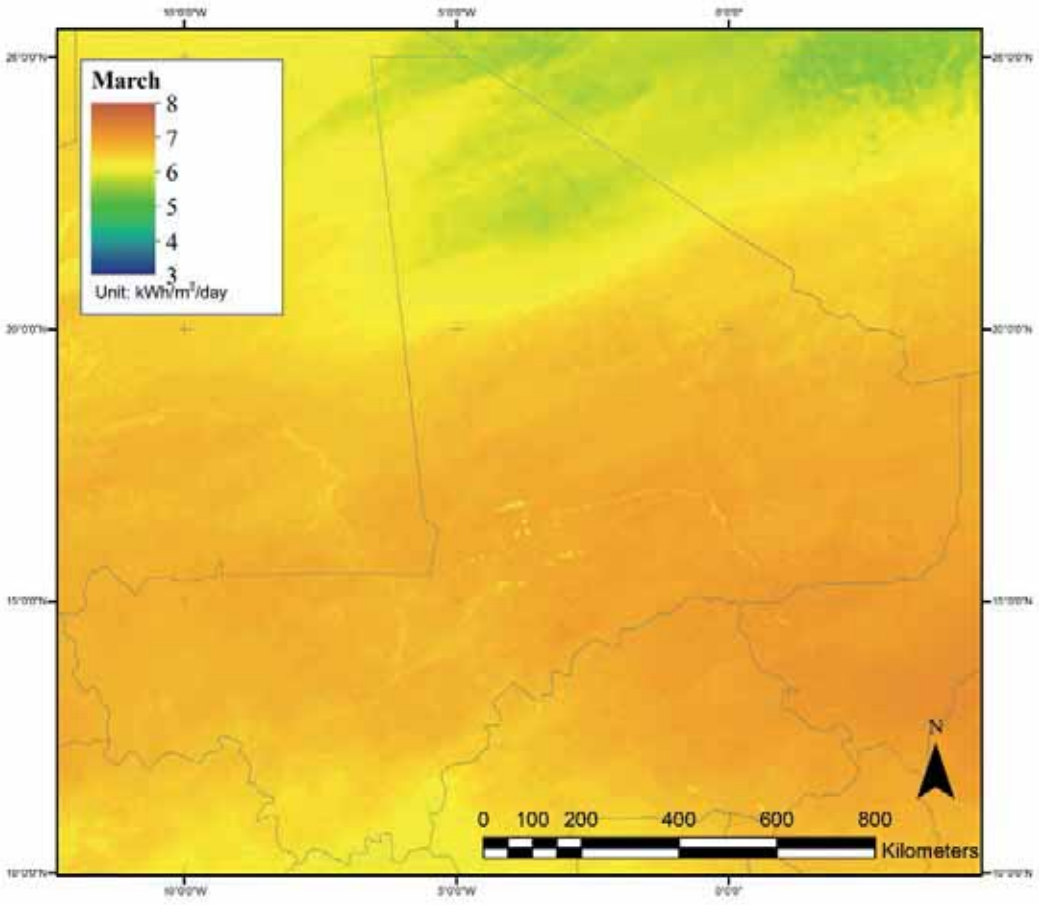
March
8
7
6
5
4
3
Unit: kWh/m²/day
N
0 100 200 400 600 800
Kilometers

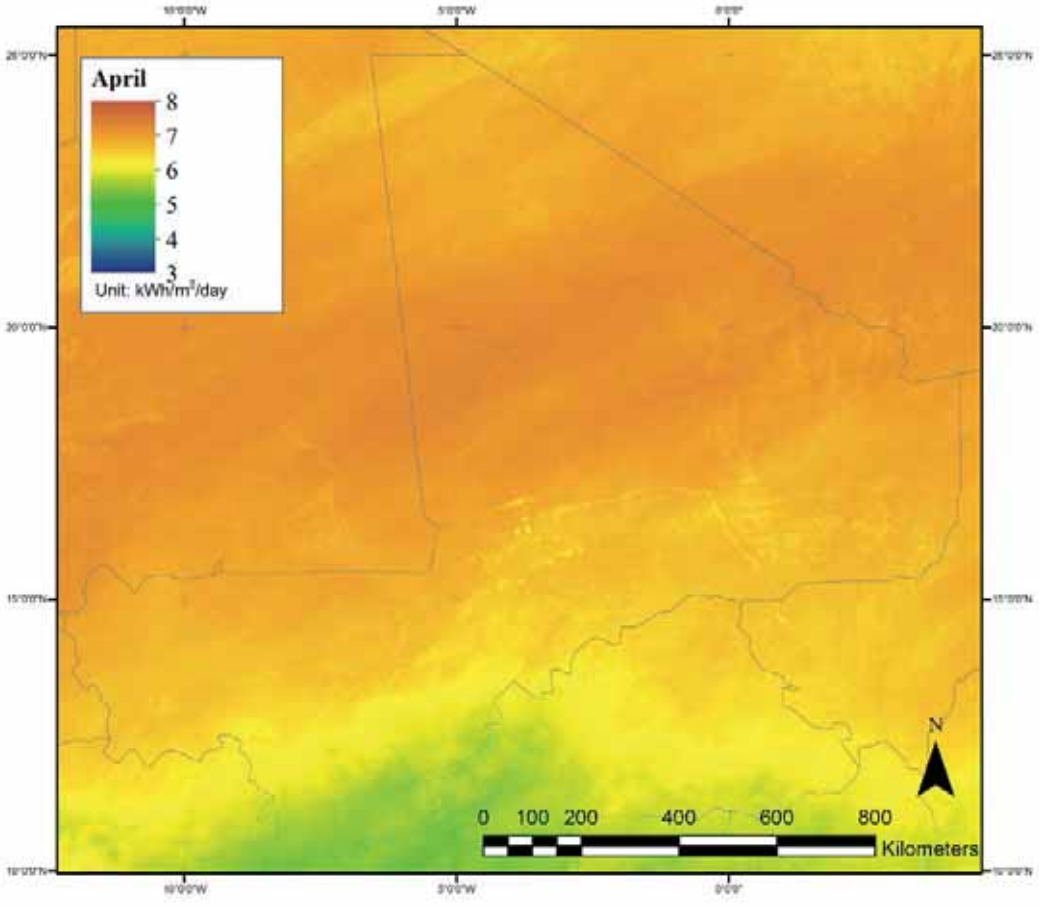
April
8
7
6
5
4
3
Unit: kWh/m²/day
N
0 100 200 400 600 800
Kilometers

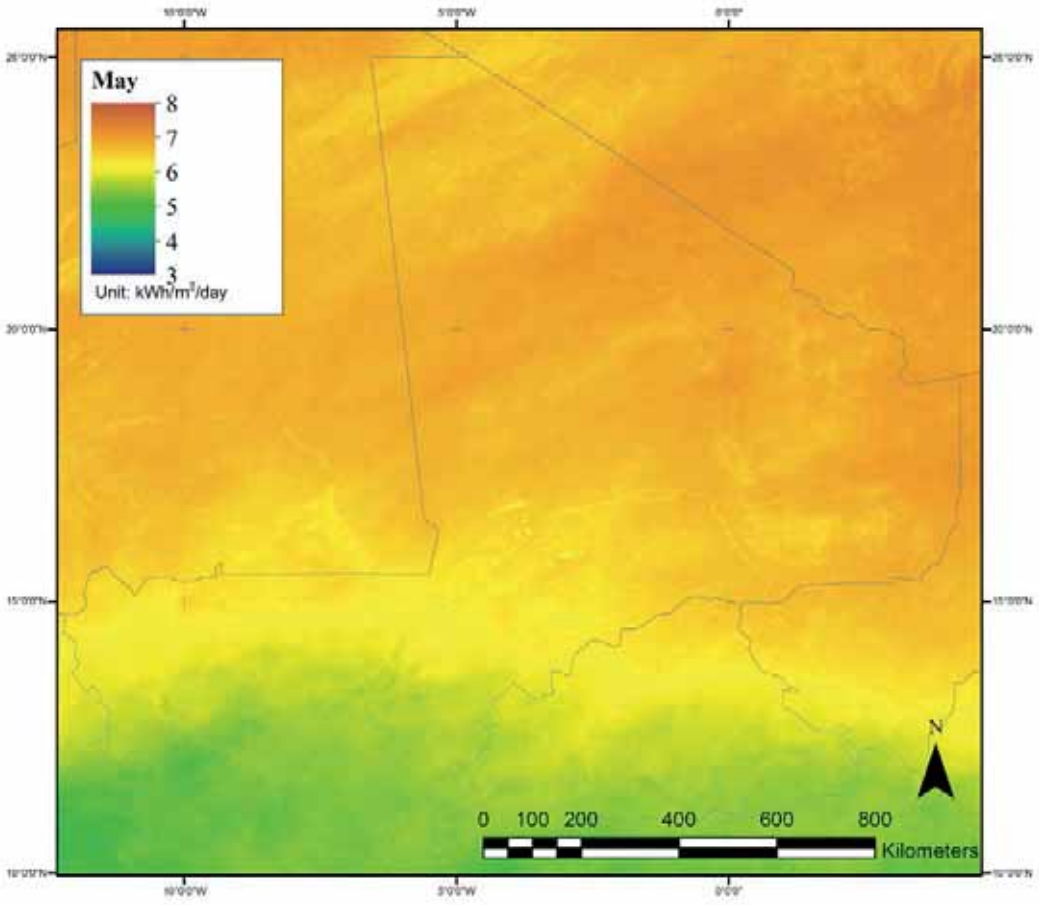
May
8
7
6
5
4
3
Unit: kWh/m²/day
N
0 100 200 400 600 800
Kilometers

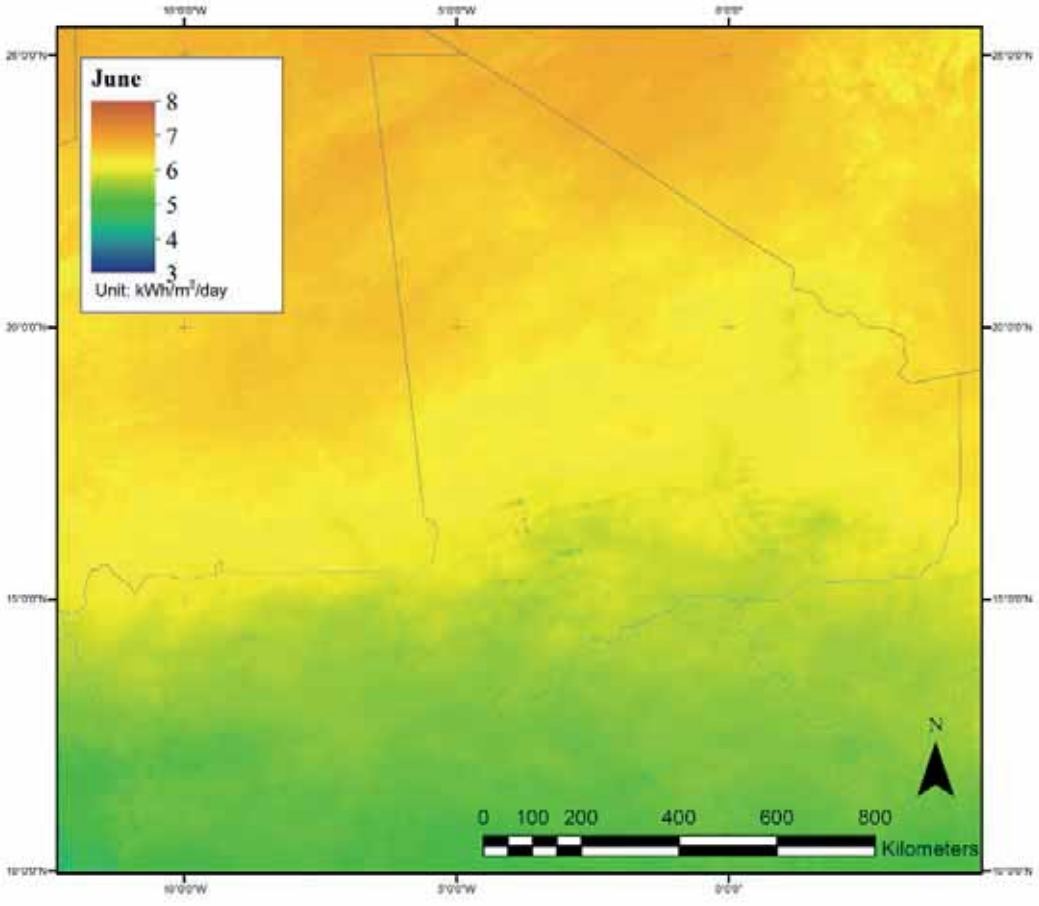
June
8
7
6
5
4
3
Unit: kWh/m²/day
N
0 100 200 400 600 800
Kilometers

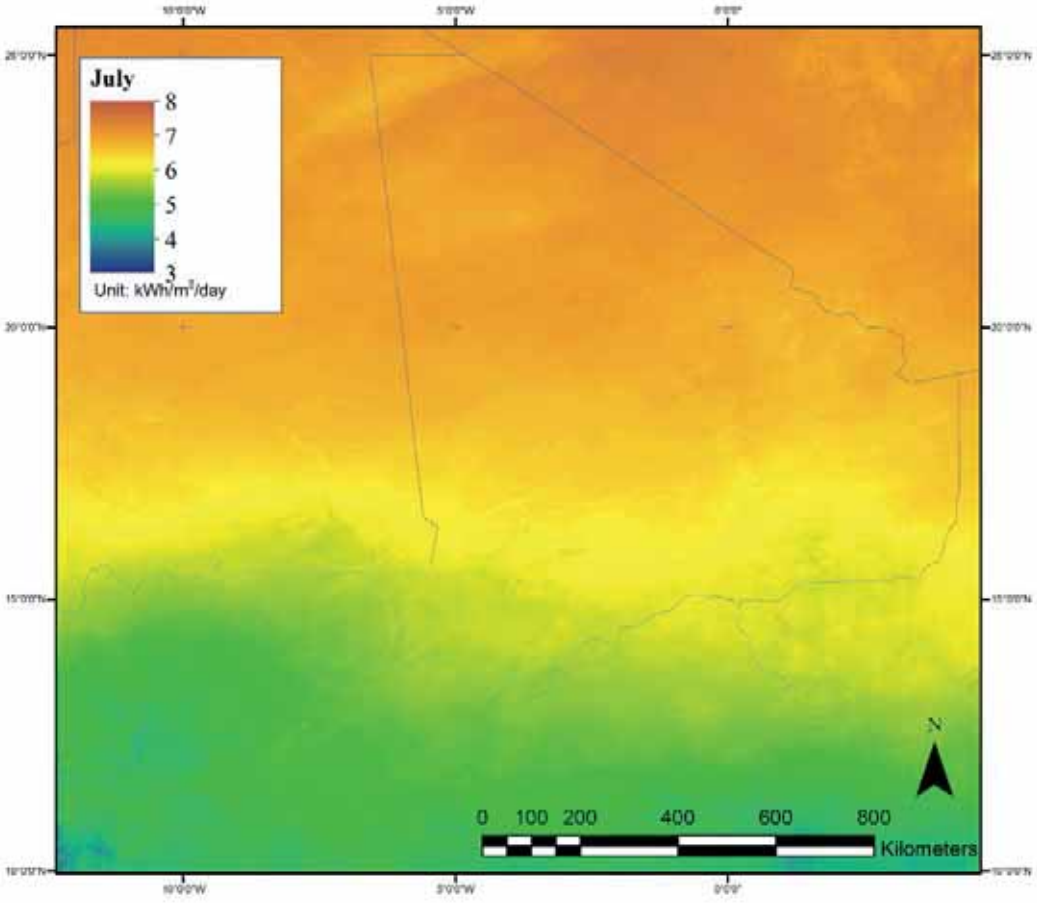
July
8
7
6
5
4
3
Unit: kWh/m²/day
N
0 100 200 400 600 800
Kilometers

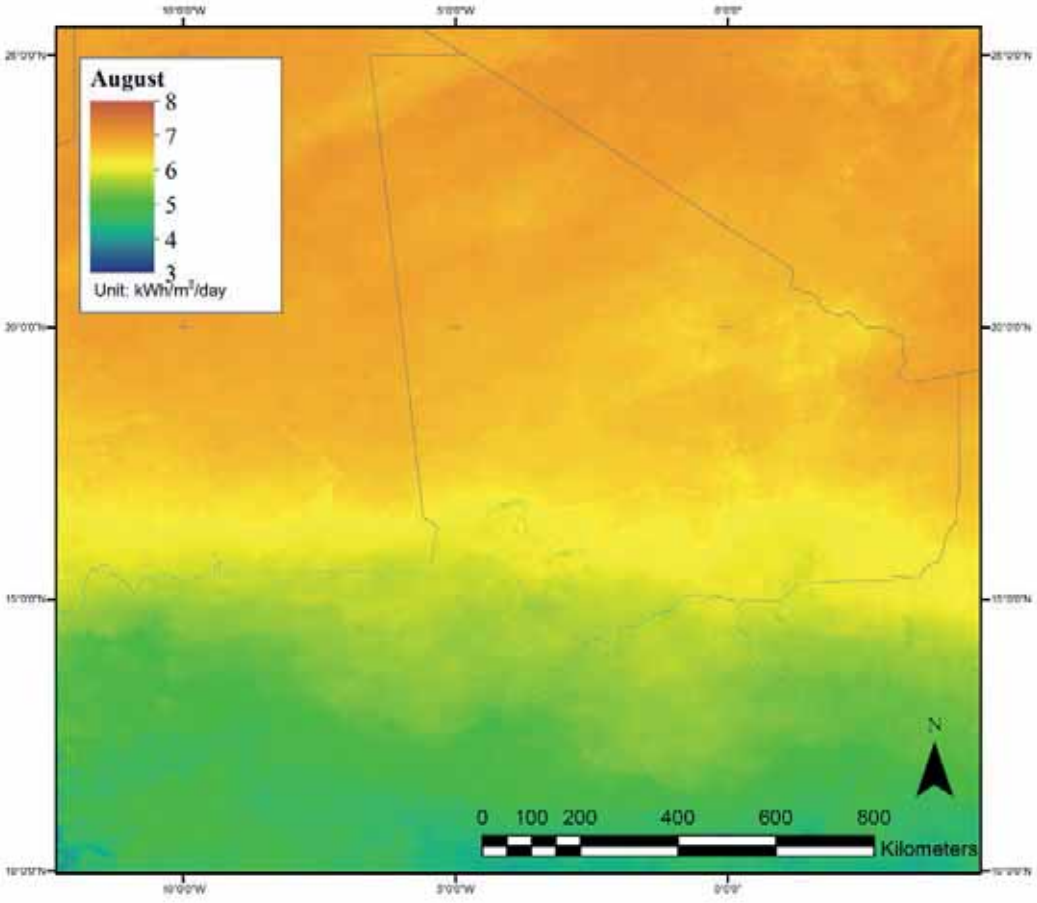
August
8
7
6
5
4
3
Unit: kWh/m²/day
N
0 100 200 400 600 800
Kilometers

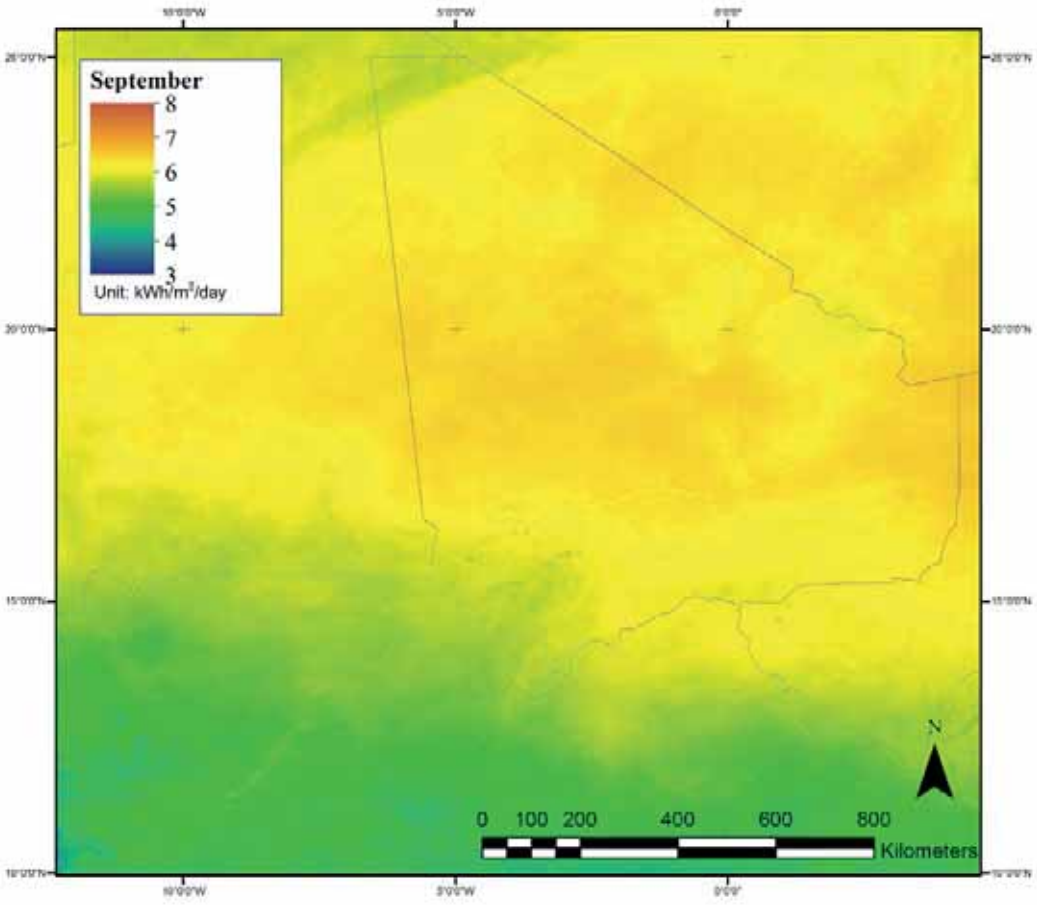
September
8
7
6
5
4
3
Unit: kWh/m²/day
N
0 100 200 400 600 800
Kilometers

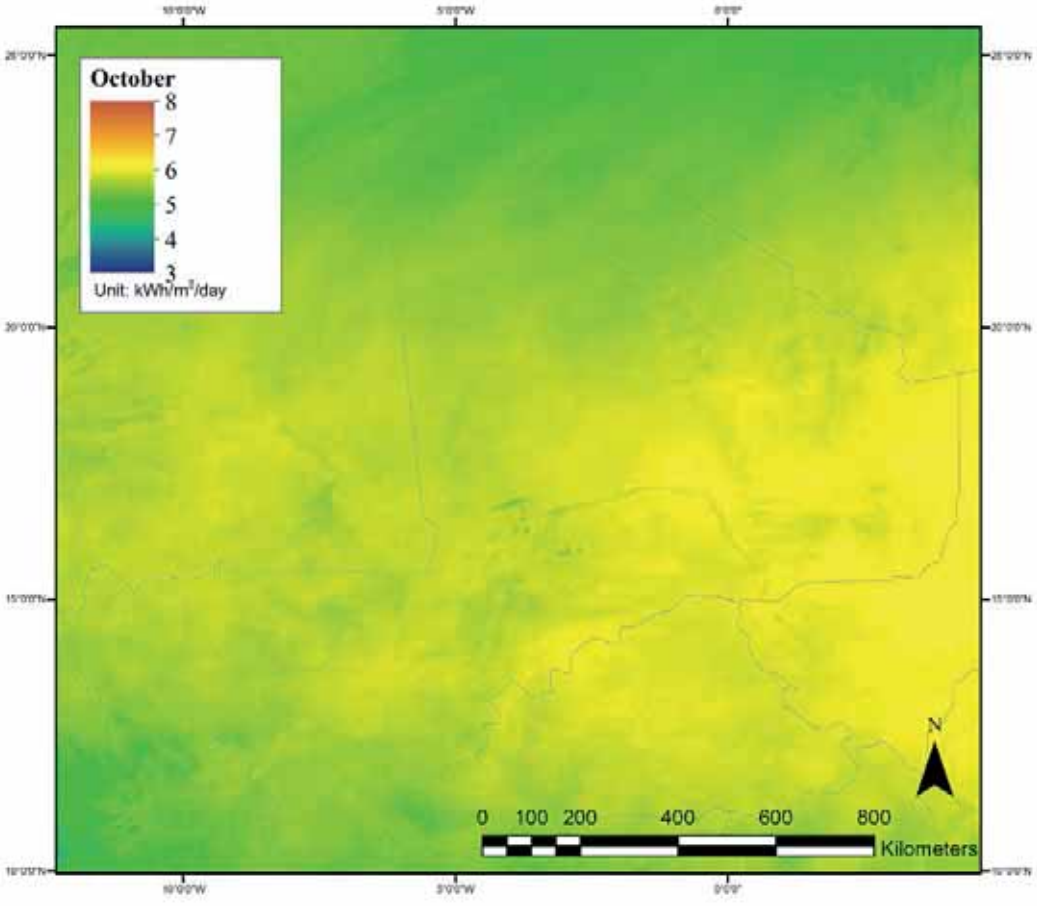
October
8
7
6
5
4
3
Unit: kWh/m²/day
N
0 100 200 400 600 800
Kilometers

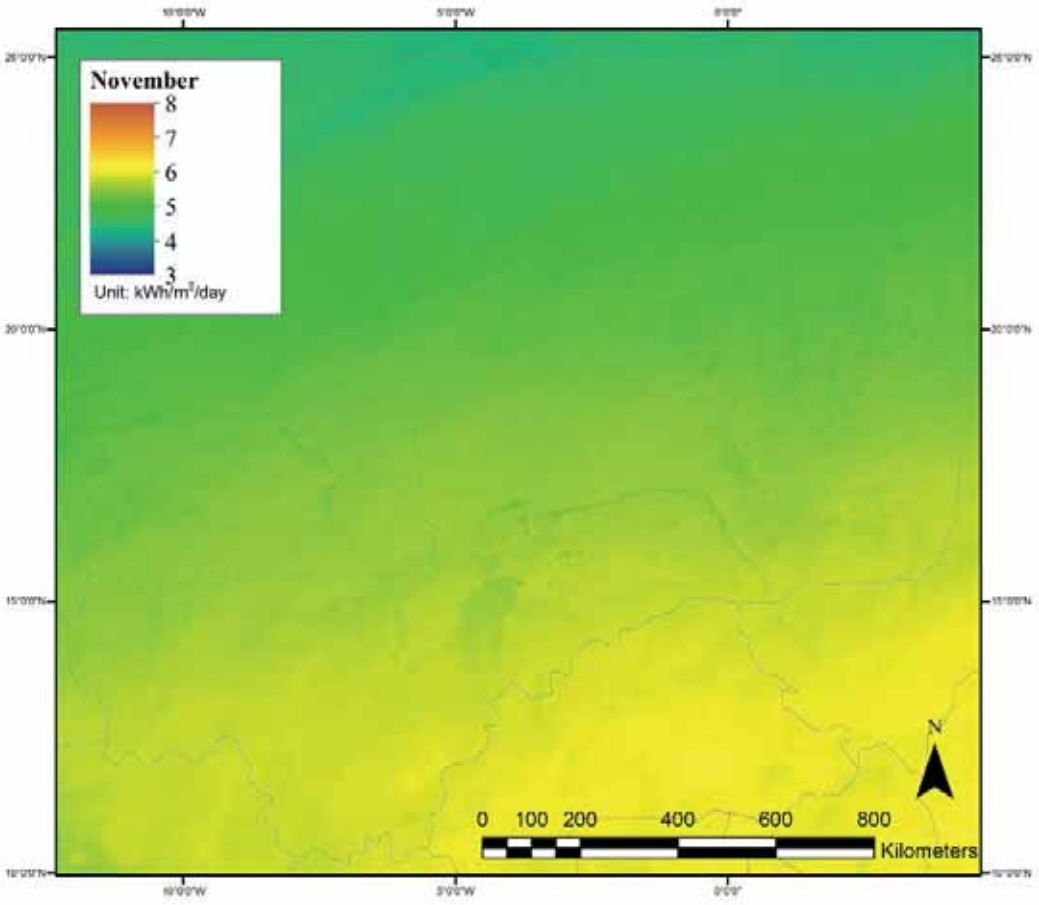
November
8
7
6
5
4
3
Unit: kWh/m²/day
N
0 100 200 400 600 800
Kilometers

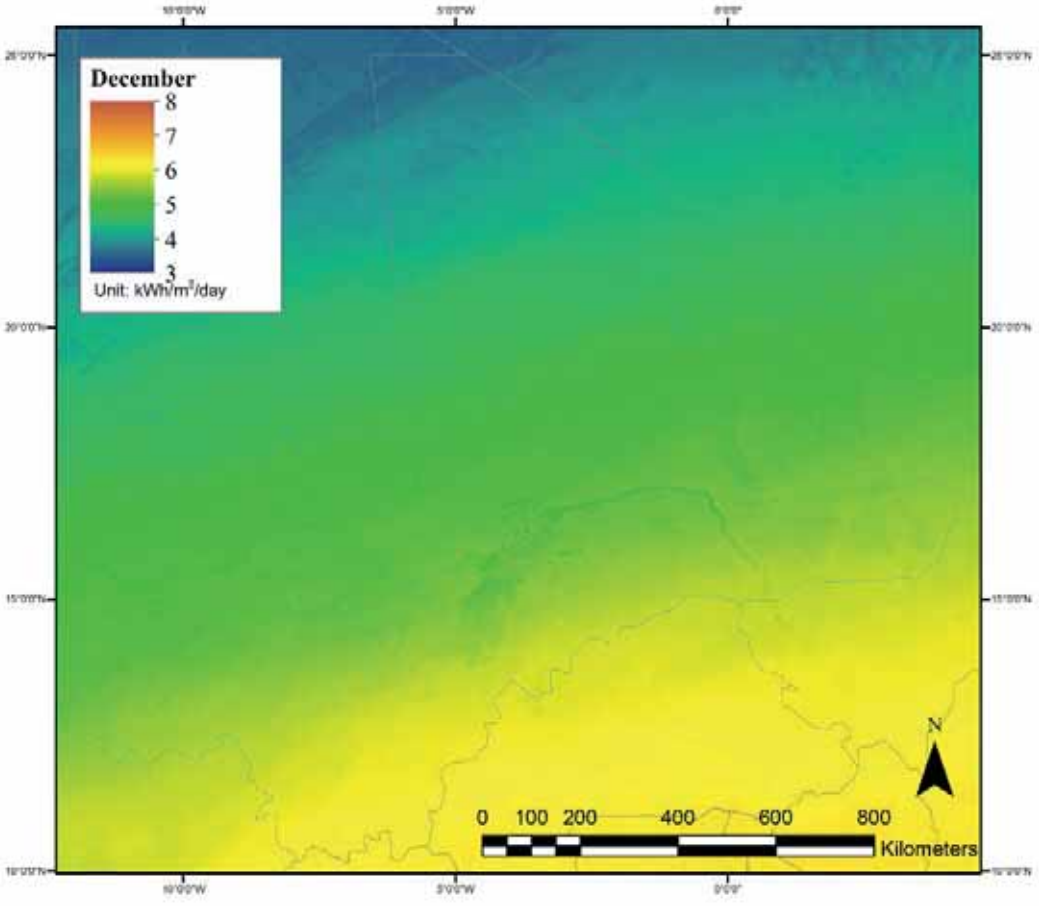
December
8
7
6
5
4
3
Unit: kWh/m²/day
N
0 100 200 400 600 800
Kilometers

5 Monthly daily average in kWh/m^2/day, 1 degree resolution averaged for the three years covered in this study

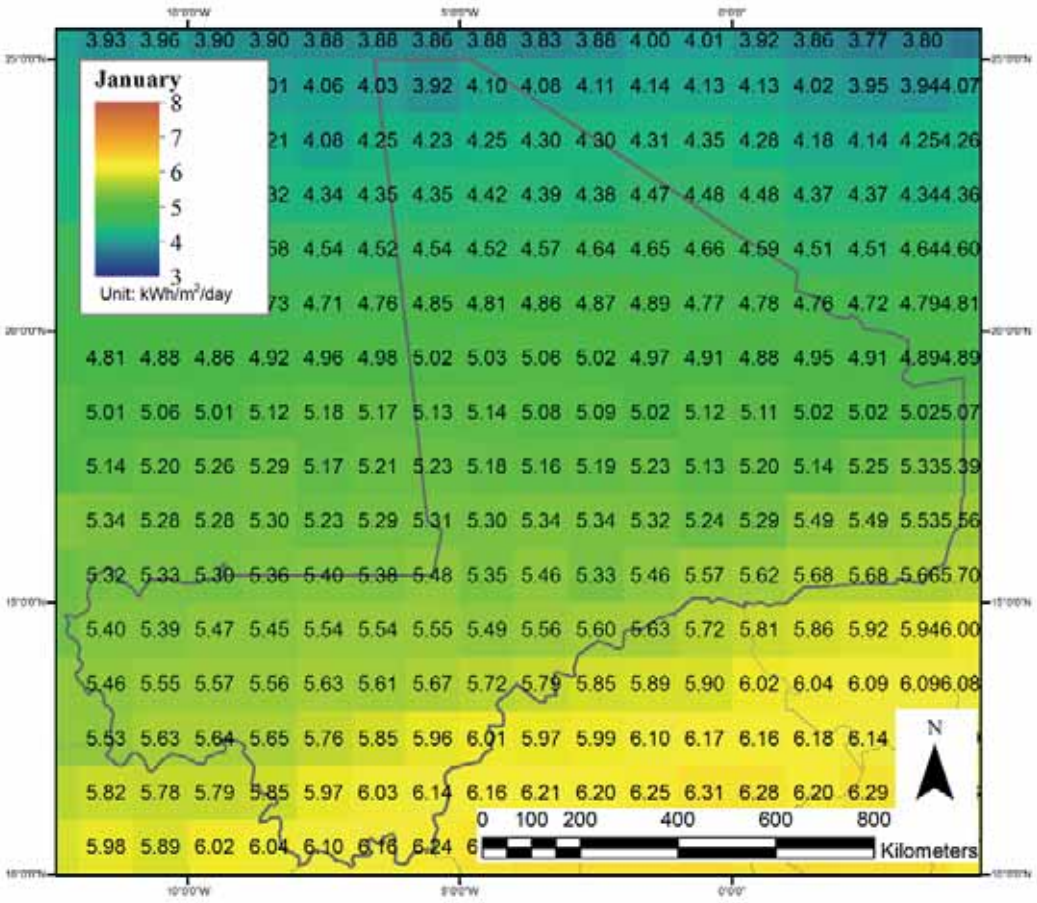
January
8
7
6
5
4
3
Unit: kWh/m²/day
N
0 100 200 400 600 800
Kilometers

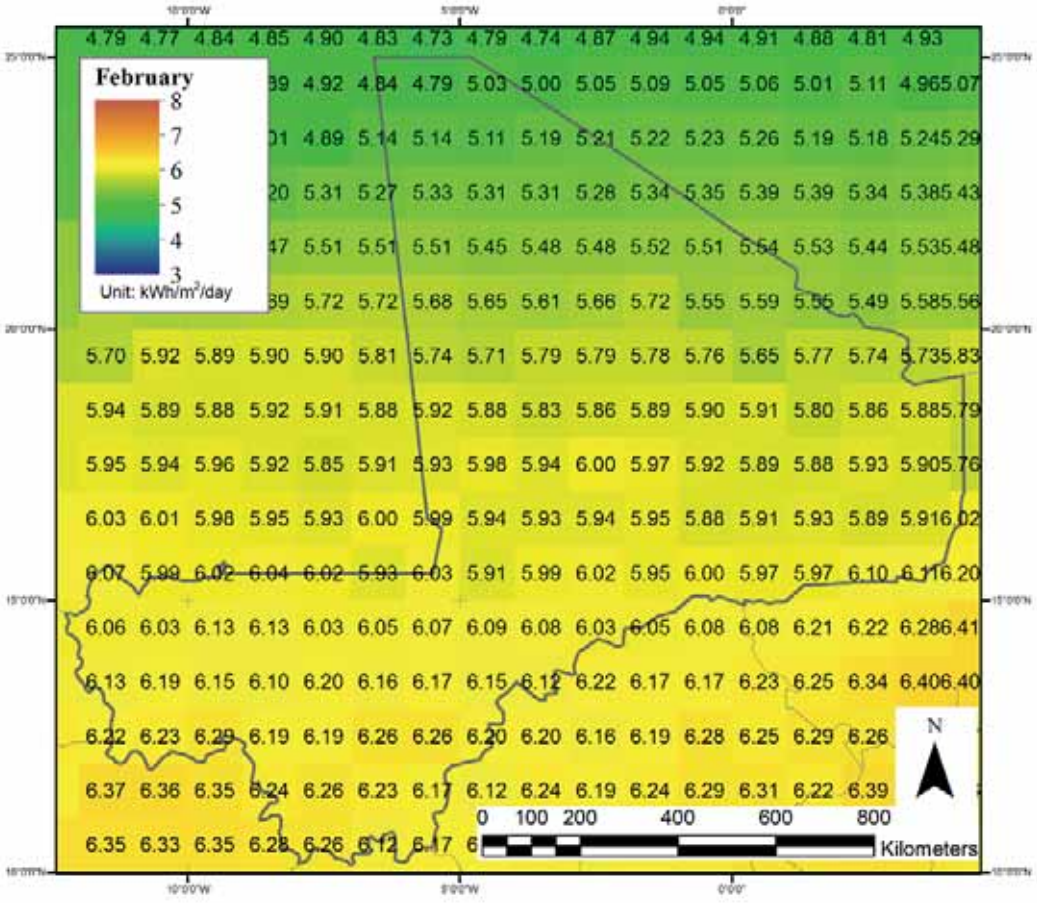
February
8
7
6
5
4
3
Unit: kWh/m²/day
N
0 100 200 400 600 800
Kilometers

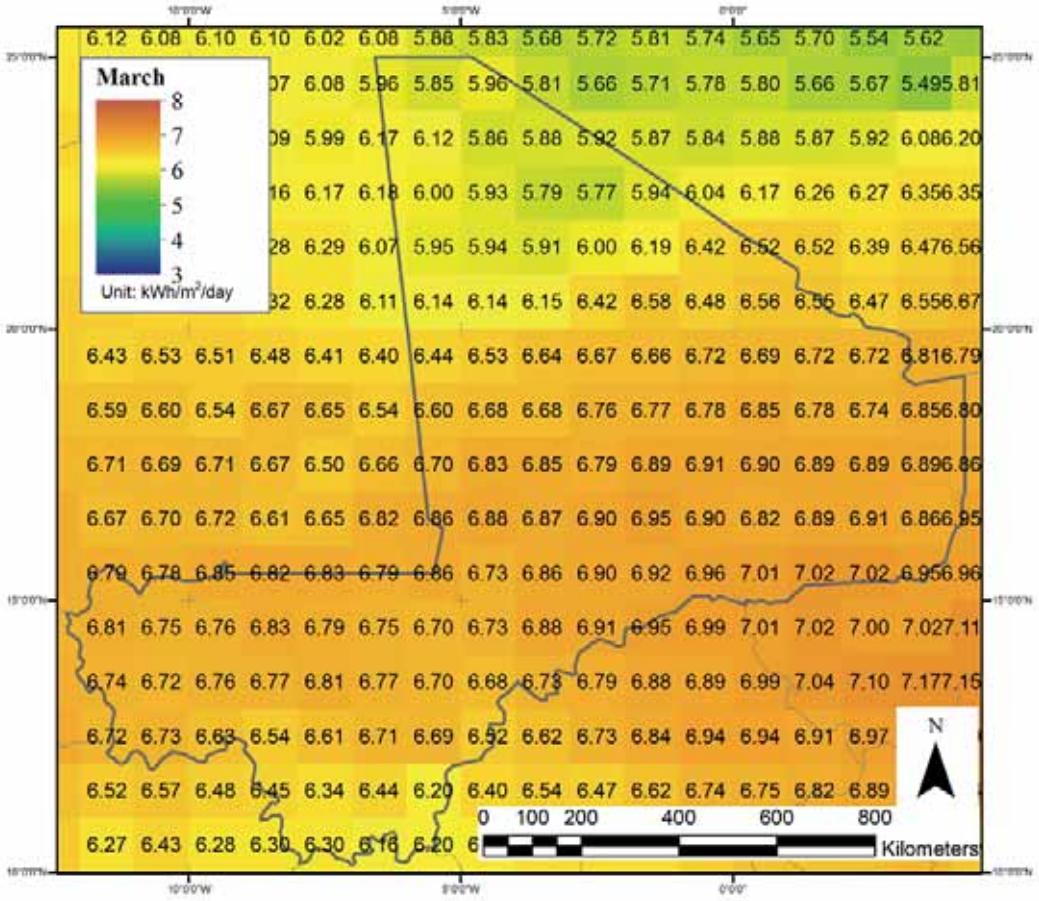
March
8
7
6
5
4
3
Unit: kWh/m²/day
N
0 100 200 400 600 800
Kilometers

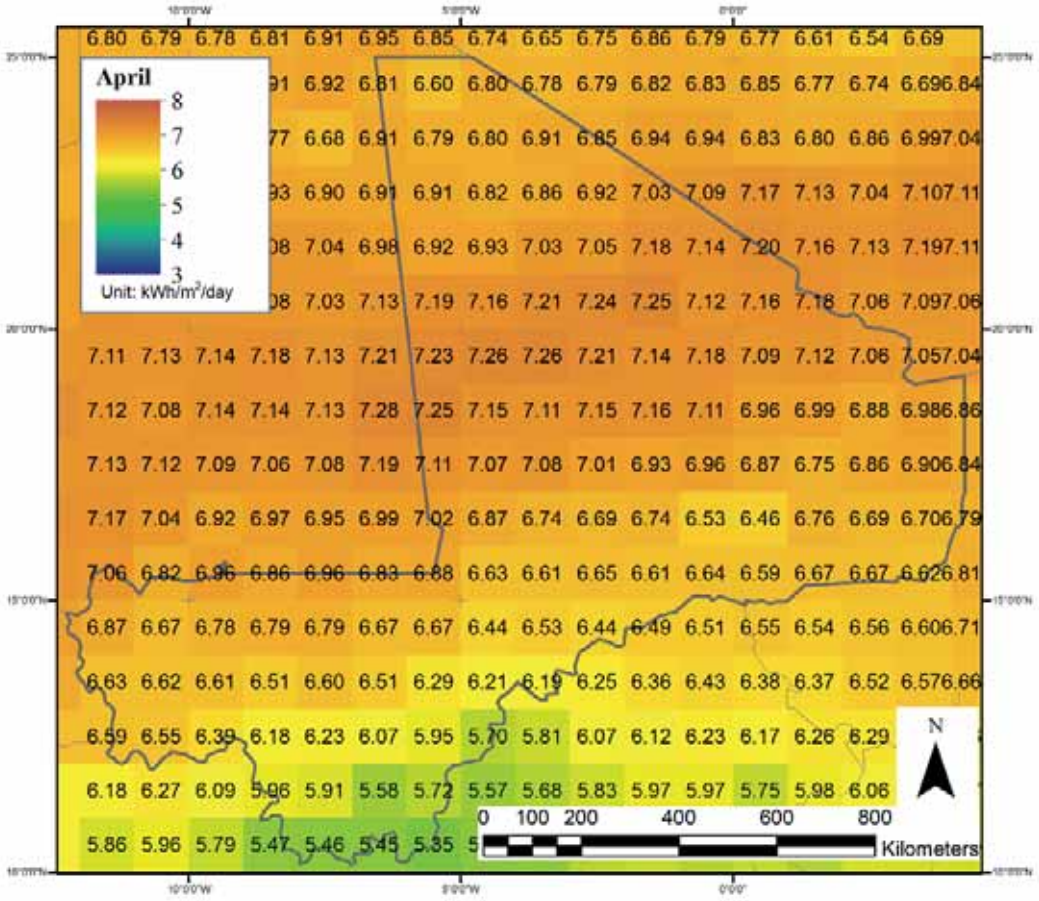
April
8
7
6
5
4
3
Unit: kWh/m²/day
N
0 100 200 400 600 800
Kilometers

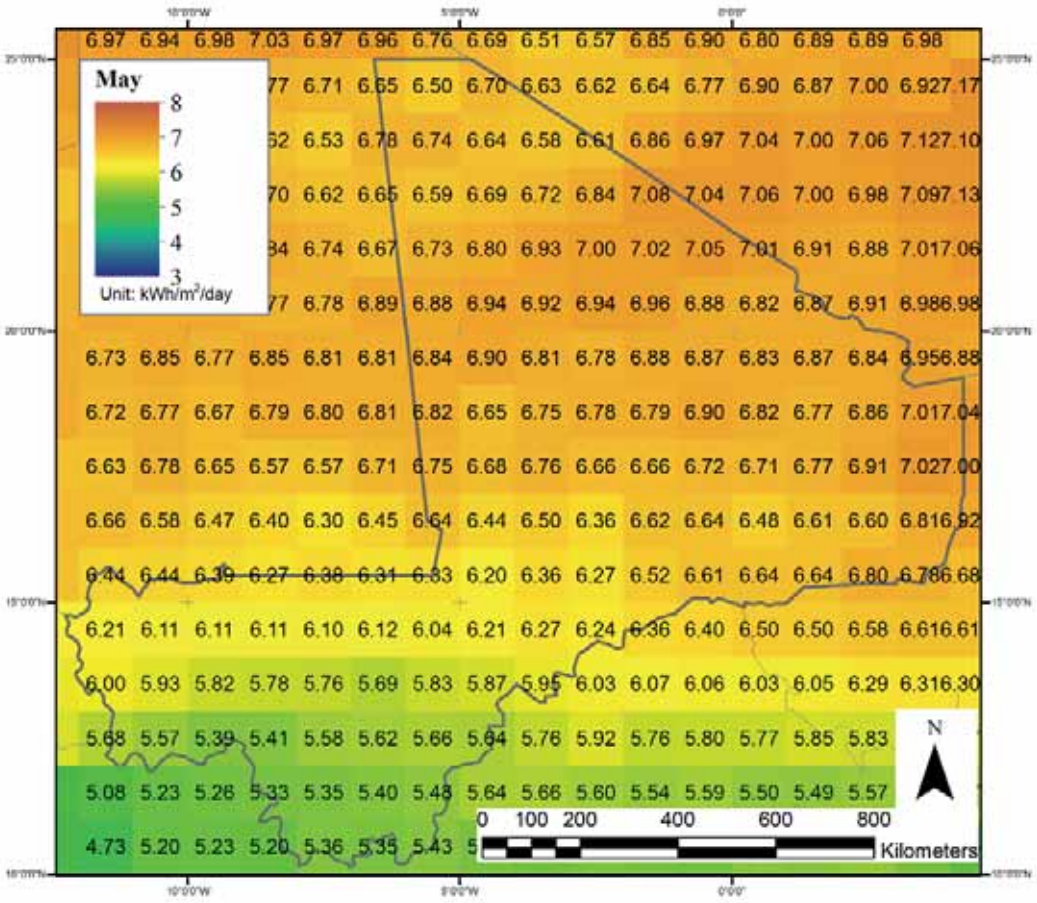
May
8
7
6
5
4
3
Unit: kWh/m²/day
N
0 100 200 400 600 800
Kilometers

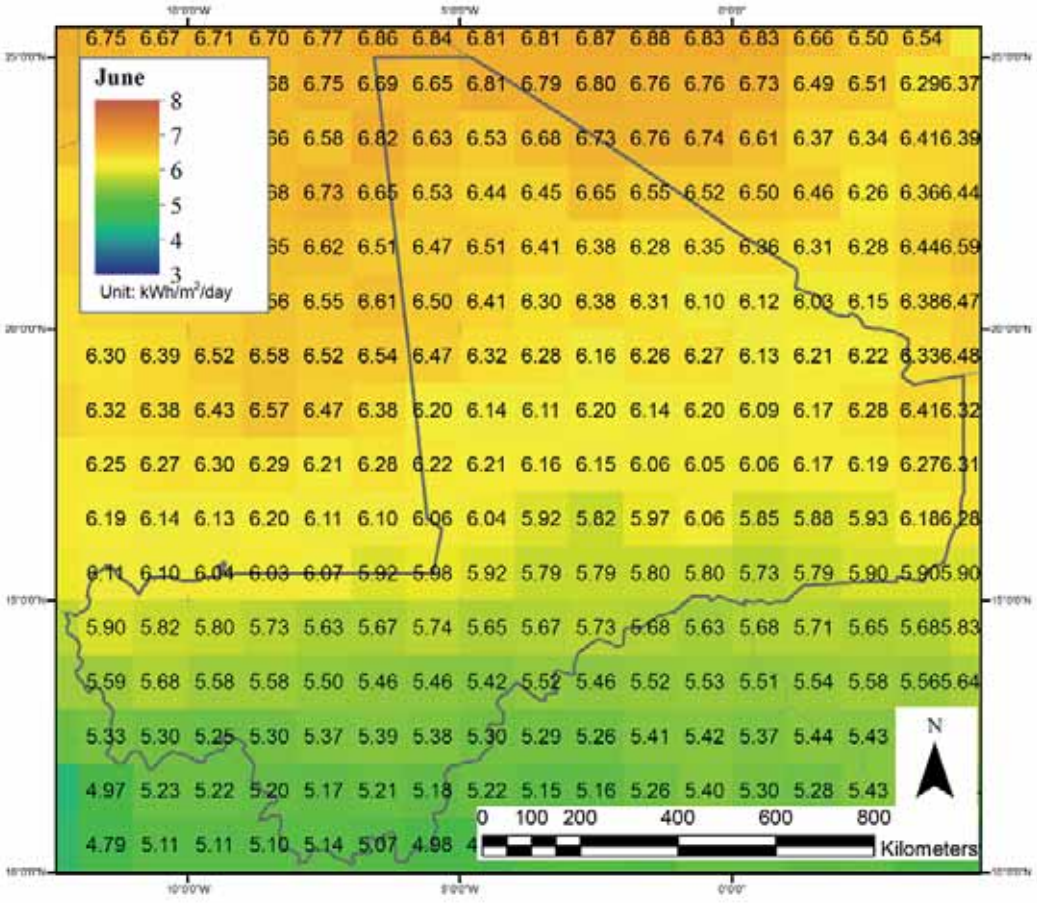
June
8
7
6
5
4
3
Unit: kWh/m²/day
N
0 100 200 400 600 800
Kilometers

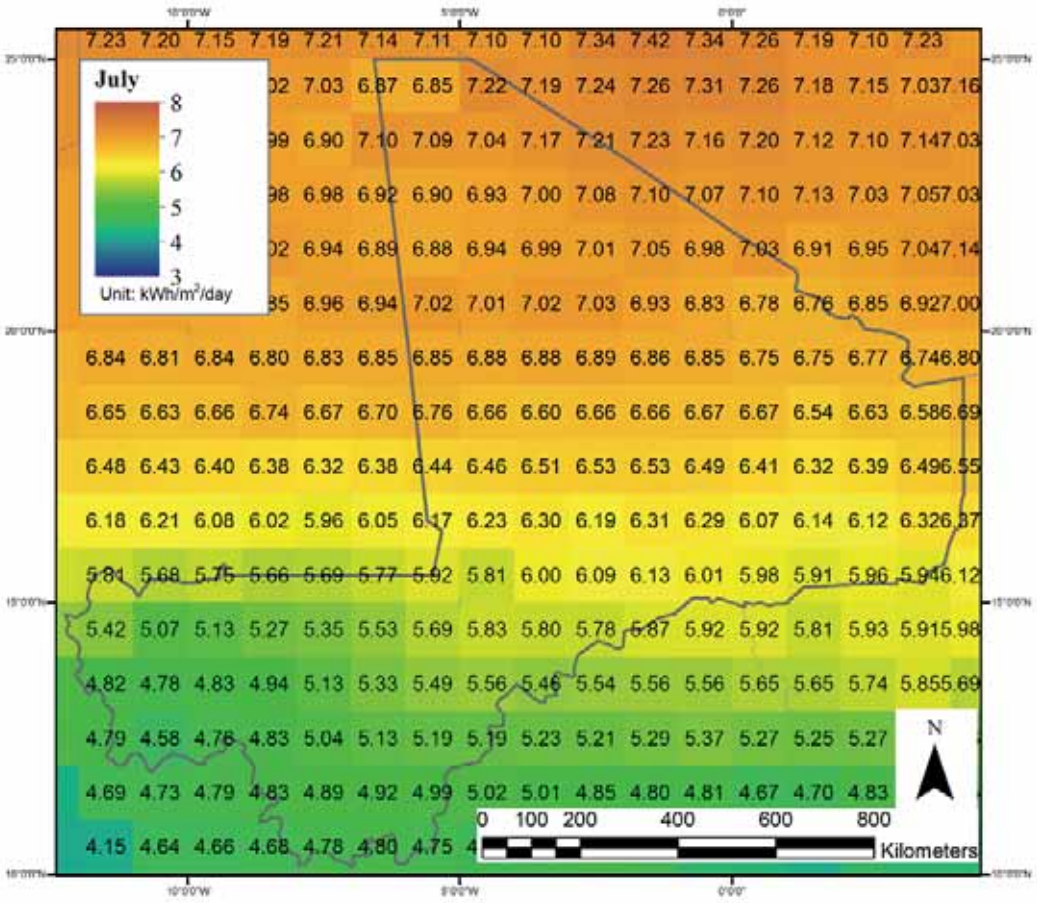
July
8
7
6
5
4
3
Unit: kWh/m²/day
N
0 100 200 400 600 800
Kilometers

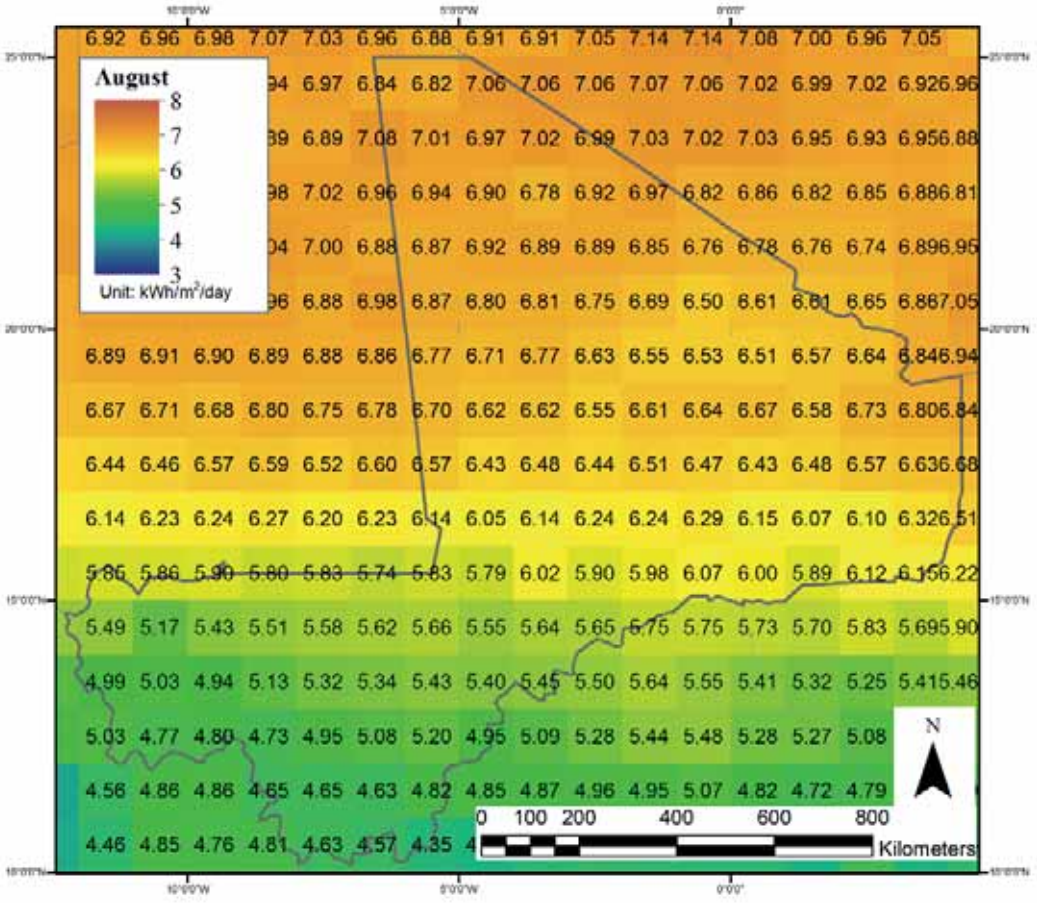
August
8
7
6
5
4
3
Unit: kWh/m²/day
N
0 100 200 400 600 800
Kilometers

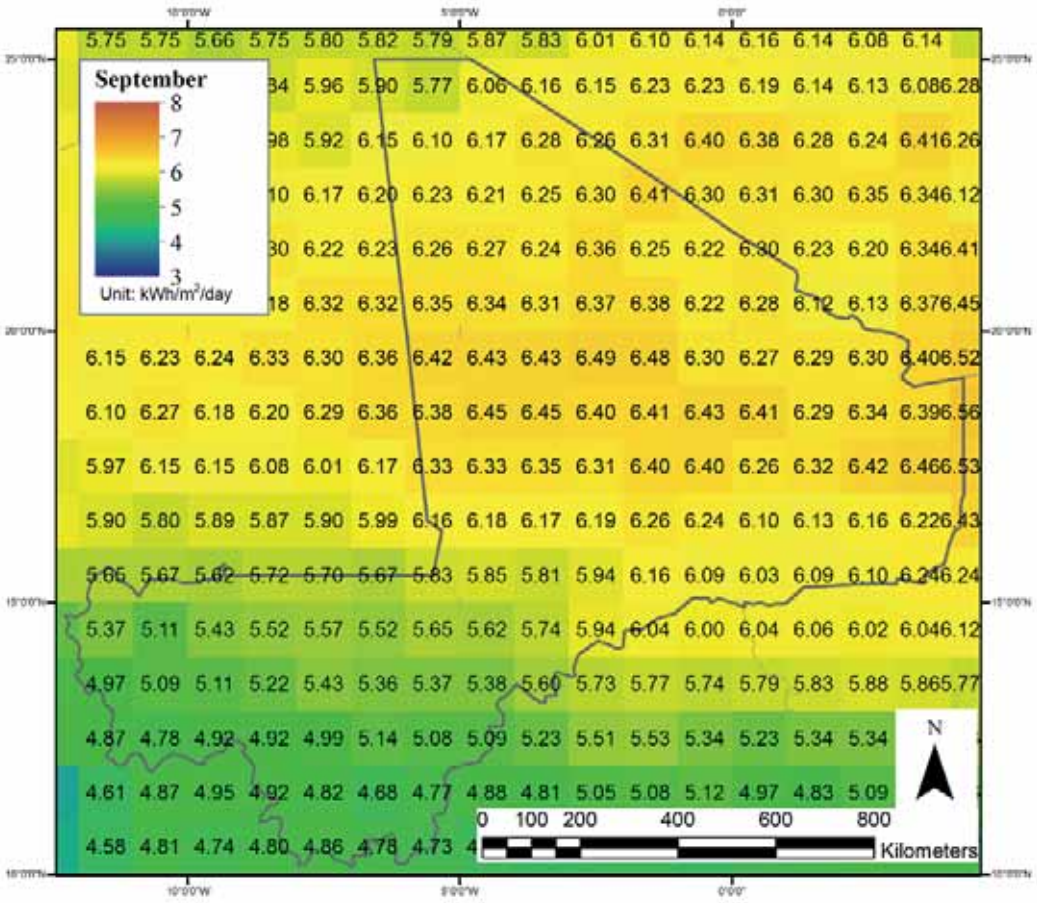
September
8
7
6
5
4
3
Unit: kWh/m²/day
N
0 100 200 400 600 800
Kilometers

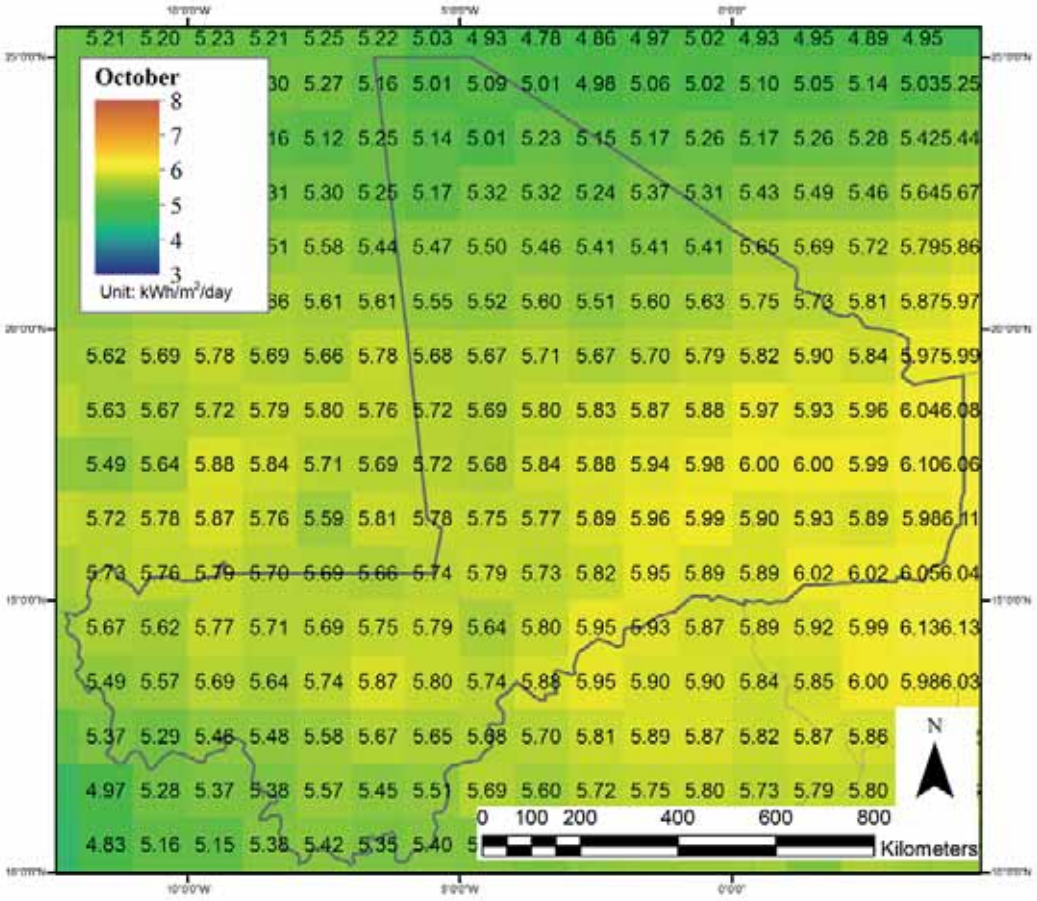
October
8
7
6
5
4
3
Unit: kWh/m²/day
N
0 100 200 400 600 800
Kilometers

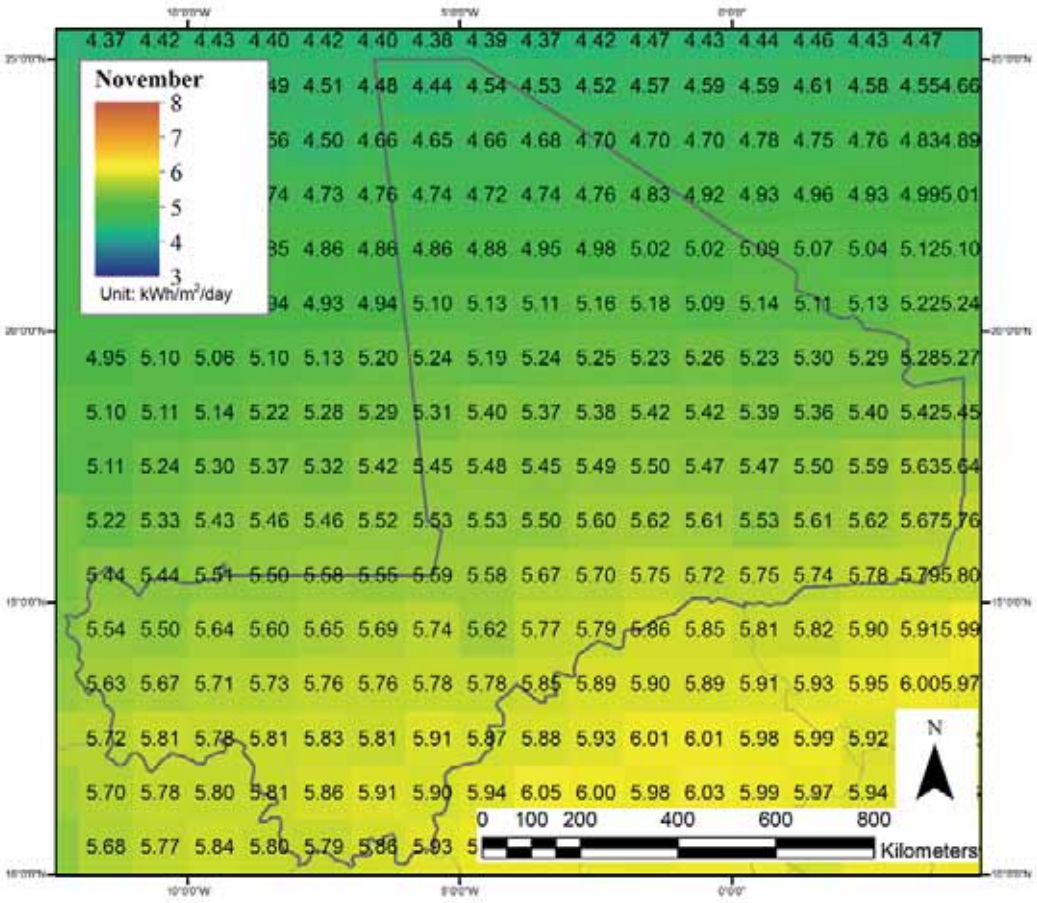
November
8
7
6
5
4
3
Unit: kWh/m²/day
N
0 100 200 400 600 800
Kilometers

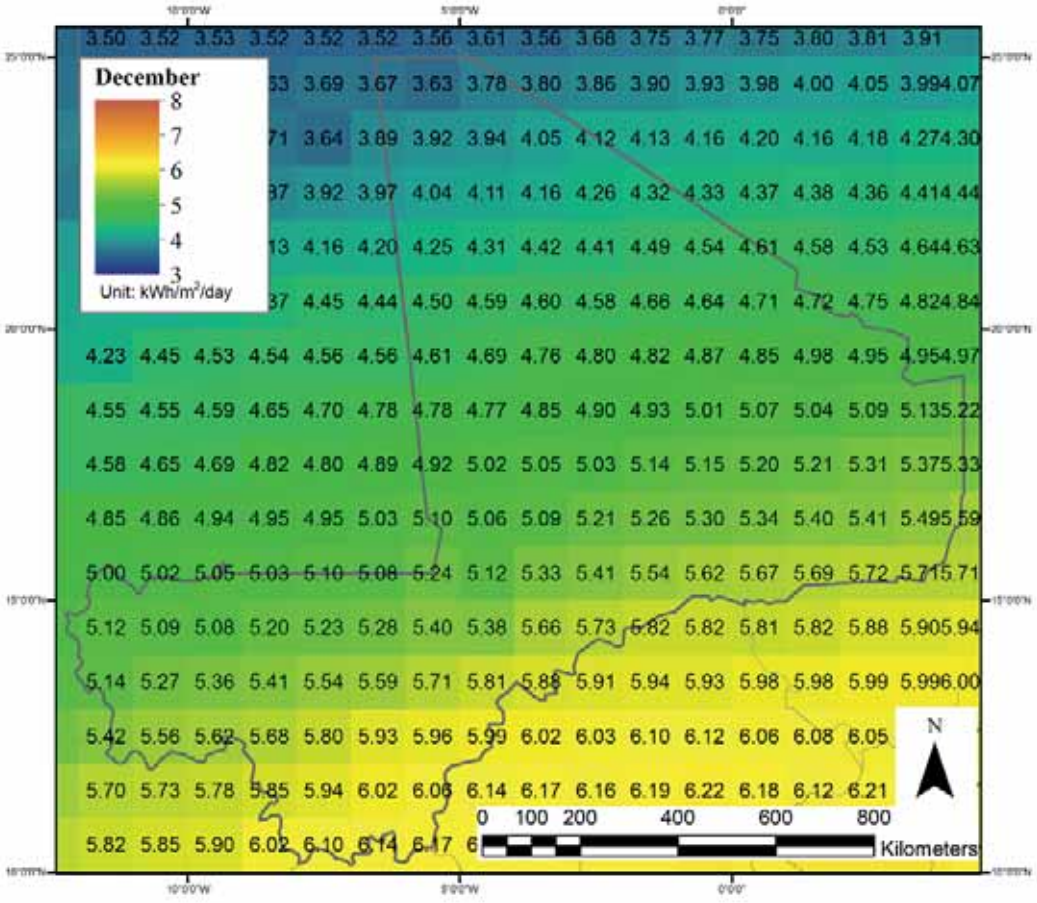
December
8
7
6
5
4
3
Unit: kWh/m²/day
N
0 100 200 400 600 800
Kilometers